Optical determination of the temperature of a laser heated industrial diamond

Bathusile Nelisiwe Masina

Submitted in partial fulfilment of the requirements for the degree of

Master of Science

UNIVERSITY of ZULULAND

Supervisor: Dr. A. Forbes (CSIR – NLC)

Co-supervisor: Prof. O.M. Ndwandwe

Co-supervisor: Prof. G.R. Hearne (Wits)

March 2008

Declaration

I declare that this dissertation is my own work that has not been submitted before for any degree or assessment in any University, that all the sources I have used have been indicated and acknowledged by means of references.

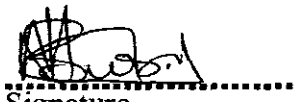

Signature

25/08/08

Date

Acknowledgements

- First and foremost, praise and thanks go to the Almighty God, for His Love and Blessings all the time.
- I am deeply indebted and extremely thankful to the following people:
    - Prof. O.M. Ndwandwe and Dr. A. Forbes for supervising this work.
    - Prof. G. Hearne for the warm welcome at the University of the Witwatersrand and allowing me to use his laboratory, for everything he did for me.
    - Mr. H. van Wyk for his help in technical aspect of work.
    - Mr. R. Erasmus for his help with the analysis.
    - Mr. B. W. Mwakikunga for his guidance, encouragement, time and discussion the experimental work.
- I would like to extend my deep appreciation to CSIR-NLC for granting me the opportunity to work in such a conducive environment, in particular the User Facility. My studies were funded by NRF, CSIR and Element-six (De Beers).
- To the staff at CSIR-NLC (Vatiswa Mbebe, Priscilla Lesele and Tshepiso Mothibinyane) who made it possible for me to feel at home.
- To my family, boMasina (Lutsala), boBembe (Mavudla), for their moral support and believing that I could achieve this.
- To my friends, Vhutshilo Nekhwalivha, Thomas Sibiya and Ally Mathye, for their support, encouragement and believing that I could achieve this.
- To my daughter, Comfort Lukhele, thanks for being nano-meters away from my heart and understanding that I had to be away.

Abstract

Diamond has the highest thermal conductivity among known materials. In order to heat diamond to high temperature and measure the temperature, one needs to have a laser heating system with sufficiently good power stability, beam position and suitable wavelength for absorption. In this dissertation we heated, and measured the temperature of a diamond sample by using a CO_2 laser. Temperatures are difficult to measure with the accuracy and stability required for many potential applications. Temperature sensors such as thermocouples that depend on attainment of thermal equilibrium with a surface via conductive or convective heat transfer are problematic because: (i) they require intimate contact with the surface which affects the local surface energy balance, especially when minute regions of the sample are to be probed, and (ii) they are limited to temperatures of $\leq$1500 °C. Similar restrictions apply to pyrometric, non-contact, temperature determination of hot-spots where the colour of a hot object is referenced against that of a heated tungsten filament. However these limitations do not apply in the case of non-contact infrared thermometry (spectro-radiometry), involving the grey-body (Planck) emission envelope emanating from a hot spot, which may even be well below sub-millimeter dimensions. A model of the surface temperature was successfully developed and qualitatively compared to the experimental results. CO_2 and Nd: YAG laser heating was employed for heating two different industrial diamonds at extreme high power levels. The industrial diamonds were characterised using Raman spectroscopy, Scanning electron microscopy and X-ray diffraction. We show that there was some changing (physical and chemical) in the industrial diamond after heating.

In loving memory of my mother

Lettah Bembe (1957-2005)

Contents

Chapter 4

Chapter 5

Chapter 6

List of figures

is made of W and Co, initially. The EDS spectrum for number 2 shows that the PCD is mostly C.

Figure 7.9: This is the zoom-in of figure 7.8 at the PCD/W-Co interface and shows the honeycomb construction of the materials before heating it. The EDS number 3 illustrates that the white material is the made of W, Fe, C and Co. EDS spectrum in number 4 is W, Co and C. Number 5 is along the interface between the PCD and substrate and shows that the most abundant element is Co.

Figure 7.10: SEM micrograph and EDS spectra taken on the surface of the industrial diamond after heating by Nd: YAG laser for 8 seconds. The micrograph and EDS spectra show spheres that are made of Co and W.

Figure 7.11: SEM micrograph on the surface of an industrial diamond and EDS spectrum of an industrial diamond after heating with CO_2 laser for 8 seconds on the PCD.

Figure 7.12: SEM cross-section micrograph and EDS spectrum of an industrial diamond after heating with CO_2 laser for 8 seconds. This micrograph was taken on the substrate.

Figure 7.13: A schematic diagram of the industrial diamond illustrating C_OS, C_IS, and M_IS. C_ground is the mixture of C_OS and C_IS ground to a powder.

Figure 7.14: The XRD spectra of the industrial diamond after heating with Nd: YAG laser. The spectrum of M_IS shows that the substrate reacted and formed WC, WO_3 and $CoWO_4$.

Figure 7.15: XRD spectra of the industrial diamond after heating with CO_2 laser. The spectrum of the C-OS is showing the migration of Co into the C. The spectrum of the C_IS is showing the W+Co. The $CaCO_3$ may originate from the calcite in the clay that was used to mount the sample. The spectrum of the M_IS is showing that the substrate, W+Co changed from W+Co to WC.

Figure 7.16: Schematic diagram of the two lasers in action.

List of tables

Chapter 1

1.1 Introduction

Temperature is difficult to measure with the accuracy and stability required for many potential methods [1]. These methods include multiwavelength thermometry, ratio thermometry, reflectance and absorptance measurement techniques, temperature sensor, etc. In multiwavelength thermometry, the spectral intensity of the target at several wavelengths is curve fitted to Planck's equation. In ratio thermometry the ratio of the spectral intensity at two wavelengths is used to measure temperature, which requires that either the emissivity ratio at the two wavelengths is unity or is known from prior measurements. Other techniques derive emissivity from the direct and simultaneous measurement of reflectance or absorptance of the target at the wavelength concerned. Any of these methods may provide a significant advantage for a particular application or measurement situation. All these methods are directed at minimizing the temperature error caused by an uncertainty in emissivity.

Temperature sensors such as thermocouples that depend on attainment of thermal equilibrium with a surface via conductive or convective heat transfer are problematic because: they require intimate contact with the surface which affects the local surface energy balance, especially when minute regions of the sample are to be probed, and they are limited to temperatures of ≤ 1500 °C [1-3]. Similar restrictions apply to pyrometric, non-contact, temperature determination of hot-spots where the colour of a hot object is referenced against that of a heated tungsten filament. However these limitations do not apply in the case of non-contact infrared thermometry (spectro-radiometry) [1], involving the grey-body (Planck) emission envelope in the range 400 – 1000 nm emanating from a hot spot, which may even be well below sub-millimeter dimensions.

1.2 Objectives of the present work

The main focus of this work was to set-up a laser-based system to raise the temperature of a diamond sample in a controlled and repeatable manner. Obviously, the laser-based system has to be understood very well before heating and measuring temperature, hence characterisation of a laser must be done before the heating. The heating is due to direct linear absorption of the laser radiation by the sample. The temperature was measured during the heating process by non-contact temperature measurement. In this study, an emission spectrometer was employed to measure the thermal radiation spectrum of the sample and the temperature was extracted by

using the Planck radiation function. A model was developed to predict the temperature gradients in the sample that was compared with the experimental data. Characterisation techniques were used to study the industrial diamond.

1.3 Plan of the dissertation

This dissertation contains eight chapters. Chapter 2 provides more insight on the origin of the blackbody radiation. Scanning electron microscopy (SEM), Raman spectroscopy and x-ray diffraction (XRD) methods were used to characterise the industrial diamond in the present study and are discussed in Chapter 3. The basic principles of lasers such as a CO_2 laser are also discussed in Chapter 3. The mathematical model and the results of the model are presented and discussed in Chapter 4. The characterisation of a CO_2 laser and the results of the characterisation are presented and discussed in Chapter 5. The experimental set-up and non-contact temperature measurement results are addressed and discussed in Chapter 6. The characterisation results are presented and discussed in Chapter 7, while the conclusions and future work drawn from the results obtained in this study are found in Chapter 8.

Chapter 2

Theory

2.1 Introduction

Several experimental methods and approximations have been used by different scientists to measure the temperature of an object. This chapter discusses some of the methods that have been used to measure temperature. The subject of consideration in this chapter is the blackbody model, which is of primary importance in thermal radiation theory and is a fundamental law of radiation. The quantitative blackbody radiation laws and their corollaries are analysed in detail. The emissivity and absorptivity of physical bodies of grey-body radiation character are also discussed in this chapter.

However, the main goal of this chapter is to detail the approximations and methods employed to determine temperature of an object. Temperature is recognized as one of the basic variables in science, particularly in thermodynamics and statistical mechanics and it is a measure of the average heat or thermal energy of the particles in a substance [4]. Many physical properties of materials including the phase, density and electrical conductivity depend on the temperature. Temperature also plays an important role in determining the rate and extent to which chemical reactions occur. One of the reasons why a human body has several elaborate mechanisms for maintaining the temperature at 37 ^{0}C, is that only a few degrees higher than body temperature harmful reactions may take place with serious consequences [4-5]. Temperature also controls the type and quantity of thermal radiation emitted from a surface. One of these effects is emission of radiation from the incandescent light bulb, when a tungsten filament is electrically heated to a high temperature [6].

2.2 Thermal radiation

All objects whose temperature is above absolute zero radiate energy in a wide range of wavelengths, i.e., electromagnetic waves as shown in figure 2.1. This kind of radiation is referred to as thermal radiation [6]. Thermal radiation is a direct result of the movements of atoms and molecules in a material. These atoms and molecules are composed of charged particles and their movements result in the emission of electromagnetic radiation, which carries energy away from the surface [5]. The surface is uniformly pumped by radiation from the surroundings, resulting in the transfer of energy to the surface. The amount of emitted

radiation increases with increasing temperature. This radiation depends not only on the temperature but also on the composition of the object [7]. It emits electromagnetic radiation in a continuous range of wavelengths/frequencies. Electromagnetic radiation is usually quantified according to its wave-like properties, which include intensity and wavelength/frequency. The colour of any particular kind of radiation is designated by its frequency [5-6]. The length of a single wave is called the wavelength. The challenge was to show how this radiant energy is related to the temperature of the object.

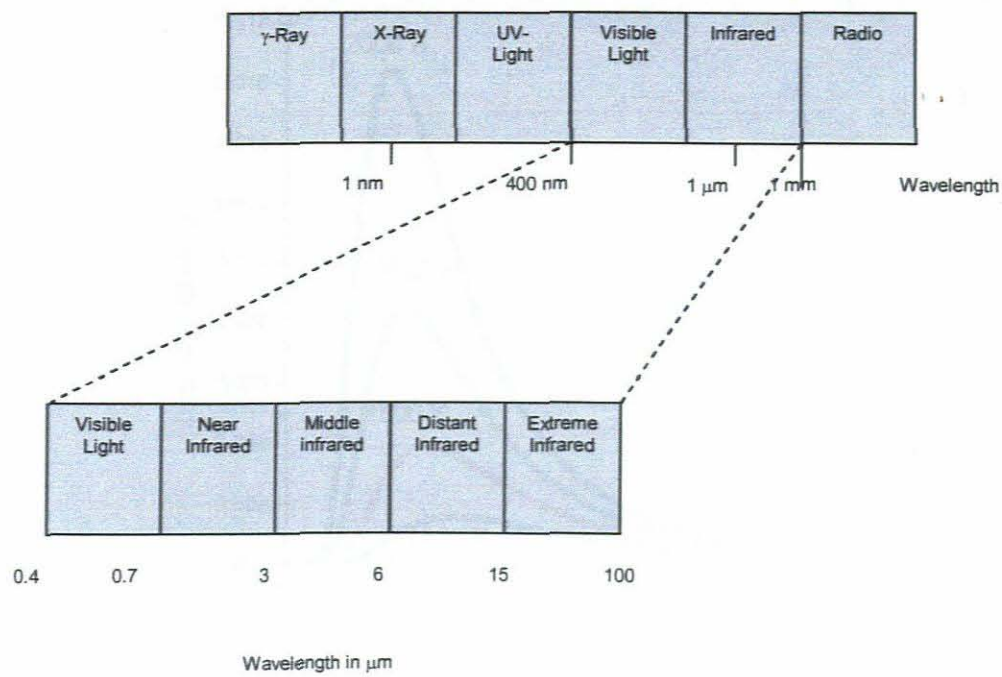

Figure 2.1: Electromagnetic spectrum.

2.2.1 Blackbody

The blackbody is of primary importance in studying thermal radiation and electromagnetic radiation transfer in all wavelength bands. It is an ideal radiation absorber, and the blackbody is used as a standard against which the absorption of real bodies is compared [7]. The blackbody is so called because those bodies that absorb all incident visible light will seem black to the human eye. The term is, certainly, purely conventional and has historical roots. An example, we can hardly characterize our sun, which is indeed almost a blackbody within a very wide band of electromagnetic radiation wavelengths as a black physical object in optics.

A blackbody is defined as a theoretical object that absorbs all radiation incident upon it, regardless of frequency [6-7]. Therefore it reflects no radiation and appears perfectly black. In practice no material has been found to absorb all incoming radiation [9].

A blackbody radiates more intensity when it is hot than when it is cold. The spectrum of a hot blackbody has its peak at a higher frequency than the peak in the spectrum of a cooler one. At low temperatures, the wavelengths of the thermal radiation are mainly in the infrared region.

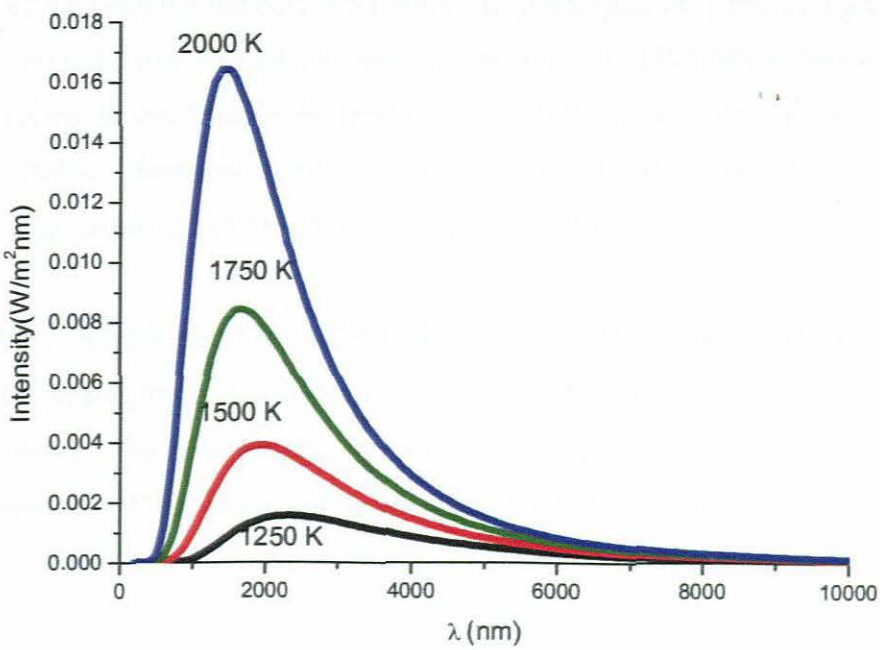

Figure 2.2: Simulations of blackbody radiation curves showing peak wavelengths at various temperatures.

The graph in figure 2.2 shows how the blackbody radiation curves change at various temperatures. All the curves have their peak wavelengths in the infra-red part of the spectrum. The graph shows that as the temperature increases, the peak wavelength emitted by the blackbody decreases. It then begins to move from the infra-red towards the visible part of the spectrum. The graph also shows that as temperature increases, the total energy emitted increases, because the total area under the curves increases.

2.2.2 Blackbody Radiation laws

General thermodynamic considerations allowed Kirchhoff, Boltzmann and Wien to derive a series of important laws concerning the emission of heated bodies. These general considerations were insufficient for deriving a particular law of energy distribution in the ideal blackbody radiation spectrum. In 1893, it was Wien who advanced in this direction more than the others [7]. He studied the temperature and entropy of thermal radiation and showed that the maximum radiation in the blackbody spectrum displaces to the side of shorter wavelengths with increasing temperature (Wien's displacement law) and at a given frequency the radiation intensity can depend on temperature only. In 1896 Wien derived the law of energy distribution in the blackbody spectrum that was correct only in the case of short waves. Nevertheless, these two laws of Wien have played a considerable part in the development of quantum theory (the Nobel Prize, 1911) [9].

In 1900 and 1905, Rayleigh and Jeans derived the spectral distribution of thermal radiation on the basis of the assumption that the classical idea on the uniform distribution of energy is valid [9]. However, the temperature and frequency dependencies obtained differed from Wien's relationships. Wien's expression for spectral energy distribution was invalid at high temperatures and short wavelengths, according to the results of fairly accurate measurements, carried out before that time. Planck stepped in for consideration of harmonic oscillators, which have been taken as the sources and absorbers of radiation energy. Planck obtained an equation, which very soon was reliably confirmed experimentally on the basis, first of all, of the Wien-Lummer blackbody model [9]. Investigation for the theory modifications that would allow this empirical equation to be derived, Planck made some assumptions constituting the quantum theory basis (the Nobel Prize, 1918) [10].

2.2.3 Planck's law

In 1901, Max Planck derived the Planck's blackbody formula theoretically [5, 8, and 9]. In this theory Max Planck [4, 11] assumed that electromagnetic harmonic oscillations can only exist in energy quanta of $h\nu$ (h is Planck's constant and has the value 6.62517×10^{-34} m^2 kg s^{-1}, ν is frequency) and that oscillators emit energy only when changing from one level to another level of their quantized energy states.

Imagine a cavity (vacuum) in the shape of a rectangular parallelepiped with reflecting metallic walls. At the walls, the electric field E must vanish, and therefore the radiation within the cavity will be an ensemble of standing waves that satisfy the boundary condition $E = 0$ at the walls. A standing wave is a superposition of two travelling waves, propagating in opposite directions. We represent a travelling wave in the form

$$E = E_0 e^{i(\omega t - kr)} \tag{2.1}$$

where $\boldsymbol{k}$ is the wave vector whose components are

$$k_x = \frac{2\pi}{\lambda_x},\ k_y = \frac{2\pi}{\lambda_y},\ k_z = \frac{2\pi}{\lambda_z} \tag{2.2}$$

The expression for a standing wave is then

$$E = E_0 e^{i\omega t}(e^{ikr} - e^{-ikr}) \tag{2.3}$$

To satisfy the boundary conditions, the wavelengths of the travelling waves must be

$$\lambda_x = \frac{2L_x}{n_x},\ \lambda_y = \frac{2L_y}{n_y},\ \lambda_z = \frac{2L_z}{n_z}. \tag{2.4}$$

where L_x, L_y, L_z are the lengths of the cavity and n_x, n_y, n_z are positive integers. Consequently, the wave vector must have components

$$k_x = \left(\frac{\pi}{L_x}\right)n_x, k_y = \left(\frac{\pi}{L_y}\right)n_y,\ k_z = \left(\frac{\pi}{L_z}\right)n_z \tag{2.5}$$

To derive the Planck distribution we need to know the number of possible modes in the frequency interval between ν and $\nu + d\nu$. For electromagnetic waves, $\nu = c/\lambda = 2\pi ck$, and so we seek the number of standing waves whose wave vectors fall in the interval between k and $k + dk$. When counting the number of standing waves, subject to condition (equation (2.5)), we must remember that n_x, n_y, and n_z have to be positive integers to avoid counting the same standing wave twice.

We proceed by first calculating the number of standing waves whose wave vector is less than some value k. The vector of magnitude k defines a sphere in this $\boldsymbol{k}$-space, a vector space whose Cartesian coordinates are k_x, k_y, k_z. The volume of that sphere is $\frac{4}{3}\pi k^3$. Now the number of wave vectors that terminate in the volume elements dk_x, dk_y, dk_z is, from equation (2.5),

$$dn_x dn_y dn_z = \frac{L_x L_y L_z}{\pi^3} dk_x dk_y dk_z = \left(\frac{V}{\pi^3}\right) dk_x dk_y dk_z$$

In other words, the density of wave vectors in $\boldsymbol{k}$-space is V/π^3.

For each value of $\boldsymbol{k}$ there are two independent modes, corresponding to the two independent directions of polarization of an electromagnetic wave. Consequently, the number of modes in the positive octant (positive n_x n_y n_z) of the sphere of radius k is

$$N(k) = 2\left(\frac{1}{8}\right)\left(\frac{4\pi k^3}{3}\right)\left(\frac{V}{\pi^3}\right) = \left(\frac{V}{3\pi^2}\right) k^3 \qquad (2.6)$$

The number of modes between k and $k + dk$ is obtained by differentiating $N(k)$. We call this the density of states in $\boldsymbol{k}$-space and use the symbol $\eta(k)$. Thus

$$\eta(k) dk = \left(\frac{V}{\pi^2}\right) k^2 dk, \qquad (2.7)$$

is the number of modes in the interval between k and $k + dk$.

Since $k = 2\pi/\lambda = 2\pi\nu/c$, the number of modes per unit volume $g(\nu)d\nu$, in the frequency interval between ν and $\nu + d\nu$ is

$$g(\nu) d\nu = \frac{8\pi}{c^3} \nu^2 d\nu \qquad (2.8)$$

The energy density in the cavity as a function of frequency is now given by the product of $g(v)$ and the average of an electromagnetic mode of frequency v. The probability that at a temperature T a mode of energy $\in$ is excited is

$$f(\in) = Ce^{-\in/kT} \tag{2.9}$$

where $C = 1/kT$ is normalization constant and $e^{-\in/kT}$ is the Boltzmann factor. If the energy $\in$ were a continuous function, as assumed in classical physics, the average energy of mode would be

$$\langle \in \rangle_{cl} = \int_0^\infty \in f(\in) d \in = kT \tag{2.10}$$

If we now multiply $\langle \in \rangle_{cl}$ by $g(v)$, we arrive at the expression for the frequency dependent energy $U(v)$ first derived by Rayleigh and Jeans,

$$U(v) = \left(\frac{8\pi}{c^3}\right) v^2 kT \tag{2.11}$$

Equation (2.11), proposed after Planck's formula, cannot possibly be correct. The difficulty, recognized by Rayleigh and Jeans, is that according to equation (2.11) the energy density increases without limit as the frequency increases. That is, $U(v)$ diverges as $v \to \infty$. This "unphysical" consequence of equation (2.11) came to be known as the ultraviolet catastrophe.

If, as proposed by Planck, the allowed energy is not a continuous variable, the integral form for the average energy, equation (2.10), is inapplicable. Instead, we should perform a summation over the discrete energy states given by

$$\in_n = nhv . \tag{2.12}$$

The average energy is then

$$\langle \in \rangle = \sum \in_n f_n , \tag{2.13}$$

where

$$f_n = C' e^{-\epsilon / kT} = C' e^{-nhv/kT}. \tag{2.14}$$

The normalization constant C' is now obtained from the condition

$$\sum f_n = 1. \tag{2.15}$$

To evaluate that sum we note that we can write

$$\sum f_n = C' \sum e^{-nx} = C' \left[1 + e^{-x} + \left(e^{-x}\right)^2 + \left(e^{-x}\right)^3 + \ldots\right]$$

$$= \frac{C'}{1 - e^{-x}}, \tag{2.16}$$

where we have set $x = hv/kT$ and have made use of the binomial expansion of $(1+a)^{-1}$.

Thus $C' = \left(1 - e^{-hv/kT}\right)$

To evaluate $\langle \epsilon \rangle$ we again write out the summation terms:

$$\langle \epsilon \rangle = \sum \epsilon_n f_n = \left(1 - e^{-hv/kT}\right) hv \sum n e^{-nx}$$

$$= \left(1 - e^{-hv/kT}\right) hv \left[e^{-x} + 2\left(e^{-x}\right)^2 + 3\left(e^{-x}\right)^3 + \ldots\right]$$

$$= \left(1 - e^{-hv/kT}\right) hv \left\{-\frac{d}{dx}\left[e^{-x} + 2\left(e^{-x}\right)^2 + 3\left(e^{-x}\right)^3 + \ldots\right]\right\}$$

$$= \left(1 - e^{-hv/kT}\right) hv \left[\frac{d}{dx}\left(1 - e^{-x}\right)^{-1}\right] = \frac{hv}{e^{hv/kT} - 1}. \tag{2.17}$$

On multiplying equation (2.17) by the density of states $g(v)$, we obtain the Planck distribution

$$U(v) = \frac{8\pi v^2}{c^3}\left(\frac{hv}{e^{hv/kT} - 1}\right). \tag{2.18}$$

This then is the expression which Planck developed for the frequency distribution of energy in blackbody radiation (spectral energy density, $U(v)$ is defined as the energy density per unit frequency interval centred at a given frequency). One can obtain the equivalent in terms of

spectral intensity $I(\nu)$ (spectral intensity is defined as spectral energy per unit time per unit surface area per unit solid angle per unit frequency,$Js^{-1}m^{-2}sr^{-1}Hz^{-1}$) as follows [12]:

$$I(\nu)=\frac{U(\nu)c}{4\pi}. \tag{2.19}$$

$$I(\nu)=\frac{8\pi h\nu^3}{c^3}\frac{1}{\exp\left(\frac{h\nu}{kT}\right)-1}\times\frac{c}{4\pi}. \tag{2.20}$$

$$I(\nu)=\frac{2h\nu^3}{c^2}\frac{1}{\exp\left(\frac{h\nu}{kT}\right)-1}. \tag{2.21}$$

In many practical applications in determining the spectral intensity of radiation the wavelength is used instead of frequency. It is impossible to transfer from frequency to wavelength by simply replacing the frequency with the wavelength in expression (2.21), because of the relationship between ν and λ. However, this expression can be transformed by taking into account that

$$I(\nu)|d\nu| = I(\lambda)|d\lambda|,$$

$$I(\lambda) = I(\nu)\left|\frac{d\nu}{d\lambda}\right|. \tag{2.22}$$

The well known relationship between wavelength and frequency is given as

$$\nu=\frac{c}{\lambda}. \tag{2.23}$$

Then, after appropriate differentiation, the expression of Planck's equation for the spectral intensity of a black body becomes

$$I(\lambda)=\frac{2hc^2}{\lambda^5}\frac{1}{\exp\left(\frac{hc}{\lambda kT}\right)-1}. \tag{2.24}$$

The above equation may be put into this form,

$$I(\lambda) = \frac{c_1}{\lambda^5} \frac{1}{\exp\left(\frac{c_2}{\lambda T}\right) - 1}. \tag{2.25}$$

where

$$c_1 = 2hc^2, c_2 = \frac{hc}{k}.$$

Planck's law gives the intensity of radiation per unit wavelength interval per unit area at absolute temperature [5, 8, 9]. The Planck's formula in equation (2.25) is for blackbody radiation. The well-known curves of Planck's equation describe the energy distribution as a function of temperature and wavelength as shown in figure 2.3.

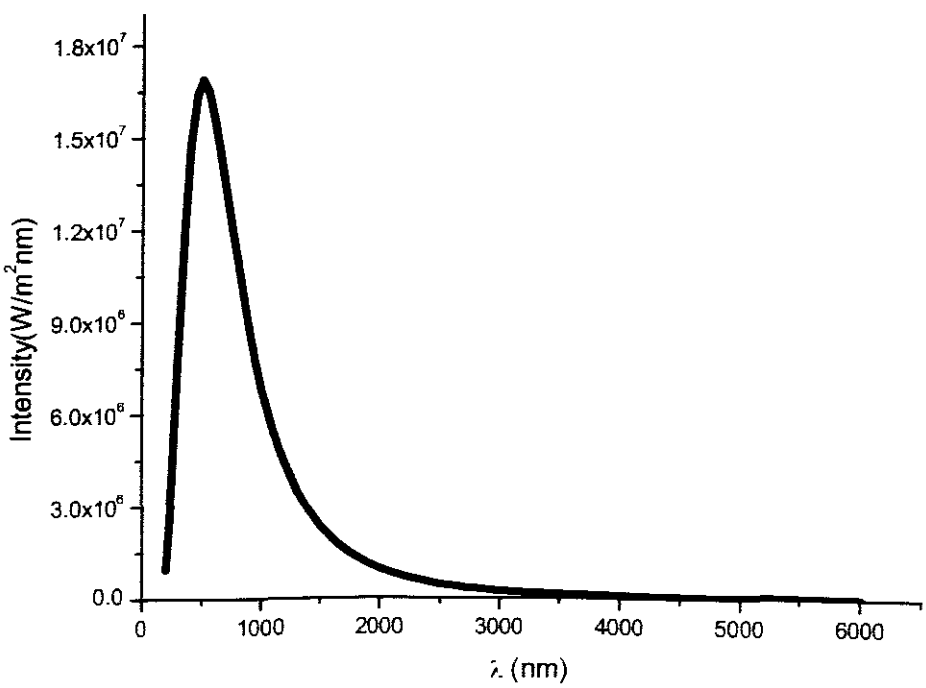

Figure 2.3: Simulation spectrum of the sun, with T = 5800 K.

2.2.4 Related Derivations

IV. Wien's approximation law

Wien's approximation is a law of physics used to describe the spectrum of thermal radiation. Wilhelm Wien was the first to derive this law in 1896 [9,10]. Wien's approximation formula accurately describes the short wavelength spectrum of thermal radiation from objects, but it failed to accurately describe long wavelength radiation. Wien's approximation can be derived from Planck's law equation by assuming $\exp\left(\frac{c_2}{\lambda T}\right) >> 1$. When this is true, then

$$\frac{1}{\exp\left(\frac{c_2}{\lambda T}\right)-1} \approx \exp\left(-\frac{c_2}{\lambda T}\right). \tag{2.26}$$

and then,

$$I(\lambda) = \frac{c_1}{\lambda^5}\left(\exp -\frac{c_2}{\lambda T}\right). \tag{2.27}$$

Therefore Planck's law approximately equals Wien's approximation at short wavelength. For the values of $\lambda T >> 3000\,\mu\text{m K}$ this formula gives an error within the limits of 1% [10].

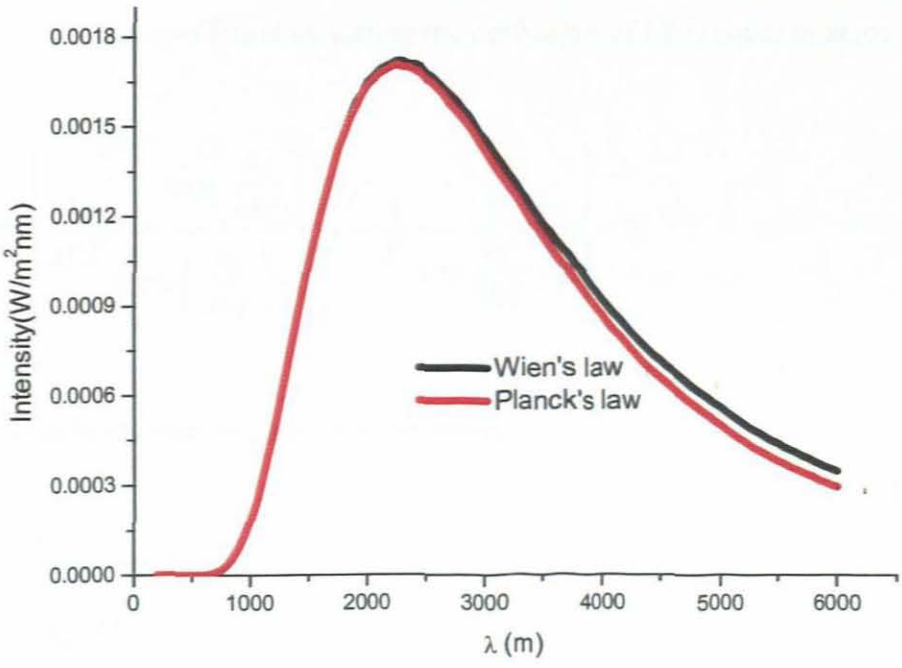

Figure 2.4: Simulation graphs showing comparison of intensity versus wavelength for a blackbody at 1273 K according to Planck's law in equation (2.25) and to Wien's law in equation (2.27). Planck's law is considered to be exact.

V. Wien's Displacement law

Wien's displacement law states that the hotter an object is; the shorter the wavelength at which it will emit most of its radiation [13]. Then the wavelength for maximum or peak radiation power is found by dividing Wien's constant by the temperature in Kelvin. This law is named after Wilhelm Wien, who developed/derived the relationship in 1893 based on a thermodynamic argument [14]. However, Wien was not able to derive the constant b in his relationship but later done by Planck as will be shown below.

Nowadays, the usual practice is to derive the relationship from Planck's law of blackbody radiation. From equation 2.18:

$$U(\lambda) = \frac{8\pi hc}{\lambda^5} \frac{1}{\exp\left(\frac{hc}{\lambda kT} - 1\right)} \quad . \tag{2.28}$$

The wavelength λ_{max} at which $U(\lambda)$ is a maximum satisfies a relation known as Wien's displacement law. It can be found by setting the derivative of $U(\lambda)$ equal to zero:

$$\frac{\partial U(\lambda)}{\partial \lambda} = 8\pi hc\left(\frac{hc}{kT\lambda^7}\frac{\exp\left(\frac{hc}{\lambda kT}\right)}{\left(\exp\left(\frac{hc}{\lambda kT}\right)-1\right)^2}-\frac{1}{\lambda^6}\frac{5}{\exp\frac{hc}{\lambda kT}-1}\right)=0. \tag{2.29}$$

Then by applying some algebra, one gets this result,

$$\frac{hc}{\lambda_{\max} kT}\frac{1}{1-\exp\frac{hc}{\lambda_{\max} kT}}-5=0. \tag{2.30}$$

Let $$x=\frac{hc}{\lambda_{\max} kT}. \tag{2.31}$$

Then,

$$\frac{x}{1-\exp(-x)}-5=0. \tag{2.32}$$

This equation cannot be solved in terms of elementary function [13-14], but it can be solved numerically, with x given by:

$$x=4.965\ . \tag{2.33}$$

Solving for the wavelength in units of nm and using units of K for temperature:

$$\lambda_{\max}=\frac{hc}{kx}\frac{1}{T}, \tag{2.34}$$

And then by substituting the necessary input of the constant, one gets this

$$\lambda_{max} = \frac{2.8977 \times 10^6 \, nm.K}{T}. \tag{2.35}$$

VI. Stefan-Boltzmann's law

Stefan showed experimentally in 1879 that for a blackbody the rate at which energy is emitted is related to the object's temperature [8-9]. The law may be written as:

$$P(T) = \varepsilon \sigma T^4, \tag{2.36}$$

where P is the rate at which energy is emitted per unit area of blackbody surface at absolute temperature T, including radiation of all wavelengths from 0 to ∞ throughout the solid angle, and σ is the Stefan-Boltzmann radiation constant. Area is given in square centimetres and T in Kelvin and P is in watts per square centimetres. However, real hot objects always radiate less efficiently than the blackbody, therefore for non-blackbody objects, a positive quantity, ε, referred to as the emissivity, which is always less than 1, and depends on the material, the surface and the temperature.

The Stefan-Boltzmann law is obtained by integrating the spectral intensity given by Planck's law as follows:

$$I(\lambda) = \frac{c_1}{\lambda^5} \frac{1}{\left(\exp \frac{c_2}{T\lambda} - 1 \right)}, \tag{2.37}$$

$$P = \int_0^{\infty} \frac{c_1}{\lambda^5} \frac{1}{\left(\exp \frac{c_2}{\lambda T} - 1 \right)} d\lambda. \tag{2.38}$$

and then by taking out the constant c_1, one gets this

$$P = c_1 \int_0^{\infty} \frac{\lambda^{-5} d\lambda}{\left(\exp \frac{c_2}{\lambda T} - 1 \right)}. \tag{2.39}$$

The above equation may be put into this form,

$$P = c_1 \int_0^{\lambda} \frac{\lambda^{-3}\left(\lambda^{-2} d\lambda\right)}{\left(\exp \frac{c_2}{\lambda T} - 1\right)}. \tag{2.40}$$

Since $d(\lambda^{-1}) = -\lambda^{-2} d\lambda$, the above expression becomes,

$$P = -c_1 \int_0^{\lambda} \frac{\left(\lambda^{-1}\right)^3 d\left(\lambda^{-1}\right)}{\left(\exp \frac{c_2}{\lambda T} - 1\right)}. \tag{2.41}$$

Reversing the limits to remove the minus sign before the integral and multiplying through by $\left[\left(T^4 / c_2^4\right)\left(c_2^3 / T^3\right)\left(c_2 / T\right)\right]$,

$$P = \frac{c_1 T^4}{c_2^4} \int_0^{\infty} \frac{\left(\frac{c_2}{\lambda T}\right)^3 d\left(\frac{c_2}{\lambda T}\right)}{\left(\exp \frac{c_2}{\lambda T} - 1\right)}. \tag{2.42}$$

In latter equation the limits of integration are in terms of $\frac{c_2}{\lambda T}$ or $\frac{1}{\lambda T}$, since c_2 is a constant. If

$x = \frac{c_2}{\lambda T}$.

Then

$$P = \frac{c_1}{c_2^4} \left[\int_0^{\infty} \frac{x^3 dx}{\exp x - 1} \right] T^4. \tag{2.43}$$

Since $\frac{1}{\exp x - 1} \times \frac{\exp(-x)}{\exp(-x)} = \frac{\exp(-x)}{1 - \exp(-x)} = \exp(-x) + \exp(-2x) + \exp(-3x) \ldots + \exp(-\infty)$.

Then by dividing $\exp(-x)$ by $(1 - \exp(-x))$, equation (2.43) becomes

$$P = \frac{c_1}{c_2^4}\left[\int_0^\infty x^3 \exp(-x)dx + \int_0^\infty x^3 \exp(-2x)dx + \int_0^\infty x^3 \exp(-3x)dx + ..\right]T^4 \qquad (2.44)$$

Since $\int_0^\infty x^n \exp(-ax)dx = \frac{n!}{a^{n+1}}$.

and if $n = 3$ equation (2.44) becomes

$$P = \frac{c_1}{c_2^4}\left[\frac{3!}{1^4} + \frac{3!}{2^4} + \frac{3!}{3^4} + ... + \frac{3!}{\infty}\right]T^4. \qquad (2.45)$$

Since 3! = 6

$$P = \frac{6c_1}{c_2^4}\left[\frac{1}{1^4} + \frac{1}{2^4} + \frac{1}{3^4} + ...\frac{1}{\infty^4}\right]T^4. \qquad (2.46)$$

The above equation may be put into the form

$$P = \frac{6c_1}{c_2^4}\left[\sum_{n=1}^{\infty}\frac{1}{n^4}\right]T^4. \qquad (2.47)$$

Let $\sigma = \frac{6c_1}{c_2^4}\left[\sum_{n=1}^{\infty}\frac{1}{n^4}\right]$

The numerical value of σ may be determined and then the Knoop's theory and application of infinite series gives the following particular solution of his equation

$$\sum_{n=1}^{\infty}\frac{1}{n^4} = \frac{\pi^4}{90}. \qquad (2.48)$$

and then by substituting the necessary input of the constant and multiplying with the above sum, one gets

$\sigma = 5.669 \times 10^{-12}$ Watts cm^{-2} T^{-4}. (2.49)

Therefore

$$P(T) = \sigma T^4. \tag{2.50}$$

The above equation is for blackbody objects and a non-blackbody object is given as:

$$P(T) = \varepsilon\sigma T^4. \tag{2.51}$$

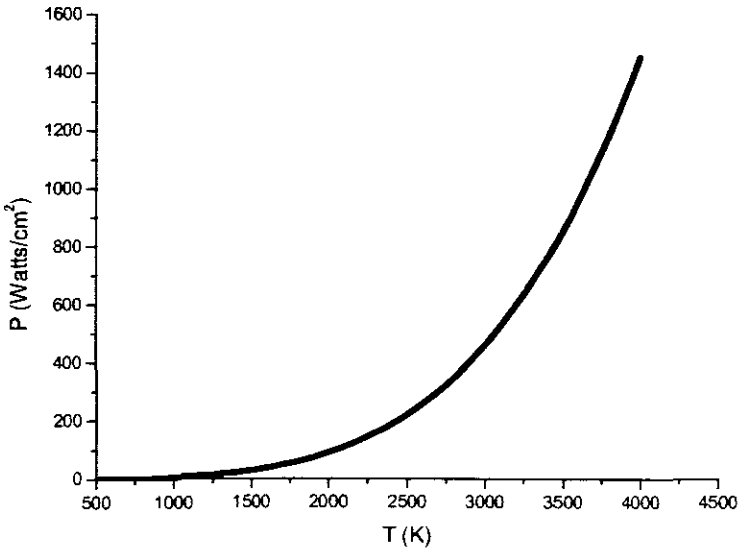

Figure 2.5: A Simulation graph showing comparison of power versus temperature changes according to change in equation (2.51).

2.2.5 Emissivity of various Materials

Different materials absorb radiation in different ways. Metals reflect most of the energy away so they do not absorb much radiation, while a black material absorbs most of the incident energy and its temperature may be raised as a result.

Emissivity is a fundamental property of a material. It is used to describe the emittance based on the conditions that it is perfectly flat and even on a molecular scale. Emissivity ε is defined [5, 13] as a measure of the ability of a body to radiate heat and is given by the ratio of the power radiated by the body per unit area, to the power radiated per unit area of a blackbody at the same temperature.

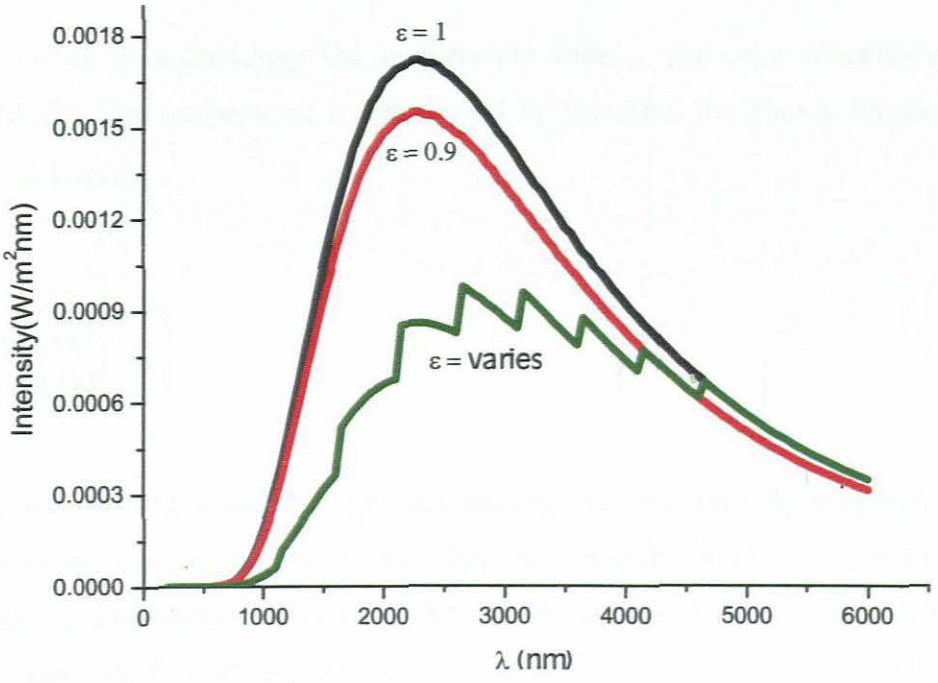

Figure 2.6: Simulations of emitted radiation as a function of λ for bodies at 1273 K and 3 different ε.

A blackbody has an emissivity of 1 [5, 10] because it absorbs or emits without reflectance or transmission. Real bodies have an emissivity of less than 1. The emittance depends on shape, surface roughness, and oxidation or other surface effects. The emissivity ability of a real physical body depends on different factors such as its temperature, its physical and chemical composition, and the angle at which the radiation is emitted [10].

If a non-blackbody is being viewed, however, its emissivity, which is a function of wavelength and temperature, must be taken into consideration. Then the formula in equation (2.24) can be expressed as:

$$I(\lambda) = \frac{c_1 \varepsilon(\lambda)}{\lambda^5 \left(\exp\left(\frac{c_2}{\lambda T} \right) - 1 \right)}, \tag{2.52}$$

where ε is the emissivity.

2.2.6 Temperature

One is interested in determining the temperature from a particular blackbody radiation spectrum $I(\lambda,T)$. The temperature is determined by inverting the Planck function with an appropriate emissivity,

$$T = \frac{c_2}{\lambda \ell n\left(\frac{c_1 \varepsilon(\lambda)}{I(\lambda)\lambda^5}+1\right)}. \tag{2.53}$$

The temperature derived is called brightness temperature or blackbody temperature. As the temperature of the sample rises, so it emits light as a blackbody according to Planck's law modified with an appropriate emissivity. Then, by measuring the emission spectrum of the sample one can therefore determine the temperature profile of the sample. However, the emittance or emissivity must be known to convert radiant heat transfer measurements to temperature and it is important that emittance be properly determined for the real material being studied in order to obtain accurate temperature measurements [15].

Chapter 3

Instrumentation

3.1 Introduction

This chapter addresses the main techniques used to characterise the industrial diamond in this study, such as Raman spectroscopy, scanning electron microscopy and x-ray diffraction. Spectro-radiometric technique and laser principles are also discussed in this chapter.

3.2 Raman spectroscopy

Raman spectroscopy is a useful technique for the identification of a wide range of substances like solids, liquids, and gases. It is a non-destructive technique requiring no sample preparation. It involves illuminating a sample with monochromatic light and using a spectrometer to examine light scattered by the sample.

Raman spectroscopy refers to scattered light from a sample that exhibits a frequency shift corresponding to the energy of specific molecular vibrations. It provides a chemical composition of the sample. At the molecular level, photons can interact with matter by absorption or scattering processes. Scattering may occur either elastically, or inelastically. Raman spectroscopy relies on inelastic scattering or Raman scattering of monochromatic light, usually from a laser in the visible, near infrared, or near ultraviolet range.

Raman scattering occurs when the system exchanges energy with the photon and the system subsequently decays to vibrational energy levels above or below that of the initial state. The frequency shift corresponding to the energy difference between the incident and scattered photon is termed the Raman shift. The Raman shift occurs either as up or down shift of the scattered photon frequency relative to that of the incident photon and it depends on whether the system has lost or gained vibrational energy. The down-shifted and up-shifted components are called stokes and anti-stokes lines, respectively. Raman spectrum is given by a number of photons detected versus Raman shift from the incident laser energy [25].

Lasers are used as a photon source due to their highly monochromatic nature, and high beam fluxes. Light or laser beam from the sample passes back through the microscope optics into

the spectrometer. Charge-coupled device (CCD) detector is used to detect the Raman shifted radiation and a computer is used for data acquisition and curve fitting.

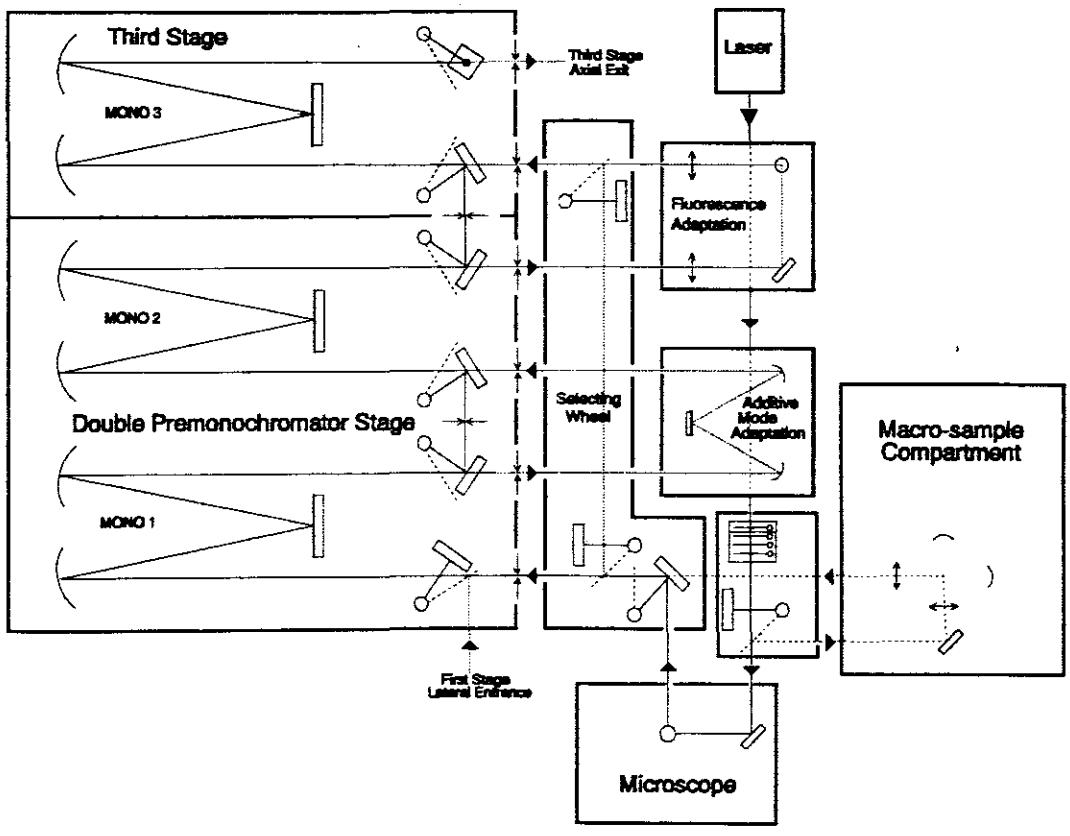

Figure 3.1: Optical diagram of a Jobin-Yvon T64000 Raman spectrometer.

Figure 3.1 is an optical diagram of a Jobin-Yvon T64000 Raman spectrometer that was used in this study. The T64000 configuration is composed of a double subtractive pre-monochromator (mono 1 and 2) and a spectrograph stage (mono 3) as shown in figure 3.1. The pre-monochromator is a double monochromator (1800 gr/mm gratings) working in a subtractive mode. It acts as a tuneable filter in the spectral range defined by the scanning mechanism and the gratings. The polychromatic radiation is limited to a specific wavelength range $\lambda_1 - \lambda_2$ at the exit of the pre-monochromator. The elastic radiation has to be outside this range.

The spectrograph stage is used as disperser. It is equipped with a two grating-turret: 1800 gr/mm and 600 gr/mm. The polychromatic radiation $\lambda_1 - \lambda_2$, selected by the pre-monochromator, is dispersed by the grating of the spectrograph stage. The spectrum is

acquired with a multi-channel detector, a Charge Coupled Device (CCD) detector, cooled by liquid nitrogen down to 140 K. The CCD detector is mounted in the plane of the exit image. The T64000 system can work in single spectrograph configuration. In this configuration, the elastic radiation is removed by using an appropriate holographic notch filter. The T64000 is equipped with a confocal microscope that permits experiments on small size samples, with an improved spatial, lateral and depth resolution. The total spectrum is acquired spectral band by spectral band. Each spectral band is measured for a specific grating position. The width of the spectral band depends on the scattered light and the grating used (600 gr/mm or 1800 gr/mm).

Different lasers may be used in conjunction with the T64000: an argon laser (the main lines are 514.5 nm and 488 nm), mixed laser argon with main lines 647.1 nm, 514.5 nm and 476.7 nm and dye laser providing incident radiation between 600 and 640 nm.

3.3 Scanning electron microscopy

A scanning electron microscopy (SEM) is similar to the transmission electron microscopy (TEM) because they both employ a beam of electrons directed at the specimen. They both have similar features such as the electron gun, condenser lenses and vacuum system but the way in which the images are produced and magnified are entirely different. TEM provides information about the internal structure of thin specimens while SEM is primarily used to study the surface, or near surface, structure of bulk specimens.

SEM, as its name suggests, is an instrument that produces mostly a magnified image by using electrons instead of light. Figure 3.2 is a schematic diagram showing the main components and the mode of operation of a simple SEM. The electron gun or source is usually of the tungsten filament thermionic emission type. The electrons are accelerated to an energy, which is usually between 1 keV, and 30 keV, which is

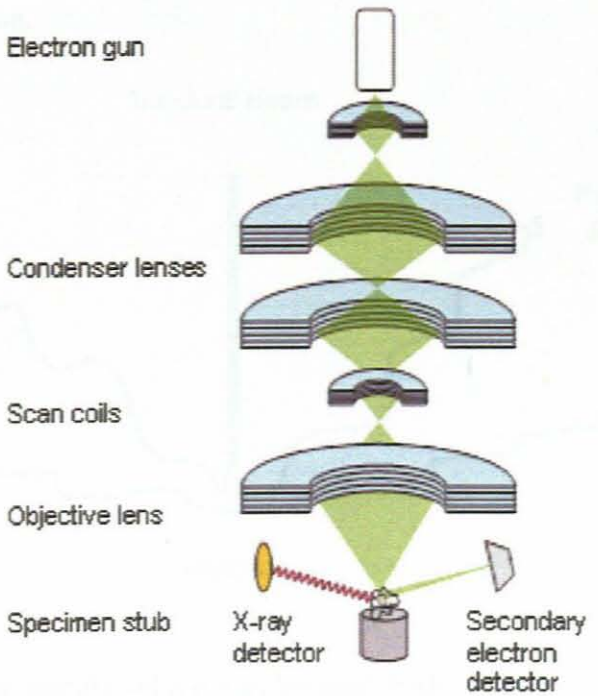

Figure 3.2: An illustration of a typical scanning electron microscopy that was employed in the present study [www.steve.gb.com/science/electron_microscopy].

considerably lower than the energies typical of the TEM (100 – 300 keV) [26]. An electron gun or source produces a beam of electrons at the top of the microscope. Then the beam travels through condenser lenses, which demagnify the electron beam until it hits the specimen as shown in figure 3.3. Usually, in older instruments, the fine beam of electrons is scanned across the specimen by the scan coils, while a detector counts the number of low energy secondary electrons. The same effect in modern instruments is achieved by digitally controlling the beam position on the specimen and the resultant image is displayed on a computer screen.

SEM requires a preparation procedure of specimen before examination. For effective viewing of a specimen in the SEM it is usually necessary for the surface of the specimen to be electrically conducting. During normal operation there is a surplus of electrons building up on the specimen surface. The surface becomes negatively charged until very soon the incoming primary electrons are repelled and deviated from their normal path, and a distorted image will

be formed. Therefore specimen must be coated with a thin conducting layer of gold or carbon before SEM examination.

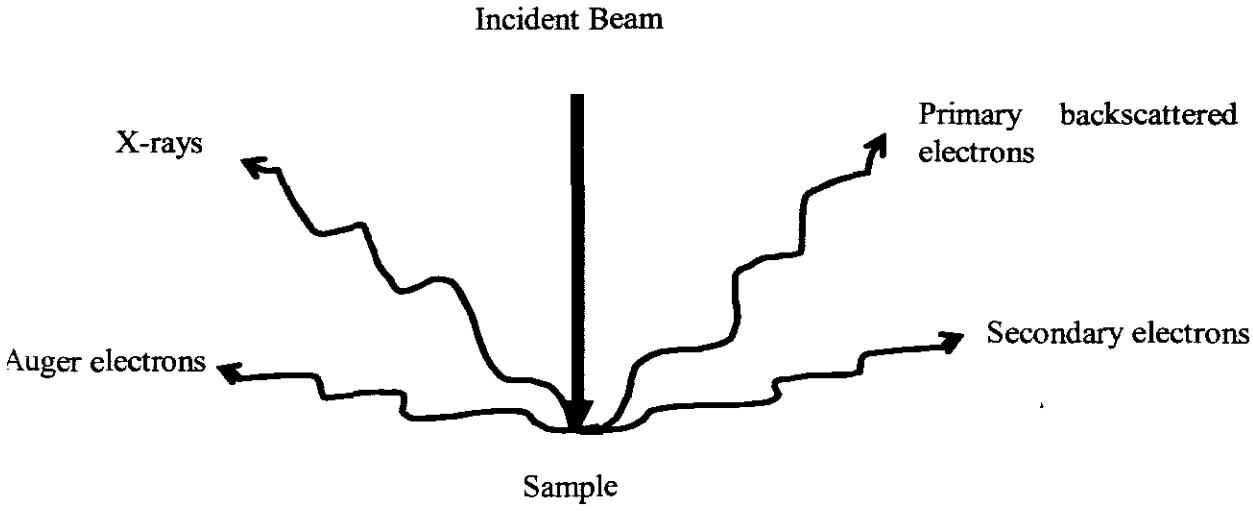

Figure 3.3: Some of the signals, which may be used in the SEM.

All SEMs normally have facilities for detecting secondary electrons, backscattered electrons and x-rays. X-rays are used for chemical analysis rather than imaging. In principle they are two things that can be determined from the x-ray spectrum emitted by the specimen that are: measurement of the wavelength or energy of each characteristics x-ray that is emitted enables us to find out which elements are present in the specimen (qualitative analysis), measurement of how many x-rays of any type are emitted per second should also tell us how much of the element is present (quantitative analysis). Therefore, many SEMs are equipped with energy dispersive spectrometer (EDS) detection system, which is able to detect and display most of the x-ray spectrum.

Energy dispersive x-ray analysis is sometimes referred to EDS or EDX and etc. It is a technique used for identifying the elemental composition of the specimen. EDX is a result of electron interaction with atoms. EDX analysis takes place inside the scanning microscopy when the specimen is bombarded with an electron beam. The incoming (primary) electron collides with electrons in the shells (K, L, and M, N ... as shown in figure 3.4) of the atom, thereby emitting electromagnetic radiation in the form of x-rays. The amount of energy released by the transferring electron depends on which shell it is transfer from, as well as which shell it is transferring to. The atom of every element releases x-rays with unique amounts of energy during the transferring process. Thus, by measuring the amounts of energy

present in the x-rays being released by a specimen during electron beam bombardment, the identity of the atom from which the x-ray was emitted can be established.

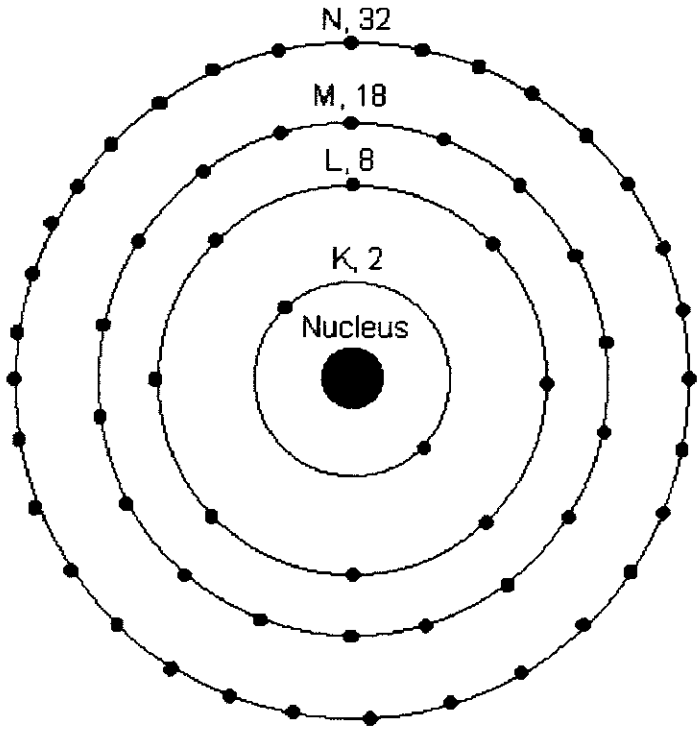

Figure 3.4: Typical diagram of electrons orbit around the nucleus in different shells, labelled from the innermost shell as K, L, M, N, etc. Each shell can have a certain number of electrons.

The output of an EDX analysis is an EDX spectrum as shown in figure 3.5. The EDX spectrum is just a plot of how frequently an x-ray is received for each energy level. The EDX spectrum normally displays peaks corresponding to the energy levels for which the most x-rays had been received. Each of these peaks are unique to an atom, and corresponds to a single element. Therefore the peak serves as a fingerprint of that element.

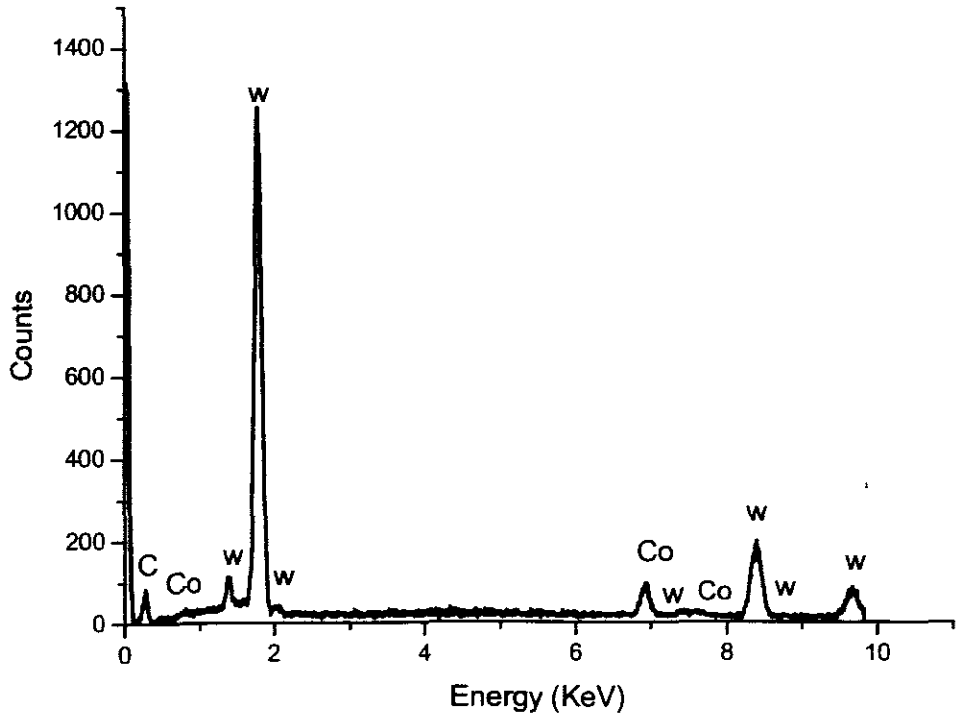

Figure 3.5: Typical EDX spectrum (that X-ray intensity as finger-prints of elements in the sample).

In the present study the investigation of morphology and qualitative analyses of industrial diamond were performed using SEM LEO 1525. The SEM LEO 1525 is fitted with Oxford Instruments INCA energy dispersive and wavelength dispersive x-ray spectrometer. Oxford Instruments INCA energy dispersive and wavelength dispersive x-ray spectrometer are useful for many material investigations such as chemical composition analysis, elementary detection (spectra), distribution detection (mapping) and simultaneous detection of 30 elements. This SEM has high resolution and image quality of 1.5 nm at 20 kV and 3.5 nm at 1 kV for metallic and non metallic materials and also magnification of 20 – 500 000 X for morphological characterisation.

3.4 X-ray powder diffraction

X-rays are a form of electromagnetic radiation with high energies and short wavelengths. They occur in that portion of the electromagnetic spectrum between gamma-rays and the ultraviolet. X-ray diffraction has been used in two main areas: fingerprint characterisation of crystalline materials and the determination of their structures chemical.

X-ray diffraction (XRD) is a method by which x-rays of known wavelengths are passed through a sample to be identified in order to identify the crystal structure. When a sample is irradiated with a parallel beam of monochromatic x-rays, the atomic lattice of the sample acts as a three dimensional diffraction grating causing the x-ray beam to be diffracted to specific angles. The diffraction pattern, that includes position (angles) and intensities of the diffraction beam, provides information about the sample: the angles are used to calculate the d-spacing and the position (d) of diffracted peaks also provides information about how the atoms are arranged within the crystalline compound [27].

In x-ray powder diffractometry, x-rays are generated within a sealed tube that is under vacuum. A current is applied that heats a filament within the tube, the higher the current the greater the number of electrons emitted from the filament. 15 – 60 Kilovolts is the range of voltage that is normally applied within the tube. This high voltage accelerates the electrons, which then hit a target, commonly made of copper. X-rays are produced when these electrons hit the target. The wavelength of these x-rays is characteristic of that target. A detector measure the x-ray signal and the signal then processed either by a microprocessor or electronically, converting the signal to a count rate. X-ray scan is performed by changing the angle between the x-ray source, the sample and the detector at a controlled rate between present limits. The distance between the planes of atoms that constitute the sample can be measure during the time an x-ray beam hits a sample and diffracted by applying Bragg's law. Bragg's law is $n\lambda = 2d_{hkl} \sin\theta$, where the integer n is the order of the diffracted beam, d is the distance between adjacent planes of atoms (the d-spacing) λ is the wavelength of the x-rays and θ is the angle of incidence of the x-ray beam. The geometry of an XRD unit is designed to accommodate this measurement (figure 3.6). The characteristics set of d-spacing generated in a typical x-ray scan provide a unique "fingerprint" of the elements present in the sample. When properly interpreted, by comparison with standard reference patterns and measurements, this "fingerprint" allows for identification of the material [28].

X-ray diffraction set up requires an x-ray source, the sample under investigation and a detector to collect the diffracted x-rays. Figure 3.6 is a schematic diagram of an x-ray diffractometer. When the incident beam strikes a sample, diffraction occurs in every possible orientation of 2θ. The diffracted beam may be detected by using a moveable detector such as

a Geiger counter, which is connected to a chart recorded. In general, the counter is set to scan over a range of 2θ values at a constant angular velocity [29].

The powder x-ray diffraction generator used in this study was a Phillips PW 1830 generator operating at 45 kV and 40 mA. A Phillips x-rays diffractometer equipped with a graphite monochromator and a copper tube is used to collect the powder data. The data is collected on a PC and analyzed using a computerized search and standard reference patterns.

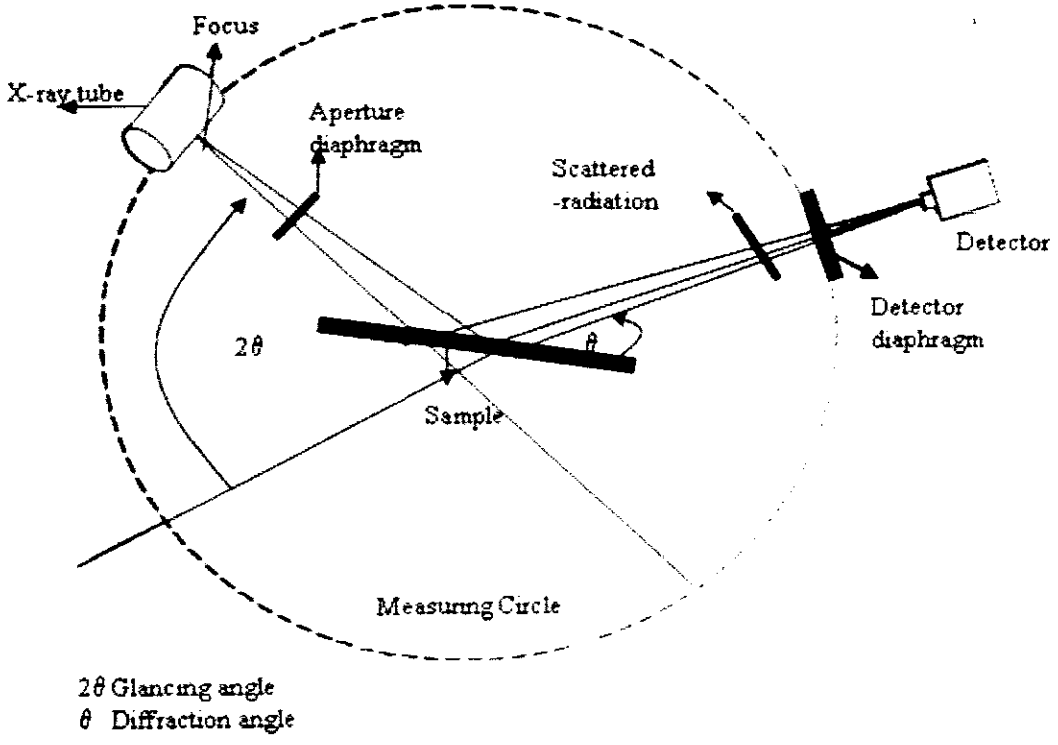

Figure 3.6: Schematic diagram of an X-ray diffraction. The x-rays are scattered through 2θ and focused to an image plate/detector for data recording.

3.5 Laser

A laser is a device that amplifies light and produces a highly directional, high-intensity beam that most often has a very pure frequency or wavelength [30]. Lasers come in sizes ranging from approximately one tenth the diameter of a human hair to the sizes of a very large building, in powers ranging from 10^{-9} to 10^{20} Watts, and in wavelengths ranging from the microwave to the soft-x-ray spectral regions with corresponding frequencies from 10^{11} to 10^{17}

Hz. It has pulse energies as high as 10^4 Joules and pulse durations as short as 5×10^{-15} seconds. Lasers can easily drill holes in the most durable of materials and can weld detached retinas within the human eye.

3.5.1 Definition of a laser

The word LASER is an acronym for Light Amplification by Stimulated Emission of Radiation. All lasers have some unique characteristics but they function under similar principles. There are three important components of a laser system. First, all lasers contain a gain or laser medium or active material which may be a collection of atoms, molecules or ions. The active material can be anything: gas, solid, liquid or a semiconductor. Second, lasers have an excitation source called a pump or power supply, which is required to excite the atoms from a lower energy state to a higher energy state. An optical cavity or resonator is another basic requirement for a laser. This consists of a set of mirrors M_1 and M_2 with the active material in between them to form a resonator. One of the mirrors is 100% reflective and the other one is partially reflective.

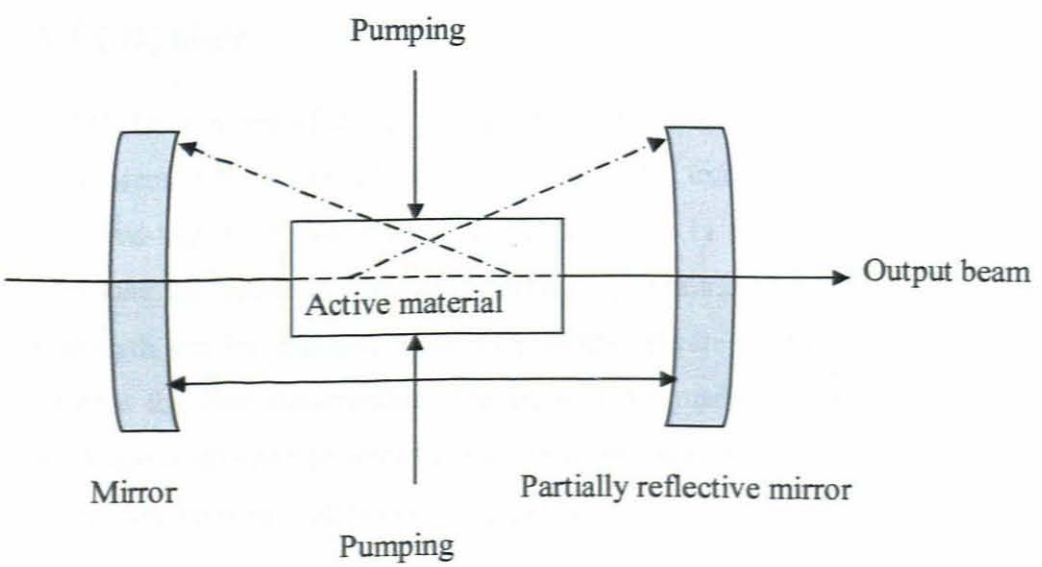

Figure 3.7: Basic components of a laser system.

In a laser, a laser medium is energized or pumped, by the external energy source (source of excitation). The pump energy is absorbed by a laser medium, placing some of its particles into a high energy level (excited). Particles can interact with light either by absorbing photons or by emitting photons. Emission can be spontaneous or stimulated. Some of the spontaneously emitted photons run in a direction parallel to the lasing medium, so they bounce back and

forth off the mirrors. As they pass through the gain medium, they stimulate emission in other excited atoms. Monochromatic, single-phase, collimated light leaves the lasing medium through the partially reflective mirror. There are many different types of lasers. Lasers are commonly given a name by the type of lasing material employed, for example, Solid-state lasers have a lasing material distributed in a solid matrix, while gas lasers like HeNe laser and CO_2 laser have a gas medium.

3.5.2 Unique properties of a laser

A typical laser that generates a beam of light can have many properties that are unique. Lasers generally have a narrower frequency distribution, much higher intensity, a much greater degree of collimation and much shorter pulse duration, than that available from more common types of light sources. Therefore, lasers are useful in compact disc players, in supermarket checkout scanners, in surveying instruments, and in medical applications such as surgical knives.

3.5.3 CO_2 laser

The CO_2 laser is one of the earliest gas lasers to be developed [30] and it is one of the most useful lasers. A CO_2 laser can emit high-power due to its high efficiency. It produces a beam of infrared light in the wavelength bands from 9 to 11 micrometers. CO_2 lasers can be tuned by rotating an internal diffraction grating. By rotating the diffraction grating, a particular wavelength can be selected. Since CO_2 lasers operate in the infrared, special materials are important for their construction. The mirrors are made of coated silicon, molybdenum, or gold, while windows and lenses are made of germanium or zinc selenide. The CO_2 laser can have powers between milliwatts and gigawatts.

CO_2 lasers are increasingly being used in industry for many different material processes due to their many advantages including high power density, high energy levels and high directionality. These industrial applications include heat-treatment to modify surface structures through intense heating followed by cooling; melting the surface layer to modify the properties such as wear and corrosion, drilling and cutting that involve melting and ablation of materials.

3.5.4 Operation Principles of CO_2 lasers

The basic principles of most CO_2 lasers are similar to that of any other gas laser. In general a gas laser consists of a low-pressure gas-filled vessel called the laser tube located between two mirrors that form an optical cavity. The gas in the tube called the laser medium can consist of atoms, and molecules. Laser action is usually obtained in the gas by pumping it by an electrical discharge; the energetic electrons provided by the discharge collide with the active gas atoms, exciting them to a higher energy level from which they automatically drop down to a lower energy by emitting a photon. HeNe lasers are based on excited atoms and CO_2 lasers use a population inversion in the vibrational energy states of CO_2 molecules mixed with other gases. The population inversion is the number of atoms in the excited state versus the number in the ground state [31].

The usual gas fill in a CO_2 laser is carbon dioxide, nitrogen, and helium. Typically, the gas fill contains the mixture of 7% carbon dioxide, 18% nitrogen and 75% helium. The CO_2 laser is a 3-energy level system. The energy of excited nitrogen molecules provides the energy needed to raise CO_2 molecules from the ground state to energy level 3. The helium in the mixture has two functions: helium atoms mixed together with CO_2 molecules at energy level 2, helping them return to the ground state, and it improves the thermal conductivity of the gas mixture [31-32].

Excitation transfer from the N_2 pumps the upper CO_2 laser level and N_2 itself is excited by electron impact. The relevant energy levels of the CO_2 and N_2 molecules are vibrational-rotational levels of their electronic ground states. The vibrational-rotational characteristics of the CO_2 molecule are discussed below. The CO_2 and N_2 vibrational energy levels are shown in figure 3.8.

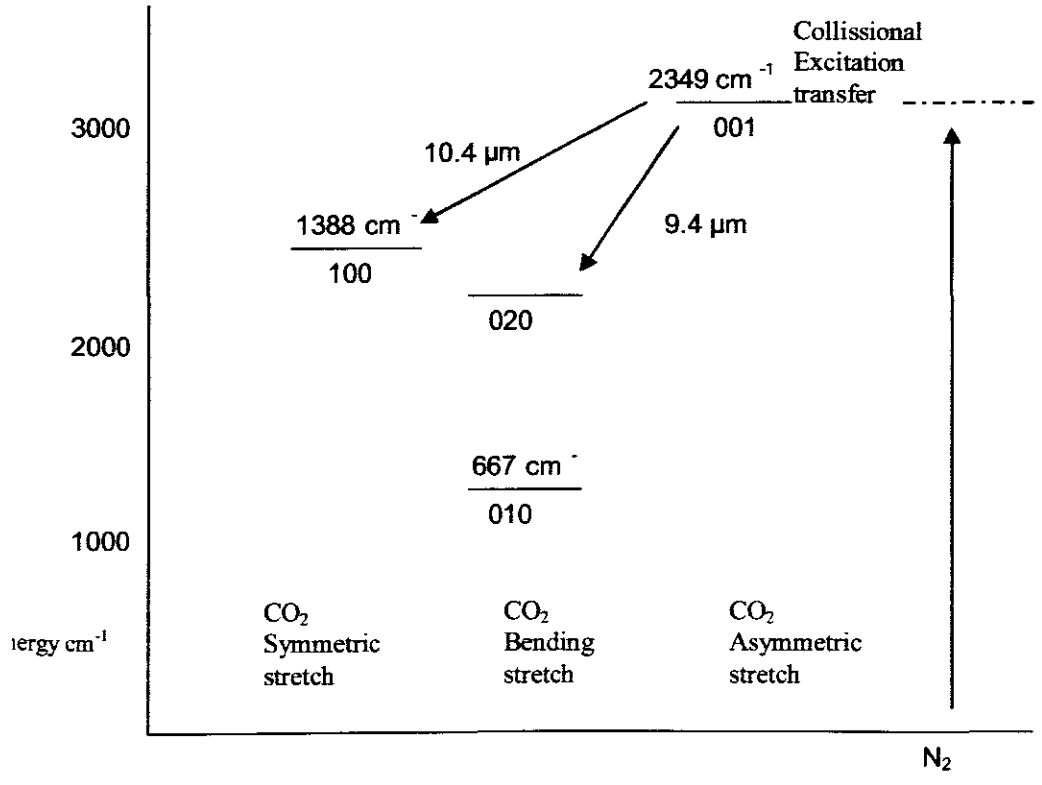

Figure 3.8: Vibrational energy levels of CO_2 and N_2. The energies are given in cm^{-1}.

3.5.5 Molecular vibration

The CO_2 laser is characterised by the vibrational and rotational transition states in the CO_2 molecules, and the molecules act like simple harmonic oscillators in three distinct ways. Three characteristic vibrational modes exist: the symmetric mode (where the two oxygen atoms vibrate against each other), the bending mode (where the carbon atoms move out of the molecular axis) and the asymmetric mode (where the two oxygen atoms oscillate against the carbon atoms) [31-33].

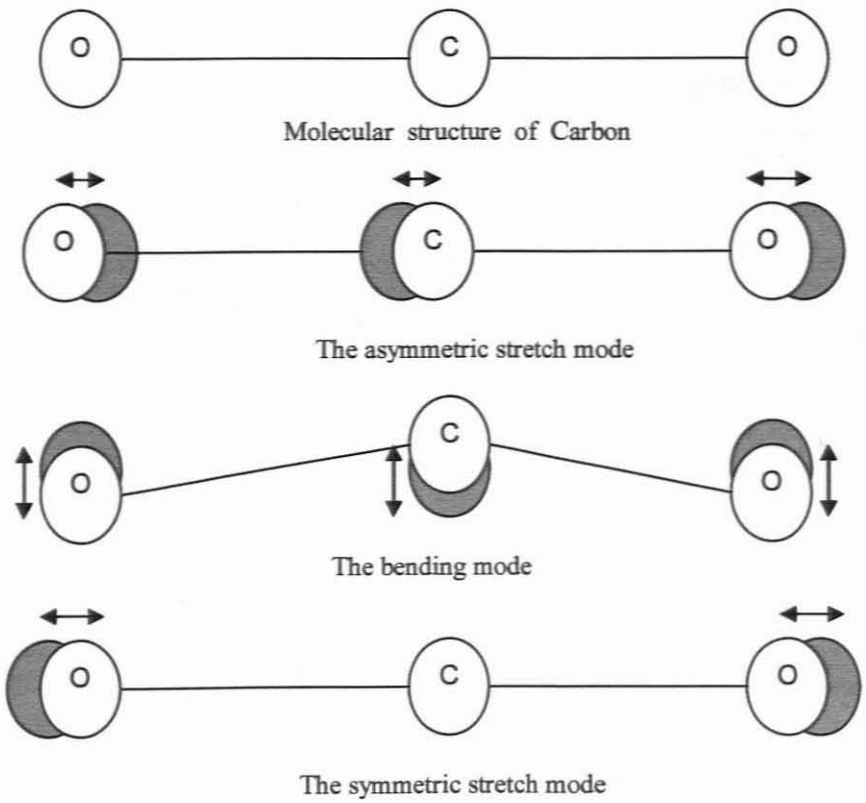

Figure 3.9: The carbon dioxide (CO_2) is a linear triatomic molecule and the normal modes of vibration of the CO_2 molecules: the asymmetric stretch mode, the bending mode and the symmetric stretch mode.

Each of these normal modes is associated with the characteristics frequency of vibration and each mode of vibration has a ladder of allowed energy levels associated with it, as in the case of a diatomic molecule. The vibrational energy levels of the molecule may then be labelled by three integers $v1$, $v2$ and $v3$ and approximately:

$$E(v1,v2,v3) = hc\omega_e^1\left(v1+\frac{1}{2}\right)+hc\omega_e^2\left(v2+\frac{1}{2}\right)+hc\omega_e^3\left(v3+\frac{1}{2}\right)$$

where ω_e^1, ω_e^2 and ω_e^3 are the normal-modes frequencies in units of wave numbers. The normal-modes frequencies for CO_2 are shown in figure 3.10 [34]:

ω_e^1 = ω (Symmetric stretch) ≈1388 cm^{-1}

ω_e^2 = ω (Bending) ≈667 cm^{-1}

ω_e^3 = ω (Asymmetric stretch) ≈2349 cm^{-1}

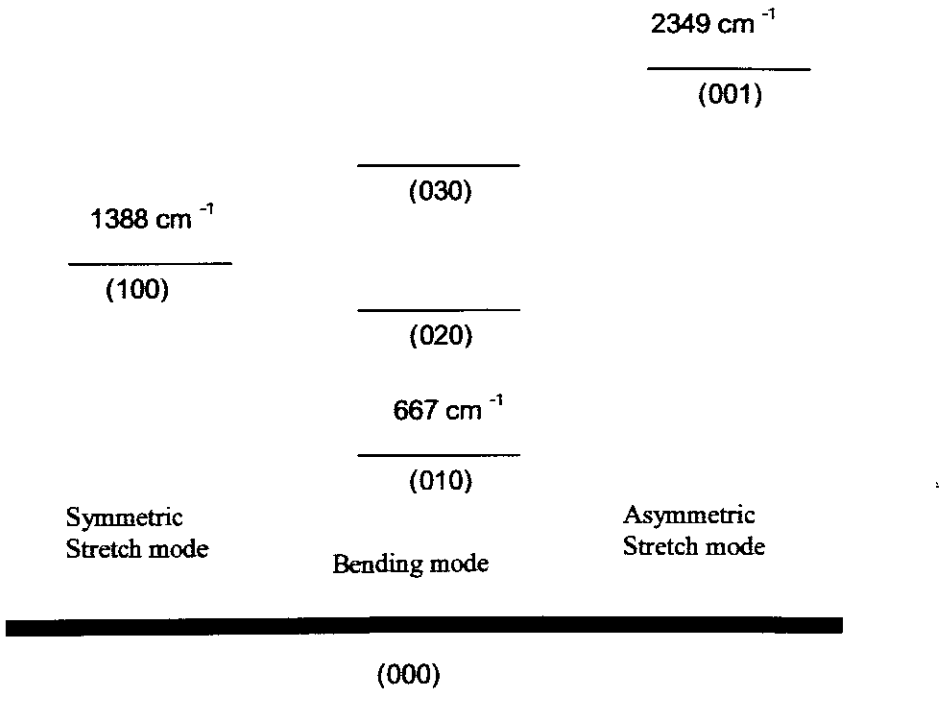

Figure 3.10: The first few vibrational energy levels of the CO_2 molecule.

CO_2 is a linear molecule; its rotational energy spectrum has the same characteristics as that for diatomic molecules. Since the CO_2 molecule is free to rotate, the total angular momentum (J) or rotational quantum number divides each vibrational level, whose value is either 0 or a positive integer. The selection rules for vibrational-rotational transitions in the CO_2 molecule are $\Delta J = +1$, giving the so-called P-branch transitions, and $\Delta J = -1$, giving the R-branch transitions. Individual transitions are denoted by the letter P or R [31, 33].

3.5.6 PL6 CO_2 laser

The type of laser used in this study was the CO_2 laser from Edinburgh Instruments PL6 model as shown in figure 3.11. This laser is a wavelength tuneable continuous (cw) CO_2 laser and is operating in the infrared region. Tuneability of the laser wavelength is possible with intracavity-mounted grating or micrometer, allowing line tuneable output in the 9.2 μm to 11 μm range. It has a peak power ~50 Watts at a wavelength of 10.6 μm.

The CO_2 laser system consists of a gas cylinder, gas controller, chiller, power supply and a laser head as is shown in figure 3.11. The CO_2 laser requires water-cooling. The water flows down the end of the tube into the laser for a few seconds and flows out to the chiller. The laser

head consists of a shutter (For closing and opening the laser beam). The active medium in CO_2 laser is a mixture of 7% carbon dioxide, 18 % nitrogen and 75% helium. The gases are mixed in a gas cylinder and into one end of discharge tube at a pressure of 5-3 mbar.

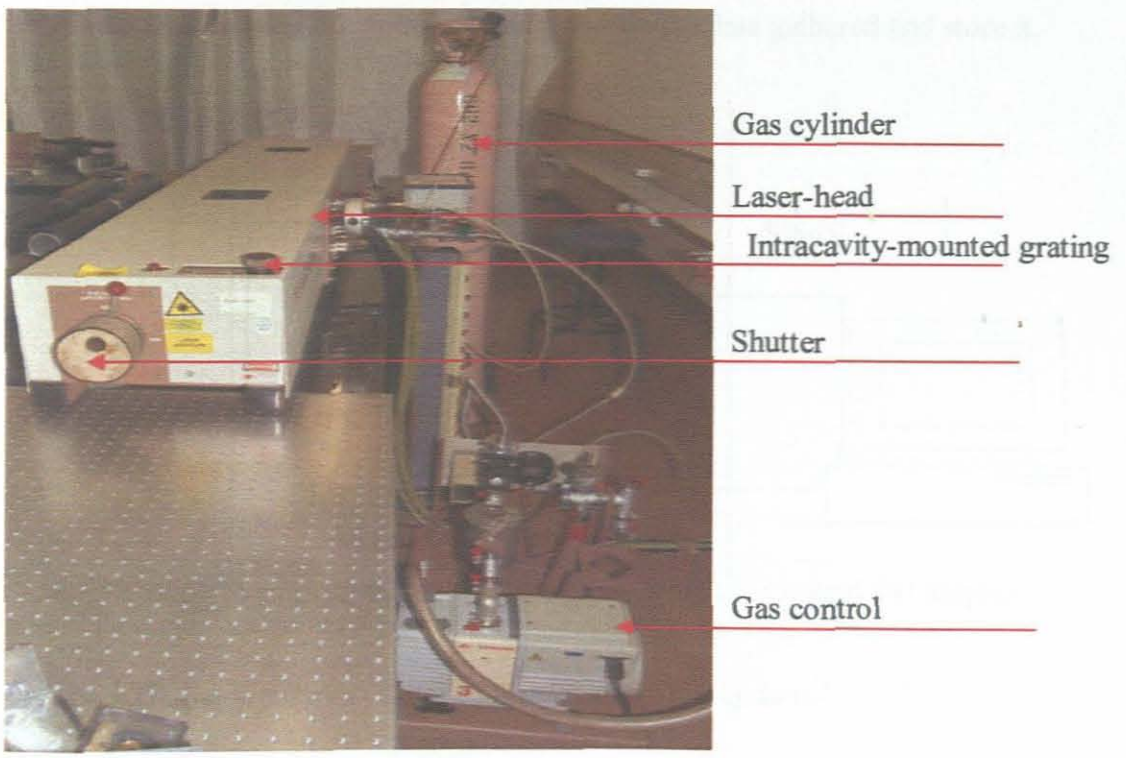

Figure 3.11: A photograph of the CO_2 laser used in the present work.

3.6 Spectro-radiometric method

Spectroradiometry is defined as a technique of measuring the spectrum of radiation emitted by a source [35-36]. The radiation must be separated into its component wavebands and each band measured separately. The characteristics of the source are provided by a spectrum of intensity against wavelength. The measured radiation may be expressed in a number of ways, depending on how the radiation entering the spectroradiometer is collected and how the system software processes it. When the spectrum of radiation emitted by a source is known, then its chemical or biological effect on a system can be calculated. The choice of spectroradiometer's components and specifications will depend very much on the use for which it is intended. Generally a spectroradiometer system consists of four basic units [37]:

1. The input optics that gather radiation from a specified field of view and deliver it to the monochromator.
2. A monochromator that separates the radiation into its component wavelengths.
3. A detector that measures the radiation at each wavelength.
4. A control and logging system to define the data gathered and store it.

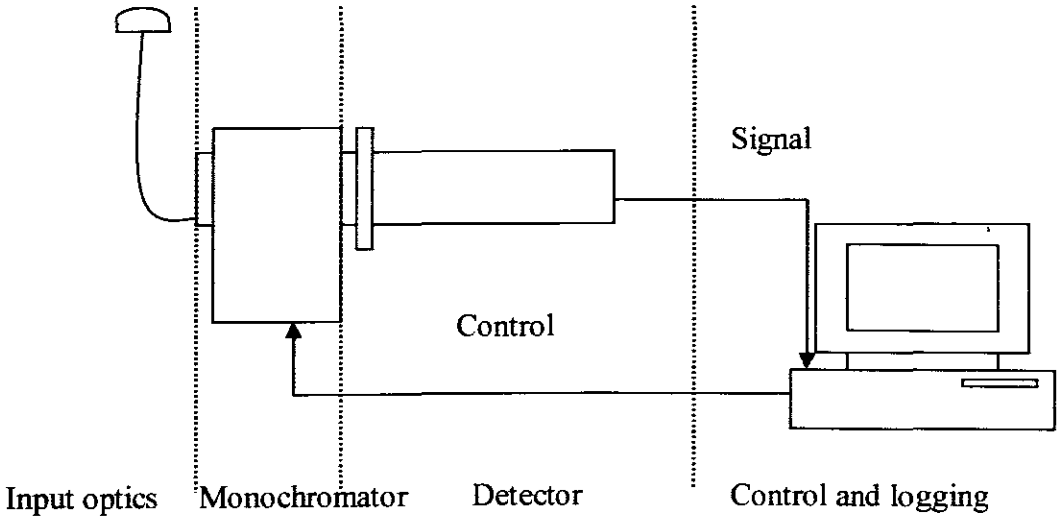

Figure 3.12: Basic components of a spectroradiometer system.

3.6.1 The monochromator

Figure 3.13 shows the monochromator (double monochromators), the central unit of a spectroradiometer [35]. Monochromator consists of entrance and exit slits, collimating and focusing optics, and wavelength dispersing element such as a grating or prism. Within the monochromators, the first element to select is that which will separate the radiation into its distinct wavebands, a task that may be performed by a prism or a diffraction grating. Most common dispersers are diffraction gratings because although prisms are more robust, gratings have a number of optical advantages. Therefore, the more lines/mm the better the dispersion and the higher the resolution.

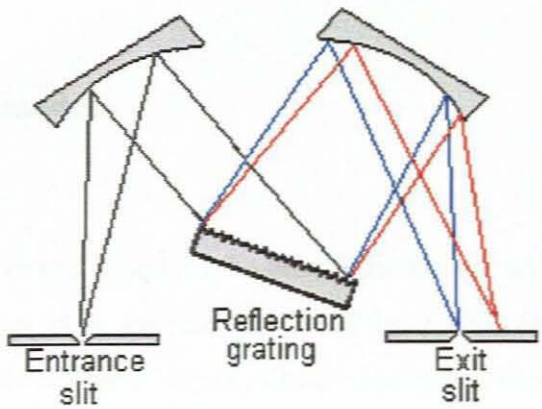

Figure 3.13: Elements of a double monochromator [38].

3.6.2 Input Optics

The radiation that enters the monochromator will depend on the input optics. The input optics (telescope or baffled tube) are required to be at the right angular field of view, in order to collect radiation from the source. The waveband of radiation which will reach the monochromator will be determined by the material used such as lenses, filters, for example optical fibres are needed [36]. The input optics must be tailored to suit the needs of the operator, not only for optical properties but also for other practical considerations.

3.6.3 The detector

The function of a detector is to measure the intensity at each designated wavelength from the gathered radiation. The wavelength range, dynamic range and sensitivity required for the measurements determine a detector to be used for the experiment. The basic detector technologies fall into three groups that are photoemissive detectors, semiconductor devices and thermal detectors. There are many options and modes of operation available within each type of detectors.

3.6.4 The Control and logging system

The control and data logging associated with spectroradiometers are tasks most often performed by a personal computer. The method of control, the devices and communication lines between computer, monochromator and detector output should be optimised to match the desired features of the system.

Chapter 4

Temperature profile model

4.1 Introduction

In this study an analytical model based on the heat diffusion equation is developed to analyse the temperature distribution in a material irradiated by a CO_2 laser. The model is multi-dimensional and incorporates different types of beam characteristics and boundary conditions. This study is conducted to show the effect of various laser beam parameters and material properties on the laser heating process. Model prediction results of industrial diamond are presented and discussed in this chapter. In the present study, a time-dependent analytical model of laser heating process in case of cylindrical geometry has been considered. The numerical model of laser heating process described here is restricted only to surface temperature profile of the targeted material.

4.2 Mathematical model

The theoretical model of studying the surface of the material is based on the equation of heat diffusion or heat flow with a non-zero source term. In order to find the dynamic temperature distribution on the surface of the sample, the heat diffusion equation needs to be solved with a non-zero source term [39]:

$$\frac{\partial U}{\partial t} - D\nabla^2 U = Q(r) \tag{4.1}$$

with diffusivity $D = k/\rho C_p$ and U is the temperature of the sample. Here ρ is the density, k is the conductivity, C_p is the heat capacity of the material and $Q(r)$ is the source term of this study. Then we solved the equation with cylindrical coordinates $U(r, \Theta, z)$ and we assumed that U is dependent only on r and t. Therefore equation (4.1) becomes

$$\frac{\partial U(r,t)}{\partial t} - D\nabla^2 U(r,t) = Q(r). \tag{4.2}$$

where $U(r, t)$ is the temperature on the surface of the sample.

This problem can be formulated in terms of the Green's function approach, which leads to an integral solution given by [40]:

$$U(r,t)=\int_0^t \int_0^a Q(\xi,\tau)G(r,\xi,t-\tau)d\xi d\tau \tag{4.3}$$

and Green's functions are given in equation (4.4) and (4.5), respectively.

$$G(r,\xi,t)=\sum_{m=1}^{\infty}\frac{2\xi}{a^2 J_1^2(\alpha_m)}J_0\left(\alpha_m\frac{r}{a}\right)J_a\left(\alpha_m\frac{\xi}{a}\right)\exp\left(-\frac{D\alpha_m^2 t}{a^2}\right) \tag{4.4}$$

Here we have assumed (equation (4.4)) that $U(a, t) = 300$ K and that $U(r, 0) = 300$ K. The α_m terms are found from the solution to $J_0(\alpha_m) = 0$. Here a is the sample radius, J_x refers to a Bessel function of order x and r is the radius coordinate.

$$G(r,\xi,t)=\frac{2}{a^2}\xi+\frac{2}{a^2}\sum_{m=1}^{\infty}\frac{\xi}{J_0^2(\alpha_m)}J_0\left(\alpha_m\frac{r}{a}\right)J_a\left(\alpha_m\frac{\xi}{a}\right)\exp\left(-\frac{D\alpha_m^2 t}{a^2}\right) \tag{4.5}$$

Here we have assumed (equation (4.5)) that $\frac{\partial U}{\partial r} = 0$ at $r = a$. The α_m terms are positive zeros of the first-order of Bessel function, $J_1(\alpha_m) = 0$.

4.3 Source term equation

The source term of this study is the CO_2 laser, which is a continuous Gaussian beam, TEM_{00} mode and given by,

$$Q(r) = \frac{2P_0\alpha \exp\left(\frac{-2r^2}{\omega^2}\right)}{\rho l C_p \pi \omega^2}, \tag{4.6}$$

where the total power of the laser beam target is P_0, α is the absorption coefficient of the sample, ω is the laser beam radius at the target and l is the laser penetration depth. This was derived as follows: In order to raise the temperature of a body, to make it hotter, we must supply energy to it. The temperature of a body depends not only on the amount of energy supplied to it, but also on its size and nature. In order to be able to compare the abilities of different materials to absorb energy we use the quantity specific heat capacity. In other words, the amount of heat gained or lost is given by [41]

$$Q = mC_p\Delta T, \tag{4.7}$$

where Q is quantity of heat, m is mass, C_p is specific heat capacity and ΔT is change of temperature. For an extremely small temperature change dT and corresponding quantity of heat dQ,

$$dQ = mC_p dT. \tag{4.8}$$

And at the rate of time,

$$\frac{dQ}{dt} = mC_p \frac{dT}{dt}. \tag{4.9}$$

Let $Q = E, T = U$ and equation (4.9) is written in this form,

$$\frac{dE}{dt} = mC_p \frac{dU}{dt}, \tag{4.10}$$

where $m = \rho v$, ρ is the density and v is the volume. Rearrange the terms and we get this:

$$\frac{\frac{dE}{dt}}{\rho v C_p} = \frac{dU}{dt}. \tag{4.11}$$

The volume is given by $v = lA$, where l is the length and A is the area.

$$\frac{\frac{dE}{dt}}{\rho l A C_p} = \frac{dU}{dt}. \tag{4.12}$$

Since the intensity is given by $I = \frac{P}{A}$ and power is given by $P = \frac{dE}{dt}$ and equation (4.13) becomes:

$$\frac{I(r)}{\rho l C_p} = \frac{dU}{dt}. \tag{4.13}$$

Therefore the source term is given as

$$Q(r) = \frac{dU}{dt} = \frac{I(r)}{\rho l C_p}. \tag{4.14}$$

Note that not all laser intensity is absorbed by the material and then we modified the equation to include the absorption coefficient α and the equation becomes

$$Q(r) = \frac{I(r)\alpha}{\rho l C_p}, \tag{4.15}$$

where $I(r) = \frac{2P_0 \exp\left(\frac{-2r^2}{\omega^2}\right)}{\pi\omega^2}$ and then by substituting the intensity, the source term is given as:

$$Q(r) = \frac{2P_0\alpha \exp\left(\frac{-2r^2}{\omega^2}\right)}{\rho l C_p \pi\omega^2}. \tag{4.16}$$

The source term depends on the radial coordinate r, total power of the laser P_0, the beam size ω and also on the absorption coefficient α (how well the material absorbs heat). Varying the total power of the laser, the beam size and the radial coordinate then can vary the source. The

source term is directly proportional to the total power of the beam, meaning that the increase of the total power; result in increase of the source term.

4.3.1 Case 1: Heating of the material

The heating process caused by a laser beam was assumed to be due to absorption of the laser beam in the thin surface layer of the bulk material. The heating of the material was modelled as an equivalent surface thermal source with appropriate dynamic temperature distribution. This study focused on cylindrical samples and accordingly the temperature profile analysis was performed using the cylindrical coordinate system. Though this problem is a three-dimensional one, the temperature profile is a function of the radial coordinates and time coordinates only, thus the problem under consideration becomes a one-dimensional one. The geometry of the considered problem is shown in figure 4.1.

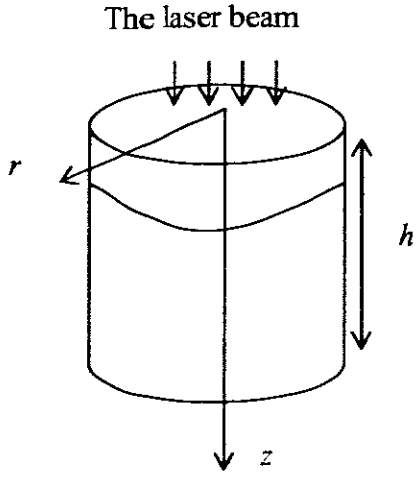

Figure 4.1: Geometry of the problem domain: r – radial coordinate, h – height of sample.

The following simplifying assumptions are made in defining the model: it was assumed that the dynamic temperature distributions of the laser beam intensity on the surface of the material samples could be described by a product of two independent functions of the radial coordinate and time, for example r and t, respectively. The source term of this study is the CO_2 laser, which is continuous Gaussian beam, TEM_{00} mode and the equation is given in equation (4.16). It was assumed that all the thermal parameters of the material of interest in the considered temperature range are constant and temperature independent.

The boundary conditions of this study are: the initial temperature profile on the surface of the material is at room temperature ($U(r,0)=300K$), initially, the temperature profile on the edge of the material is at room temperature or is constant ($U(a,t)=300K$) and also other boundary condition was that there is no heat flow on the material ($\frac{\partial U}{\partial r}=0$ at $r=a$). U is the temperature profile of the material, a is the radius of the material, t is time and r is the radial coordinate.

From equation (4.3) the temperature profile as function of time on the surface of the sample can be determine by substituting the source term given in equation (4.16) and the Green's function given in equation (4.4). The temperature profile as function of time on the surface of the sample is given as

$$U(r,t)=T_0+\sum_{m=1}^{\infty}\frac{2P_0\alpha}{\rho\ell c_p\pi\omega^2}\frac{2}{a^2J_1^2(\alpha_m)}J_0\left(\frac{\alpha_m r}{a}\right)\int_0^t\int_0^a\exp\left(-\frac{2\xi^2}{\omega^2}\right)\xi J_0\left(\alpha_m\frac{\xi}{a}\right)\exp\left(-\frac{D\alpha_m^2 t}{a^2}\right)d\xi dt, \tag{4.17}$$

The time integral can be solved analytically to yield:

$$U(r,t)=T_0+\frac{4P_0\alpha}{kl\pi\omega^2}\sum_{m=1}^{\infty}\frac{J_0\left(\alpha_m\frac{r}{a}\right)\left(1-\exp\left(-\frac{D\alpha_m^2 t}{a^2}\right)\right)\int_0^a\exp\left(-\frac{2\xi^2}{\omega^2}\right)\xi J_0\left(\alpha_m\frac{\xi}{a}\right)d\xi}{\alpha_m^2J_1^2(\alpha_m)}. \tag{4.18}$$

Integrating over the area of the sample and dividing with whole area of the sample as follows determine the average temperature on the surface of the sample:

$$\overline{U}(t)=\frac{\int_0^b\int_0^{2\pi}U(r,t)rdrd\theta}{\int_0^b\int_0^{2\pi}rdrd\theta}, \tag{4.19}$$

$$\overline{U}(t) = \frac{\int_0^b U(r,t) r dr}{\frac{b^2}{2}}, \tag{4.20}$$

where b is any distance within a ($b \leq a$). Then by substituting the function of $U(r,t)$ (equation (4.18)) in equation (4.20),

$$\overline{U}(t) = \frac{2}{b^2}\int_0^b T_0 r dr + \frac{8P_0\alpha}{b^2 kl\pi\omega^2}\sum_{m=1}^{\infty}\frac{\int_0^a \exp\left(-\frac{2\xi^2}{\omega^2}\right)\xi J_0\left(\alpha_m\frac{\xi}{a}\right)d\xi\left(1-\exp\left(-\frac{D\alpha_m^2}{a^2}\right)\right)}{\alpha_m^2 J_1^2(\alpha_m)}\int_0^b J_0\left(\alpha_m\frac{r}{a}\right)r dr$$

. (4.21)

Then, after appropriate calculus, the average temperature is given by

$$\overline{U}(t) = T_0 + \frac{8P_0\alpha}{b^2 kl\pi\omega^2}\sum_{m=1}^{\infty}\frac{\int_0^a \exp\left(-\frac{2\xi^2}{\omega^2}\right)\xi J_0\left(\alpha_m\frac{\xi}{a}\right)d\xi\left(1-\exp\left(-\frac{D\alpha_m^2}{a^2}\right)\right)}{\alpha_m^2 J_1^2(\alpha_m)}\frac{ab}{\alpha_m}J_1\left(\frac{\alpha_m b}{a}\right). \tag{4.22}$$

Here we have assumed (equation (4.18) and (4.21)) that $U(a, t)$ = 300 K and that $U(r, 0)$ = 300 K. The α_m terms are found from the solution to $J_0(\alpha_m) = 0$. Here a is the sample radius, J_x refers to a Bessel function of order x and r is the radius coordinate.

The equations (4.23) and (4.24) are for these boundary conditions: $U(a, t)$ = 300 K and $U(r, 0)$ = 300 K.

$$U(r,t) = T_0 + \frac{4P_0\alpha}{kl\pi\omega^2}\sum_{m=1}^{\infty}\frac{J_0\left(\alpha_m\frac{r}{a}\right)\left(1-\exp\left(-\frac{D\alpha_m^2 t}{a^2}\right)\right)\int_0^a \exp\left(-\frac{2\xi^2}{\omega^2}\right)\xi J_0\left(\alpha_m\frac{\xi}{a}\right)d\xi}{\alpha_m^2 J_1^2(\alpha_m)}, \tag{4.23}$$

$$\overline{U}(t)=T_0+\frac{8P_0\alpha}{b^2kl\pi\omega^2}\sum_{m=1}^{\infty}\frac{\int_0^a\exp\left(-\frac{2\xi^2}{\omega^2}\right)\xi J_0\left(\alpha_m\frac{\xi}{a}\right)d\xi\left(1-\exp\left(-\frac{D\alpha_m^2}{a^2}\right)\right)}{\alpha_m^2J_1^2(\alpha_m)}\frac{ab}{\alpha_m}J_1\left(\frac{\alpha_m b}{a}\right),$$

(4.24)

The equations (4.25) and (4.26) are for these boundary conditions: $\frac{\partial U}{\partial r}=300K$ at $r=a$.

$$U(r,t)=T_0+\frac{tP_0\alpha}{l\rho\pi a^2C_P}\left(1-\exp\left(\frac{-2a^2}{\omega^2}\right)\right)+\frac{4P_0\alpha}{l\rho\pi a^2\omega^2C_P}\sum_{m=1}^{\infty}\frac{J_0\left(\frac{\alpha_m r}{a}\right)\int_0^a\exp\left(\frac{-2\xi^2}{\omega^2}\right)\xi J_0\left(\frac{\alpha_m\xi}{a}\right)d\xi}{J_0(\alpha_m)}\frac{a^2}{D\alpha_m^2}\left(1-\exp\left(\frac{-D\alpha_m^2t}{a^2}\right)\right)$$

(4.25)

$$\overline{U}(t)=T_0+\frac{P_0t\alpha}{l\rho C_p\pi a^2}\left(1-\exp\left(\frac{-2a^2}{\omega^2}\right)\right)+\frac{8P_0\alpha}{l\rho C_pb^2\omega^2a^2}\sum_{m=1}^{\infty}\frac{\frac{ab}{\alpha_m}J_1\left(\frac{\alpha_m b}{a}\right)\int_0^a\exp\left(\frac{-2\xi^2}{\omega^2}\right)\xi J_0\left(\frac{\alpha_m\xi}{a}\right)d\xi}{J_0^2(\alpha_m)}\frac{a^2}{D\alpha_m^2}\left(1-\exp\left(\frac{-Dt\alpha_m^2}{a^2}\right)\right)$$

(4.26)

The four equations depend on how well the material absorbs heat (α), how small the beam is (ω), the total power of the laser (P_0) and also to the material properties (D). These four equations show that the temperature profile on the surface of the sample is decaying with time. The trend that the temperature profile on the surface of the sample follows is an exponential form.

4.3.2 Case 2: Cooling of the material

For the case when the laser is switched off (cooling of the sample) when the sample has a heat surface temperature given by $U(r, t_{off})$, the source term is zero. The heat diffusion equation is given as

$$\frac{\partial U(r,t)}{\partial t}-D\nabla^2U(r,t)=0. \qquad (4.27)$$

The above equation may be put into this form,

$$\frac{1}{D}\frac{\partial U(r,t)}{\partial t}-\nabla^2 U(r,t)=0. \tag{4.28}$$

The natural variable for the problem are cylindrical coordinates r, θ, z. The Laplace's equation in cylindrical coordinates is

$$\nabla^2 U=\frac{1}{r}\frac{\partial}{\partial r}\left(r\frac{\partial U}{\partial r}\right)+\frac{1}{r^2}\frac{\partial^2 U}{\partial \theta^2}+\frac{\partial^2 U}{\partial z^2}. \tag{4.29}$$

Putting this in equation (4.28), then the expression become this

$$\frac{1}{D}\frac{\partial U}{\partial t}-\frac{1}{r}\frac{\partial}{\partial r}\left(r\frac{\partial U}{\partial r}\right)-\frac{1}{r^2}\frac{\partial^2 U}{\partial \theta^2}-\frac{\partial^2 U}{\partial z^2}=0. \tag{4.30}$$

Then, after appropriate algebra or calculus, the expression becomes,

$$\frac{1}{D}\frac{\partial U}{\partial t}-\frac{\partial^2 U}{\partial r^2}-\frac{1}{r}\frac{\partial U}{\partial r}-\frac{1}{r^2}\frac{\partial^2 U}{\partial \theta^2}-\frac{\partial^2 U}{\partial z^2}=0. \tag{4.31}$$

Here the assumption is that U depends on r and t only then the expression becomes

$$\frac{1}{D}\frac{\partial U}{\partial t}-\frac{\partial^2 U}{\partial r^2}-\frac{1}{r}\frac{\partial U}{\partial r}=0. \tag{4.32}$$

Fourier's method of variable separation was used in order to transform the original PDE into two ordinary differential equations as follows [42]:

$$U=R(r)T(t). \tag{4.33}$$

Substituting equation (4.33) into equation (4.32) and dividing by RT gives,

$$\frac{1}{DT}\frac{dT}{dt}-\frac{1}{R}\frac{d^2R}{dr^2}-\frac{1}{rR}\frac{dR}{dr}=0. \tag{4.34}$$

First term is a function of t and last two terms functions of r, so we have two equations and set each side equal to a constant $-b^2$.

$$\frac{1}{DT}\frac{dT}{dt}=-b^2\,, \qquad \frac{1}{R}\frac{d^2R}{dr^2}+\frac{1}{rR}\frac{dR}{dr}=-b^2 \tag{4.35}$$

The time equation can be integrated to give this

$$T(t)=e^{-b^2Dt}. \tag{4.36}$$

The reason here for choosing the separation constant to be negative is that as t increases, the temperature of a body might decrease to zero as in equation (4.36), but it could not increase to infinity as it would if the constant is positive.

$$\frac{1}{R}\frac{d^2R}{dr^2}+\frac{1}{rR}\frac{dR}{dr}=-b^2. \tag{4.37}$$

Multiplying equation (4.37) with r^2R to get this

$$r^2\frac{d^2R}{dr^2}+r\frac{dR}{dr}+b^2r^2R=0. \tag{4.38}$$

This is a Bessel's equation with the solution of J_n *(br)* and N_n *(br)*. Since the base of the cylinder is considered to contain the origin, we use only the J_n and not the N_n solutions since N_n becomes infinite at the origin. Then we have

$$R(r)=J_0(br). \tag{4.39}$$

Thus the possible values of b are the zeros of J_n. The basic solutions for U is then

$$U(r,t)=e^{-b^2Dt}J_0(br). \tag{4.40}$$

Here it was assumed that $U\ (a,\ t)$ = 300 K and that $U\ (r,\ 0)$ = 300 K and the equation (4.40) becomes

$$U(a,t)=e^{-Db^2t}J_0(ba)=0. \tag{4.41}$$

$e^{-Db^2t}J_0(ba)=0$.

$J_0(ba)=0$.

Letting $\alpha_m = b_m a$ and $b_m = \frac{\alpha_m}{a}$. Therefore

$$J_0(\alpha_m)=0. \tag{4.42}$$

The possible values of α_m are the zeros of J_0, call these zeros α_m, $m = 1, 2, 3 \ldots$ Then there are infinite numbers of solutions of the form, and we shall write the solution of our problem as a series of such solutions (eigenfunctions),

$$U(r,t)=\sum_{m=1}^{\infty} C_m e^{-D\left(\frac{\alpha_m}{a}\right)^2 t} J_0\left(\frac{\alpha_m r}{a}\right). \tag{4.43}$$

Initial boundary conditions: It was assumed that when $t = 0$, $U = f(r)$. From equation (4.43):

$$U(r,0)=\sum_{m=1}^{\infty} C_m J_0\left(\frac{\alpha_m r}{a}\right)=f(r). \tag{4.44}$$

Here we want to expand $f(r)$ in a series of Bessel functions. Then we can find the coefficients C_m in equations (4.44) by the same method used in finding the coefficients in a Fourier sine or cosine series. This series is often called Fourier-Bessel series [42]. Multiply equation (4.44) by $rJ_0\left(\alpha_\mu \frac{r}{a}\right), \mu = 1,2,3\ldots$, and integrate term by term from $r = 0$ to $r = 1$. Because of the orthogonality all terms of the series drop out except the term with $m = \mu$, and we get

$$C_m \int r\left[J_0\left(\alpha_m \frac{r}{a}\right)\right]^2 dr = \int f(r) r J_0\left(\alpha_m \frac{r}{a}\right) dr. \tag{4.45}$$

For each value of $m = 1,2,3\ldots$, in equation (4.45) gives one of the coefficients in equation (4.44) and (4.45), thus any C_m in equation (4.44) is given by equation (4.45) with $u = m$. Then $\int r\left[J_0\left(\alpha_m \frac{r}{a}\right)\right]^2$ is given as $\int r\left[J_0\left(\alpha_m \frac{r}{a}\right)\right]^2 dr = \frac{a^2}{2} J_1^2(\alpha_m)$.

coordinate r is zero. The graph in figure 4.3 shows how the source term changes at various beam size. The source term can be calculated as follows:

$$Q(r) = \frac{2P_0\alpha \exp\left(\frac{-2r^2}{\omega^2}\right)}{\rho \ell c_p \pi \omega^2} \tag{4.49}$$

where ω^2 is given from the laser beam propagation equation:

$$\omega^2(z) = \left(\frac{M^2\lambda}{\pi\omega_0}\right)^2 z^2 - 2z_0\left(\frac{M^2\lambda}{\pi\omega_0}\right)^2 z + \left(\frac{M^2\lambda}{\pi\omega_0}\right)^2 z_0^2 + \omega_0^2. \tag{4.50}$$

The source terms is distributed across the sample, the peak value was calculated at $r = 0$ only and then equation (4.49) reduced to this

$$Q = \frac{2P_0\alpha}{\rho \ell c_p \pi \omega^2}. \tag{4.51}$$

Then the beam size from figure 4.2 was used to calculate the source term (given equation (4.51)) at various distances for minimum, medium and maximum power of the laser. The peak value of the source term at $r = 0$ versus the position of the beam size was plotted as shown in figure 4.3. This graph shows that at the waist of the beam the source term is high and is falling as the beam expand. This means that varying the size of the beam can vary the source term.

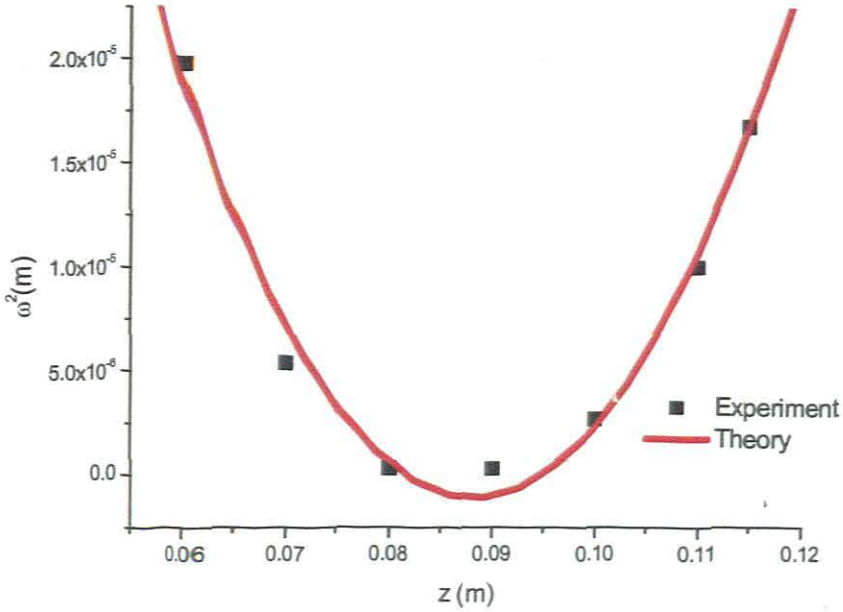

Figure 4.2: The beam size on the sample could be changed by moving the sample in and out of the focal region of the beam, thus modifying the source term equation (4.51).

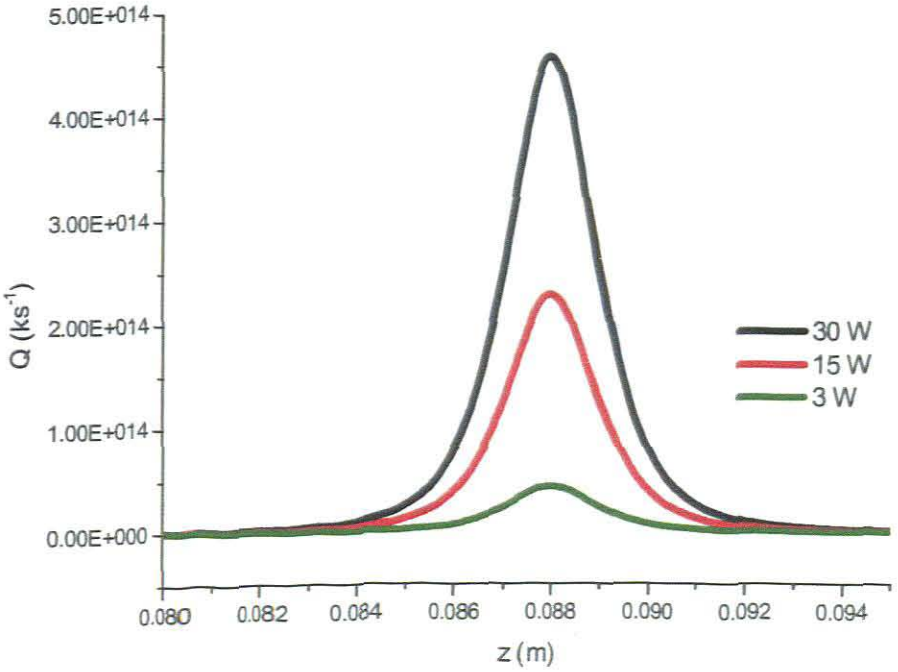

Figure 4.3: Calculation of the source term at various distances (from the focusing optic) during the laser beam propagation. Since the source term is distributed across the sample, we have plotted the peak value at $r = 0$ only.

4.4.2 Parameter study using diffusion equation solution

A parameter study is carried out to analyse the effect of different laser beam parameters such as beam size and defocused distance. Laser beam parameters and material properties are given in Table 4.1.

Table 4.1: Properties of material and laser beam parameters.

Material	Density ρ (kg/m^3)	Specific heat (J/kg. K)	Thermal conductivity (W/m. K)
Industrial diamond	3996	0.521	529.640
Laser beam spot size ω is 0.9 x 10^{-3} m			

4.4.3 Effects of laser beam size and time

The beam size along with beam power determines the power intensity distribution. Using lenses of different focal lengths varies the beam spot size. In this study, two different beam size ω, 0.5 mm and 1 mm are considered. A result for surface temperature is shown in figure 4.4. The dynamic temperature profile is computed based on the beam size given and by equation (4.23) for heating of the material.

Results show that surface temperature distribution closely resembles the Gaussian distribution of the incident laser beam. The maximum surface temperature increases as the beam size decreases from 1 mm to 0.5 mm. However, with the use of a smaller beam size, the higher beam intensity can be achieved that causes a significantly high temperature rise in the material. A smaller laser beam size not only causes high surface temperature, but also creates a wider and deeper heated region.

Figure 4.5 is temperature distribution on the surface of the sample at different times. The graph shows that the spatial variation in temperature in the sample is very rapid and falls off towards of the edges of the sample. Both the graphs (figure 4.4 and figure 4.5) mean that varying the beam size and time can vary the peak surface temperature of the sample.

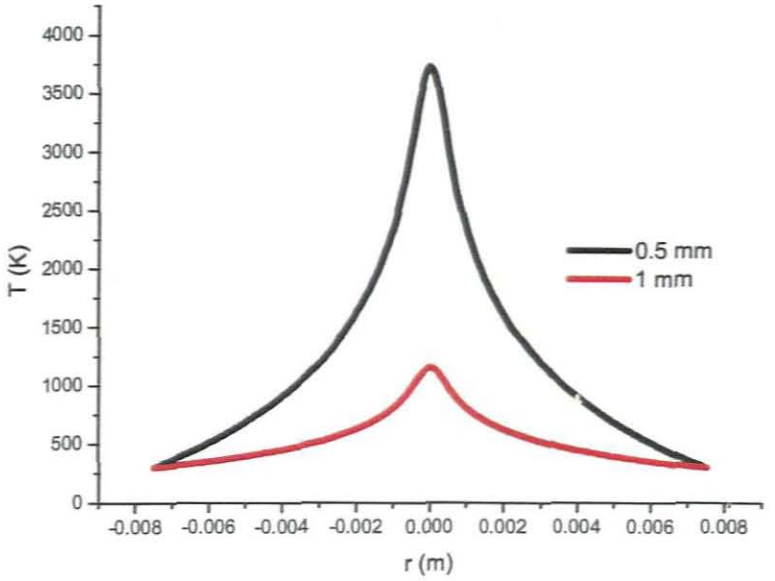

Figure 4.4: Effect of laser beam size ω on surface temperature distribution across the surface of the material and the parameters were assumed: $P_0 = 30$ W, $t = 100$ μs (Equation 4.23). This graph shows that the maximum surface temperature increases as the beam size decreases.

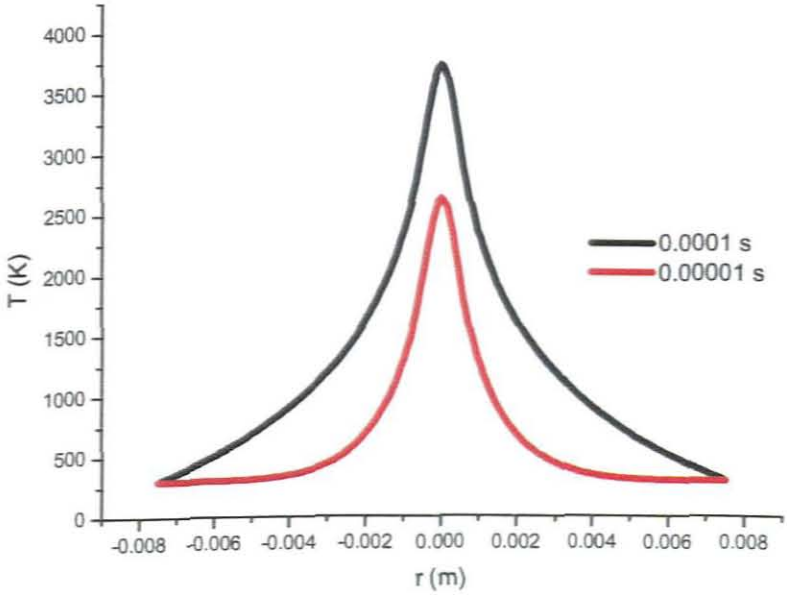

Figure 4.5: Effect of time on surface temperature distribution across the surface of the material and the parameters were assumed: $P_0 = 30$ W, $\omega = 1$ mm (Equation 4.23). This graph (figure 4.5) shows that the temperature rise in the sample is very fast and falls off towards the edges of the sample.

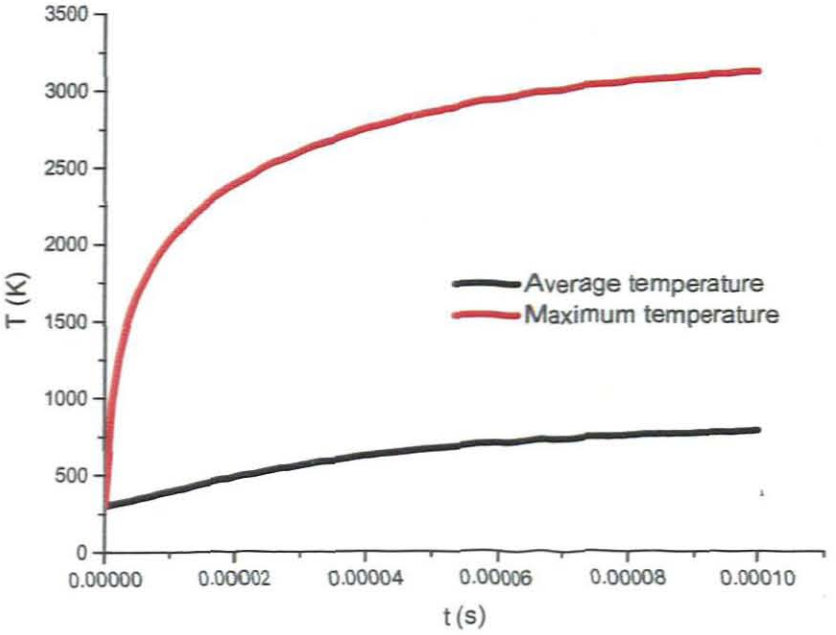

Figure 4.6: The peak (Equation 4.23) and average temperatures (Equation 4.24) rise in the micro-second scale, and stabilise after less than 1s. The average values in this calculation are much less than the peak due to a highly localised source term.

4.4.4 Comparison of the two boundary conditions for heating of the material

The surface temperature profile is computed based on the beam spot size (waist) given as 0.9 mm and by equation (4.23), $U(a, t) = 300$ K and $U(r, 0) = 300$ K and equation (4.25), $\frac{\partial U}{\partial r} = 0$, at $r = a$ for heating of the industrial diamond.

Let the 1st boundary condition to be this $U(a, t) = 300$ K and $U(r, 0) = 300$ K and

2nd boundary condition to be this $\frac{\partial U}{\partial r} = 0$, at $r = a$.

The graph in figure 4.7 is the comparison of the two boundary conditions for the surface temperature of the industrial diamond. The temperature on the 1st and 2nd boundary conditions rises in the microsecond scale and stabilise in 0.0001 s. The maximum temperature on the 1st boundary condition is approximately 3200 K and on the 2nd boundary condition is approximately 20000 K. It is understandable for the temperature of the 2nd boundary condition

to rises very fast and reach very high temperature since the 2nd boundary condition state that there is no heat flow out of the material. Figure 4.8 is surface temperature across the sample for the two boundary conditions of the industrial diamond. This graph shows that the temperature rise in the sample is very fast and falls off towards the edges of the sample.

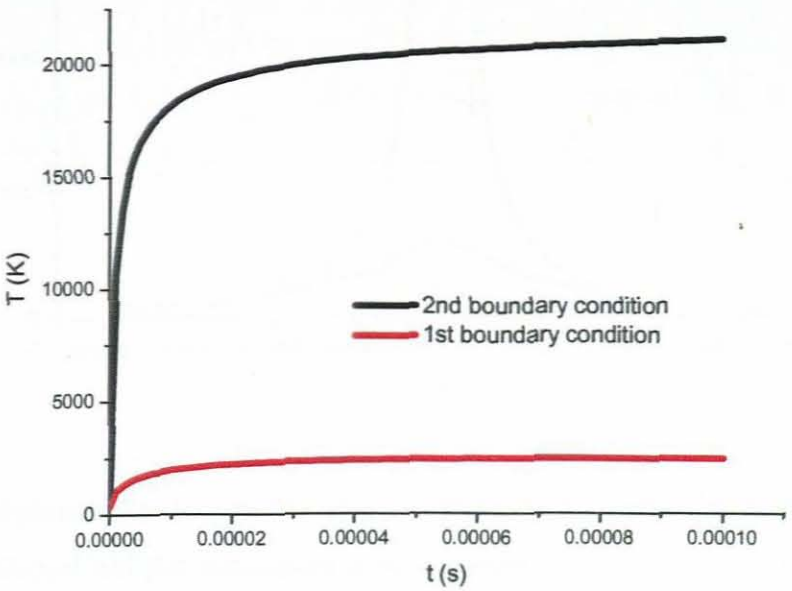

Figure 4.7: Comparison of the two boundary conditions for industrial diamond and the parameters were assumed: P_0 = 30 W, ω_0 = 0.9 x 10^{-3} m, 1st boundary condition (Equation 4.23) and 2nd boundary condition (Equation 4.25). We plotted maximum/peak temperature when r is zero.

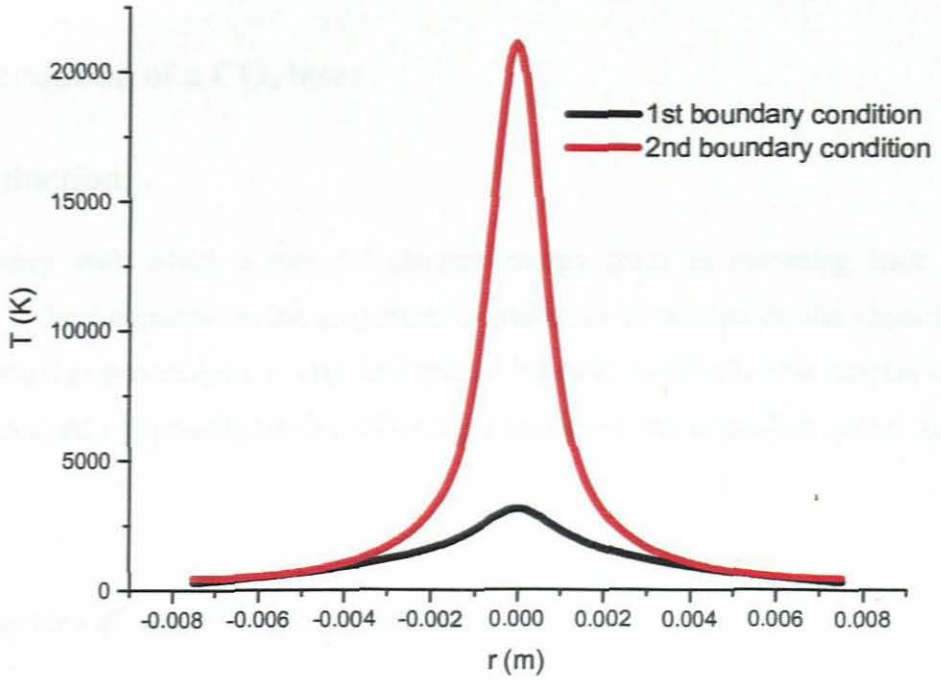

Figure 4.8: Comparison of the two boundary conditions for industrial diamond across the surface of the material and the parameters were assumed: P_0 = 30 W, t = 100 μs, ω_0 = 0.9 x 10^{-3} m.

4.5 Conclusions

An analytical model based on diffusion equation is successfully developed to analyse the temperature distribution in materials irradiated by a CO_2 laser. A parametric study shows the significant effect of parameters such as laser beam sizes. The maximum surface temperature increases as the beam size decreases. The temperature rises in the sample is very fast and falls off towards the edges of the sample. Both these observations have been confirmed experimentally in chapter 6.

Chapter 5

Characterisation of a CO_2 laser

5.1 Introduction

The efficiency with which a material absorbs energy from an incoming laser beam and converts it to heat depends on the properties of materials as well as on the characteristics of the beam, such as wavelength, energy and spatial intensity profile. In this chapter a CO_2 laser was characterized by quantifying the following parameters: beam quality, power and focused beam size.

5.2 Properties of near-Gaussian beams

A laser beam has a Gaussian intensity profile in transverse electromagnetic (TEM_{00}) mode given by [43]

$$I(x,y,z) = I_0(z)\exp\left(-2\frac{(x+y)^2}{\omega(z)^2}\right) \tag{5.1}$$

where $I_0(z)$ is the intensity on the beam axis at any location, z and is given as

$$I_0 = \frac{2P}{\pi\omega(z)^2}. \tag{5.2}$$

where P is the total power in the beam. The beam size $\omega(z)$ can be expressed in terms of the waist ω_0, the waist position z_0, and the wavelength λ:

$$\omega(z) = \omega_0\sqrt{1+\left(\frac{z-z_0}{z_R}\right)^2}. \tag{5.3}$$

The z_R is referred to as the Rayleigh range (equation (5.4)) and is considered the depth of focus for a Gaussian beam

$$z_R = \frac{\pi\omega_0^2}{M^2\lambda}. \tag{5.4}$$

The TEM_{00} mode is often the desired mode because it propagates with the least beam divergence and can be focused to the tightest spot (by propagating a beam through a focus optic) as shown in figure 5.1. Gaussian beams have a waist ω_0 that usually occurs somewhere after the focused mirror. The beam then gradually expands from that location. Then the expanding beam has a curved wave-front with radius of curvature $R(z)$ given as

$$R(z) = (z - z_0)\left[1 + \left(\frac{z_R}{z - z_0}\right)^2\right]. \tag{5.5}$$

The beam angular spread θ in radians at distances well beyond the focused mirror can be given as

$$\theta_0 = \frac{M^2\lambda}{\pi\omega_0}. \tag{5.6}$$

The output from real-life lasers is not truly Gaussian. Then to accommodate this variance, a quality factor M^2 has been defined to describe the deviation of the laser beam from a theoretical Gaussian. For a theoretical Gaussian $M^2 = 1$ and for a real laser beam $M^2 > 1$ [44].

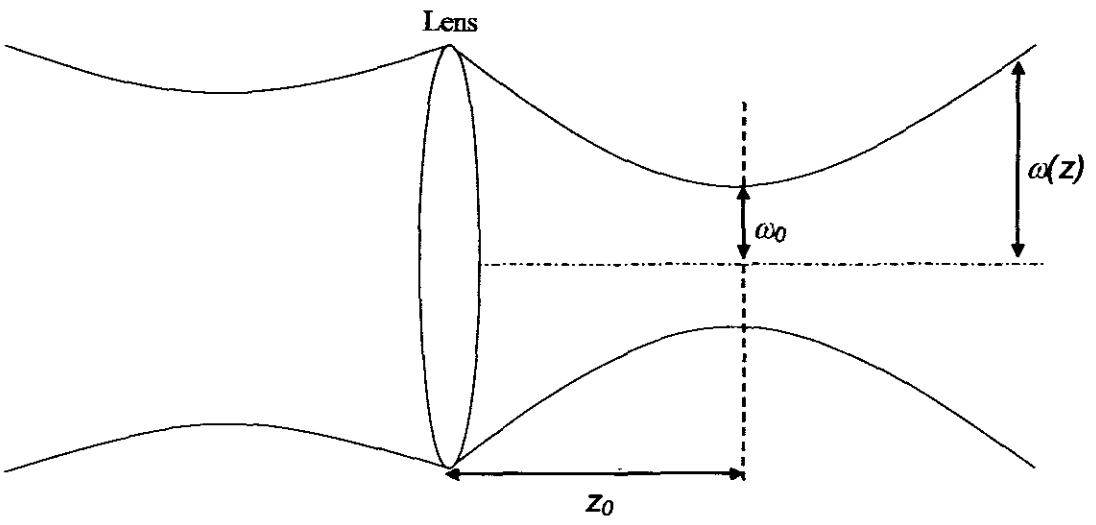

Figure 5.1: A schematic diagram showing some of the parameters of a Gaussian laser beam (TEM_{00} mode).

Therefore the necessary beam parameters are the waist ω_0, the position of the waist z_0 and beam quality M^2. These beam parameters can be determined experimentally by recording beam profiles at several axial positions along z, calculating values for the beam width $\omega(z)$ and then least-squares fitting to obtain ω_0, z_0 and M^2. If the waist ω_0 and the beam quality M^2 are known, the beam width $\omega(z)$ at any distance z from where the waist occurs can be determined from equation (5.3) and also Rayleigh range, radius of curvature.

5.3 Experimental set-up

A continuous wave (cw) CO_2 laser (Edinburgh instrument, model PL6) was characterised in this study. A Helium Neon laser was aligned co-linear with the CO_2 beam for easier alignment through the optical system and experimental set-up is given figure 5.2. The two lasers were then combined using a beam combiner close to the aperture of the CO_2 laser. The flat mirror reflected the laser beam to a pop-up mirror in the optical set up which allowed the laser beam to be directed to a diagnostics table for power measurements (Coherent power meter, model 201) and for determining the lasing wavelength using a spectrum analyser (Optical Engineering Inc, model 16A). A polarisation based attenuator was used to allow power variability (this can also be achieved through adjustment of the laser discharge current).

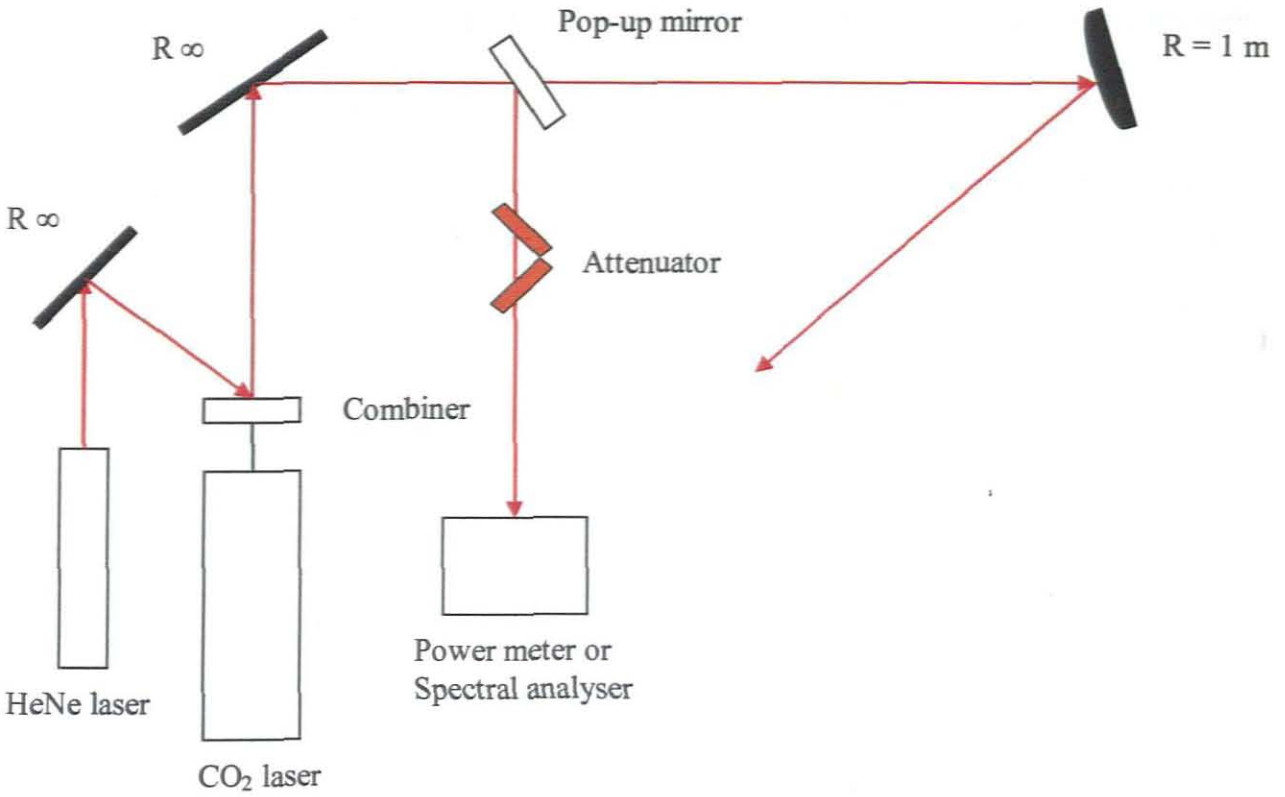

Figure 5.2: A schematic of the laser beam delivery for characterisation.

5.3.1 Beam quality and size

The laser beam was focused using a 1 m radius of curvature concave mirror (gold coated from II–VI Inc.) and the intensity profile of the laser beam was measured. The laser beam profile was measured at various distances from the focus mirror using the scanning slit method. The width of the slit (0.1 mm) was chosen so as to be small enough to allow for good spatial resolution. The beam radius at each z position was determined by fitting a Gaussian function to the slit transmission data. A non-linear least squares fit was used to extract the necessary laser beam parameters, such as waist (ω_0), waist position (z_o) and laser beam quality (M^2). This analysis is presented in a later section.

5.3.2 Laser power versus wavelength and power losses

As mentioned in chapter 3 the tuneability of the laser is possible by means of a grating in the CO_2 laser cavity. By changing the grating orientation, a counter with a number system from 0000 to 9999 enables accurate calibration of this orientation into wavelength. The wavelength

was measured at each counter number system by using the CO_2 laser spectrum analyser and the power at each wavelength was measured. This was needed for choosing the wavelength with the highest power from the laser.

There are many ways to vary the power of the PL6 CO_2 laser, such as varying the current of the laser, varying the angle of an attenuator and by changing the grating orientation. A power meter was placed at different points (P0 and P1) in order to assess the power losses throughout the system (see figure 5.3). The laser current was varied in order to change the output power of the laser and the power was recorded at each point of laser current.

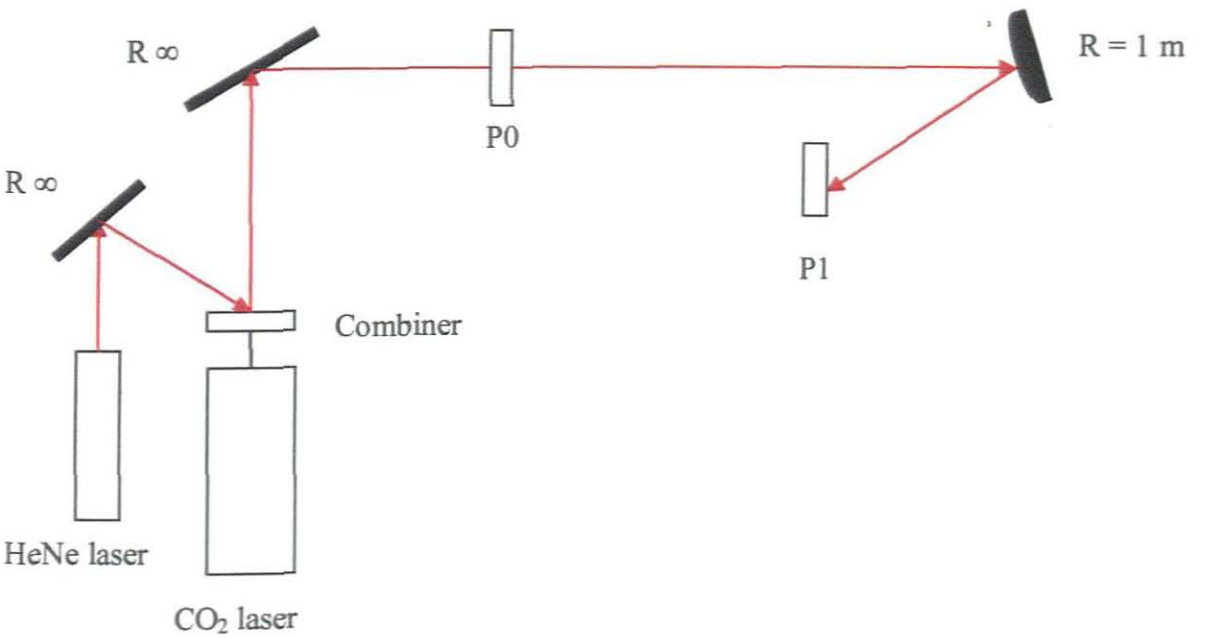

Figure 5.3: A schematic of the laser beam delivery for losses throughout the system.

5.3.4 Polarization

A home-made attenuator consisting of two ZnSe windows mounted at the Brewster angle has a schematic diagram shown in figure 5.4. The home-made attenuator can be rotated in the plane perpendicular to the direction of the beam. By rotating the windows and measuring the transmitted power as a function of the rotational angle, the polarization of the laser beam can be determined.

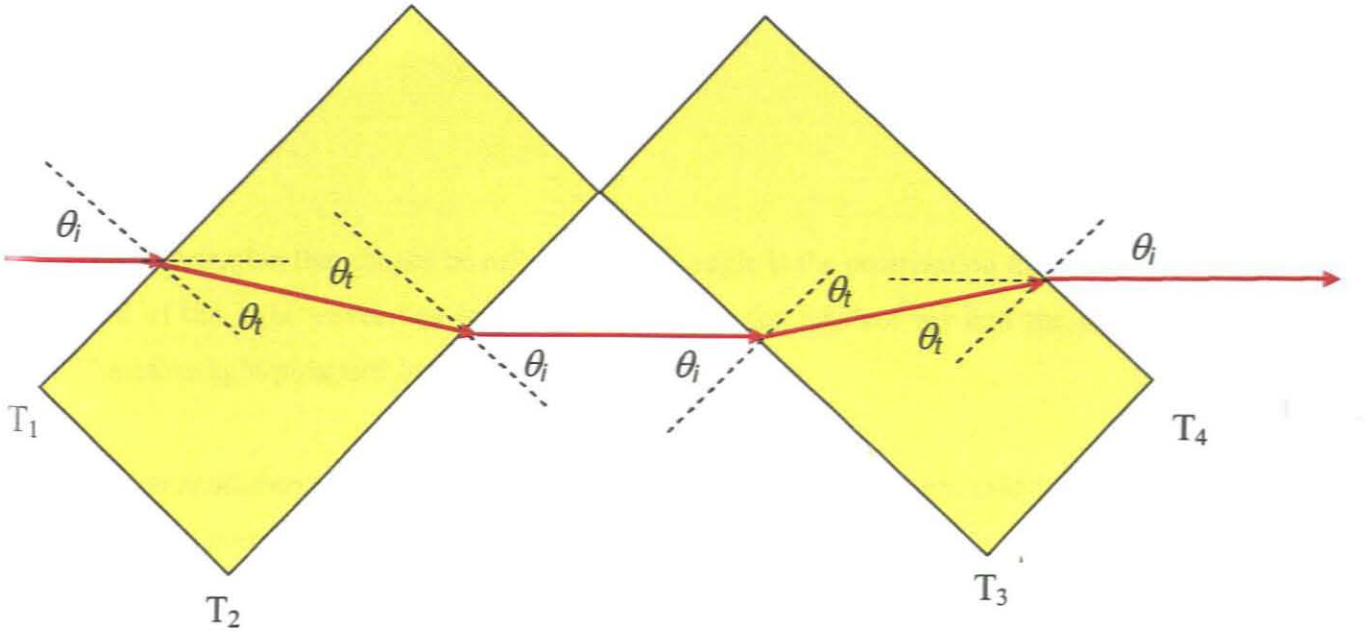

Figure 5.4: A sketch of home made attenuator, which is made of two ZnSe windows mounted at Brewster's angle. The diagram shows a ray traced through the system.

Consider figure 5.4 and assume that a beam of vertical polarized light is incident upon a ZnSe window of refractive index n_1 at an angle of incidence θ_i and transmitted at the angle of refraction θ_t within the ZnSe window interfaces T_1, T_2, T_3 and T_4 respectively. At one particular angle of incidence, however, light with one particular polarization cannot be reflected and the angle of incidence is the Brewster's angle, θ_B, and is derived as follows [45]

$$\theta_i + \theta_t = \frac{\pi}{2}, \tag{5.7}$$

where θ_i is the angle of incidence and θ_t is the angle of refraction. Using Snell's law

$$n_1 Sin\theta_1 = n_2 Sin\theta_2, \tag{5.8}$$

We can calculate the incidence angle $\theta_i = \theta_B$ at which no light is reflected:

$$n_1 Sin\theta_B = n_2 Sin\left(\frac{\pi}{2} - \theta_B\right) \tag{5.9}$$

$$= n_2 Cos\theta_B . \tag{5.10}$$

Rearranging we get this

$$\theta_B = Tan^{-1}\left(\frac{n_2}{n_1}\right). \tag{5.11}$$

The polarization that cannot be reflected at this angle is the polarization for which the electric field of the light waves lies in the same plane as the incident ray and the surface normal. Therefore light polarised in this plane is fully transmitted.

The transmittance of the ZnSe windows set at the Brewster angle was calculated using Fresnel equations and compared with the experimental data. The Fresnel equations describe the behaviour of light when moving between media of different refractive indices. Using the Fresnel equations for reflection and refraction at an interface, it may be shown that the intensity reflection coefficients $R_{//}$ and $R_{\perp}$ of the windows for light polarized parallel and perpendicular to the plane of incidence respectively are given by [46]

$$R_{\perp} = \left[\frac{Sin(\theta_t - \theta_i)}{Sin(\theta_t + \theta_i)}\right]^2 \tag{5.12}$$

$$R_{//} = \left[\frac{Tan(\theta_t - \theta_i)}{Tan(\theta_t + \theta_i)}\right]^2 \tag{5.13}$$

where θ_t and θ_i are the angles of refraction and incidence, respectively. The relationship between reflectance and transmittance assuming no absorption is given by

$$R + T = 1. \tag{5.14}$$

Then transmittances for parallel and perpendicular light are given by

$$T_{//} = 1 - R_{//}, \tag{5.15}$$

$$T_{\perp} = 1 - R_{\perp}. \tag{5.16}$$

The angle of incidence is equal to the angle of transmission for interfaces T_2 and T_4 because the normal lines are parallel to each other. Since the ZnSe windows are set at the Brewster angle, so the angle of incident is given as

$$\theta_i = Tan^{-1}\left[\frac{n_2}{n_1}\right] \tag{5.17}$$

n_1 is 1 and n_2 is 2.403 in equation (5.17). See equation (5.7) and therefore θ_t is given by

$$\theta_t = \frac{\pi}{2} - \theta_i. \tag{5.18}$$

We calculated transmittance from T_1 interface through T_4 interface for parallel and perpendicular polarization. The total transmittance of the system was calculated by multiplying the transmittance T_1 interface to T_4 interface for parallel and perpendicular polarization:

$$T_{II}^{total} = T_{1II}T_{2II}T_{3II}T_{4II}, \tag{5.19}$$

$$T_{\perp}^{total} = T_{1\perp}T_{2\perp}T_{3\perp}T_{4\perp}. \tag{5.20}$$

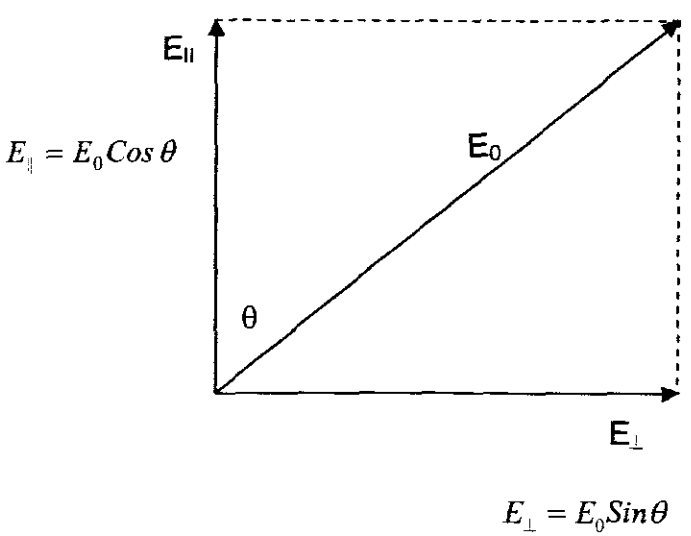

Figure 5.5: A schematic diagram of polarization light at angle.

Consider a light beam in the z direction incident on a polarizer, which has its transmission axis in the y direction. On the average, half of the incident light has its polarization axis in the y direction and half in the x direction. Then half the intensity is transmitted and the transmitted light is linearly polarised in the y direction. Assume we have a second polarizer

whose transmission axis makes an angle θ with that of the first polarizer (figure 5.5). The $\boldsymbol{E}$ vector of the light between the polarizers can be resolved into two components, one parallel and one perpendicular to the transmission axis of the second polarizer. If we call the direction of transmission of the second polariser $\boldsymbol{E}_{II}$ and $\boldsymbol{E}_{\perp}$ the their equations can be written as

$$E_{II} = E_0 Cos\theta, \tag{5.21}$$

$$E_{\perp} = E_0 Sin\theta. \tag{5.22}$$

Only the component E_{II} is transmitted by the second polariser. The intensity is proportional to the square of the amplitude. Then the intensity transmitted by both polarizers can be expressed as

$$I_{II} = E_{II}^2 = E_0^2 Cos^2\theta, \tag{5.23}$$

$$I_{\perp} = E_{\perp}^2 = E_0^2 Sin^2\theta. \tag{5.24}$$

Therefore the total intensity for parallel and perpendicular polarization is given by

$$I_{II} = T_{totalII} \times (E_0 Cos\theta)^2, \tag{5.25}$$

$$I_{\perp} = T_{total\perp} \times (E_0 Sin\theta)^2. \tag{5.26}$$

Then to get the total transmittance intensity of the Brewster windows we added the total intensity of parallel and perpendicular polarization (equation (5.25) and (5.26)):

$$I = I_{II} + I_{\perp}. \tag{5.27}$$

5.4 Results and discussion

Figure 5.6 shows an experimental data of the power spectrum. This power spectrum shows the well-known four distinct emission bands from the CO_2 laser in the wavelength range 9.2 to 10.8 μm. The major bands correspond to the rotational (R) and vibrational (P) modes of the CO_2 molecule. 9 P and 10 P are the strongest bands while 9 R and 10 R are lowest bands.

10*P*20 line has the most power and is at roughly 10.6 μm. All the results that follow below were set to the 10*P*20 line band (10.6 μm) since it has most power.

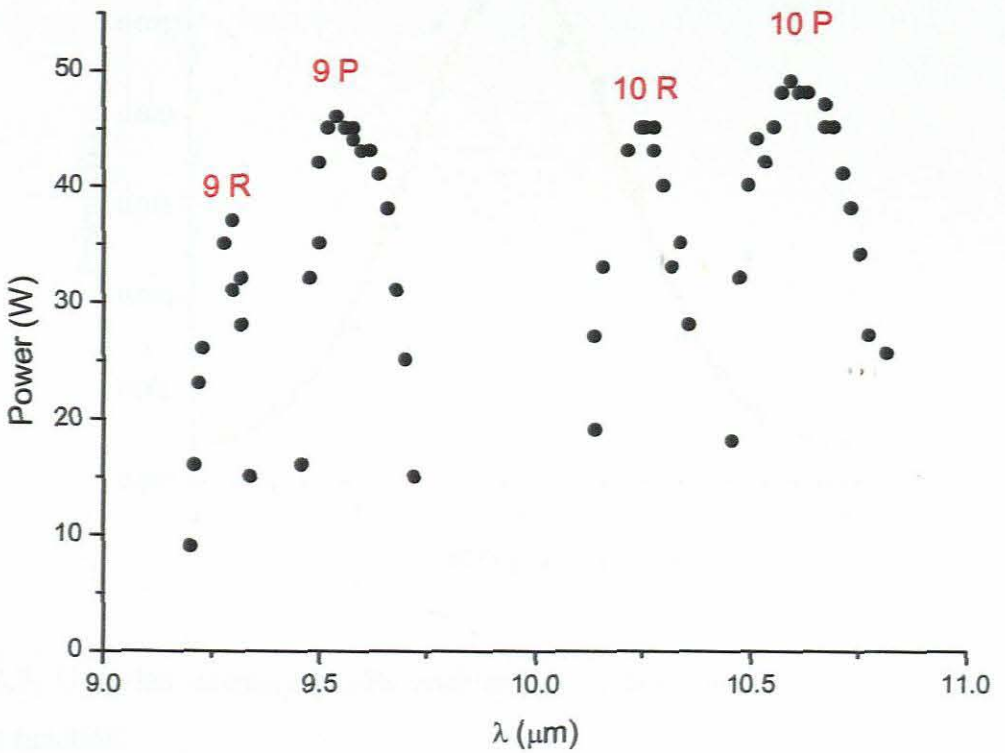

Figure 5.6: Experimental data of the power spectrum of the CO_2 laser, showing the well-known four distinct emission bands. The 10*P*20 line showed the highest output power of roughly 45 Watts.

The laser beam was focussed as discussed in section 5.2.1 and the resulting propagation was measured. The graphs in figure 5.7 show experimental data and fitted Gaussian as a function of slit position. The beam size was determined by fitting a Gaussian function to the experimental data.

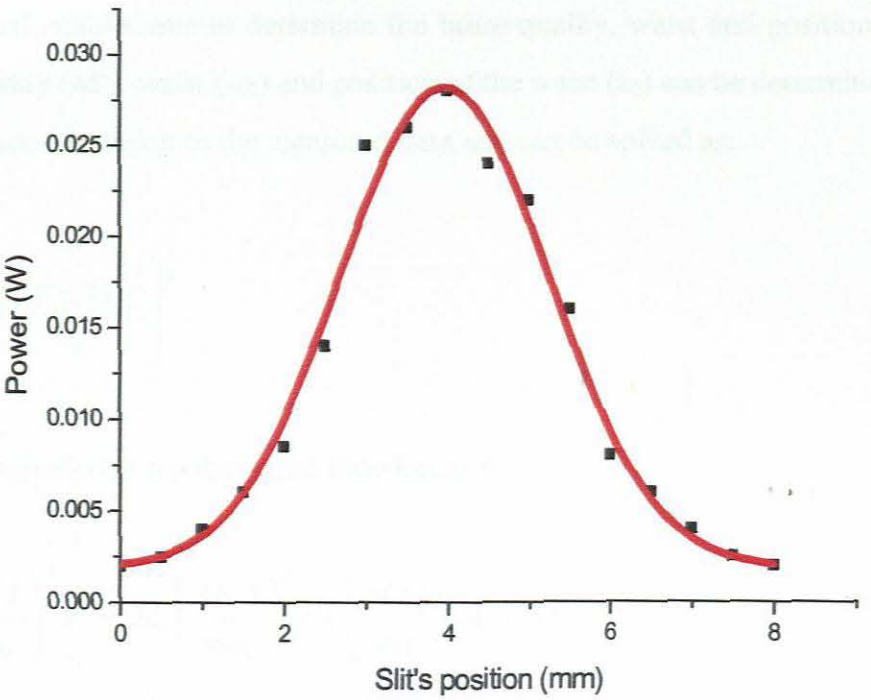

Figure 5.7: Gaussian intensity profile enables one to determine the beam size by fitting a Gaussian function.

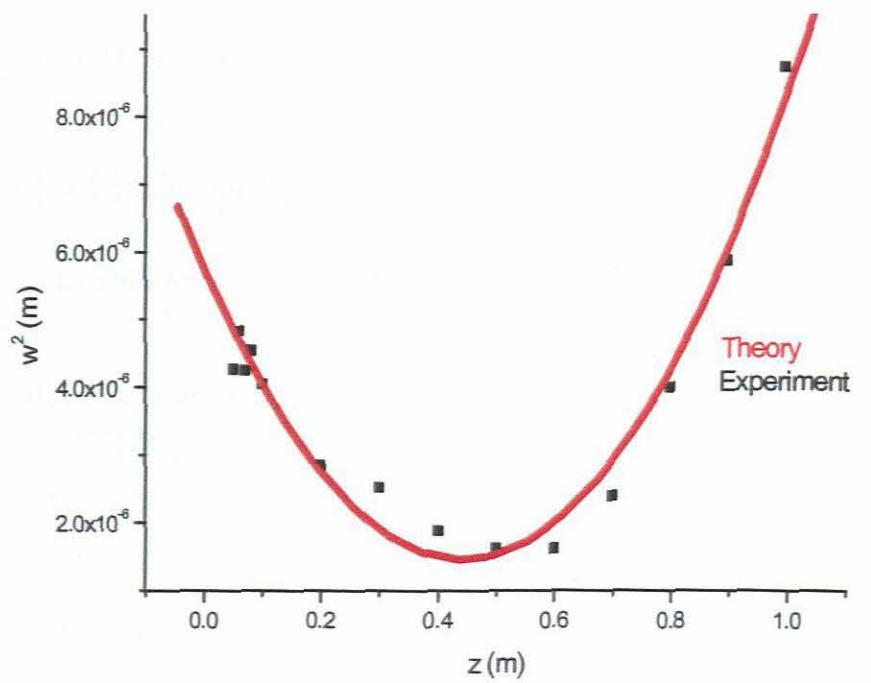

Figure 5.8: Experimental and theoretical data of the laser beam as it propagates enables one to determine the beam quality, waist and position of the waist. This is needed for predicting the beam size throughout the experiment.

The graph in figure 5.8 shows experimental and theoretical data of the laser beam as it propagates, and enables one to determine the beam quality, waist and position of the waist. The beam quality (M^2), waist (ω_0) and position of the waist (z_0) can be determined by fitting a beam propagation equation to the measured data and can be solved as:

$$\omega(z) = \omega_0 \left[1 + \left(\frac{z - z_0}{z_R} \right)^2 \right]^{\frac{1}{2}}. \tag{5.26}$$

This can be expanded to a polynomial function in z:

$$\omega^2(z) = \left(\frac{M^2 \lambda}{\pi \omega_0} \right)^2 z^2 - 2 z_0 \left(\frac{M^2 \lambda}{\pi \omega_0} \right)^2 z + \left(\frac{M^2 \lambda}{\pi \omega_0} \right)^2 z_0^2 + \omega_0^2. \tag{5.27}$$

$$\omega^2(z) = 2.18409 \times 10^{-5} z^2 - 1.93796 \times 10^{-5} z + 5.75502 \times 10^{-6}. \tag{5.28}$$

The solution is:

$$\left(\frac{M^2 \lambda}{\pi \omega_0} \right)^2 = 2.18409 \times 10^{-5}. \tag{5.29}$$

$$-2 z_0 \left(\frac{M^2 \lambda}{\pi \omega_0} \right)^2 = -1.93796 \times 10^{-5}. \tag{5.30}$$

$$\left(\frac{M^2 \lambda}{\pi \omega_0} \right)^2 z_0^2 + \omega_0^2 = 5.75502 \times 10^{-6}. \tag{5.31}$$

Results are given in table 5.1:

Table 5.1: Propagation parameters

ω_0(m)	Z_0(m)	M^2	λ(μm)
0.001207	0.4436	1.68	10.6

The laser beam was found to be near Gaussian in intensity profile (M^2 = 1.68) and focused to a waist radius of 0.001207 m.

Results for laser power optimization via laser current of a CO_2 laser power supply are shown in figure 5.9. A CO_2 laser has two arms of its U-shaped resonator. Current meter 1 controls

the electrical current in one arm and current meter 2 controls electrical current in the other arm. One of the laser current meters was fixed at 26 A while the other meter 1 was varied to yield corresponding power reading. Current and output power data were obtained.

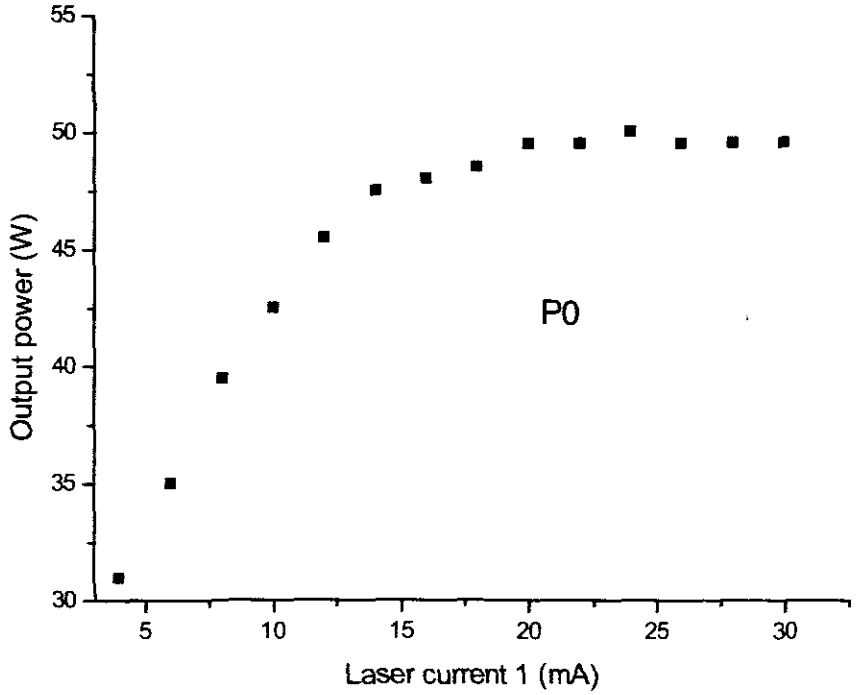

Figure 5.9: Laser current's effect on the power output: P0 signifies the point at the exit of the laser.

The graph in figure 5.10 is the experimental data for the optical power transmission of the CO_2 laser through the home-made attenuator. The power at each angle was measured by varying the angle attenuator as discussed in section 5.2.2. This spectrum shows that the maximum power is at 0°, 180° and 360° and minimum power is at 90° and 270°. The theoretical curves for the parallel and perpendicular polarized light are shown in figure 5.11 and 5.12, respectively and the total optical intensity or power transmission is shown in figure 5.13. The experimental data was fitted to the theoretical curve as shown in figure 5.14 and there is very good agreement between theory and experiment. The minimum transmittance and maximum transmittance were 0.06 and 0.9, respectively. This implies a total intensity: I = 0.06 + 0.9 = 0.96. The fraction that was horizontally polarized was thus: (0.06 / 0.96) x100= 6.25 %. The fraction that was vertically polarized was thus: 100 % - 6.25 % = 93.75 %.

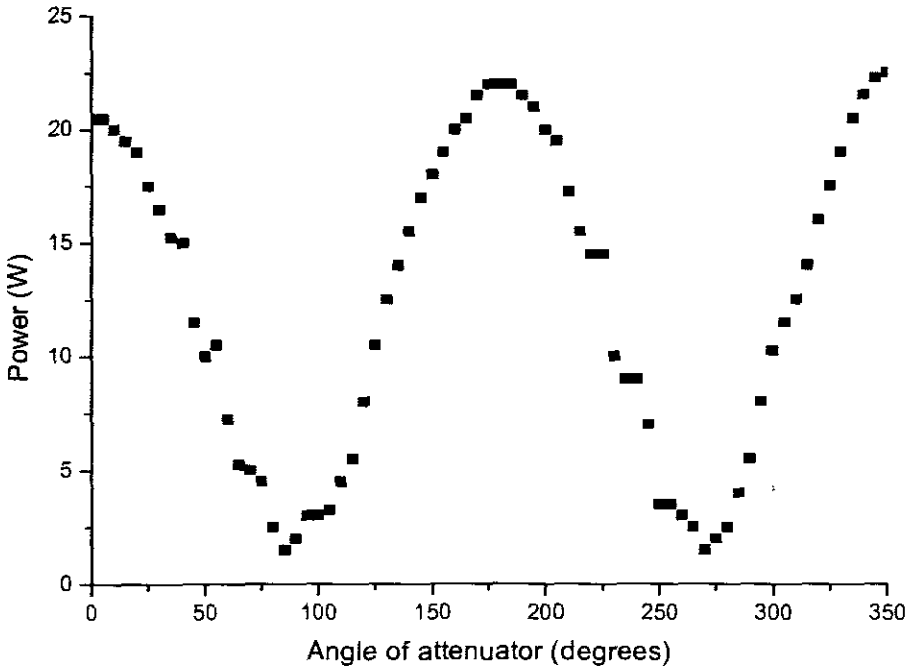

Figure 5.10: Experimental data for the optical power transmission of the CO_2 laser through the home-made attenuator.

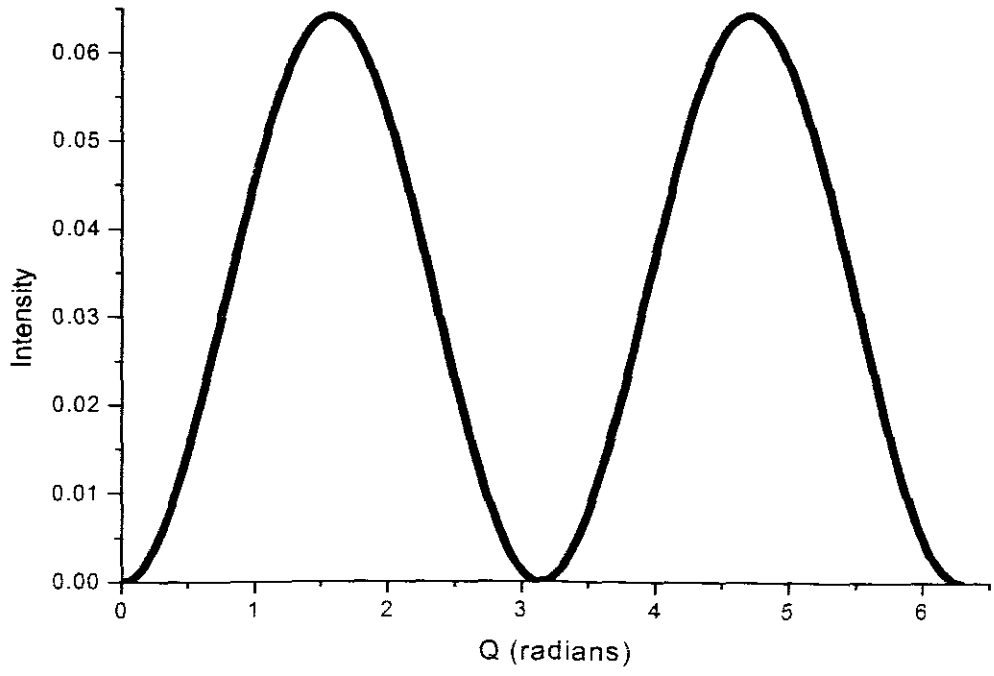

Figure 5.11: Optical intensity transmission of the parallel polarized light through the ZnSe windows (equation (5.25)).

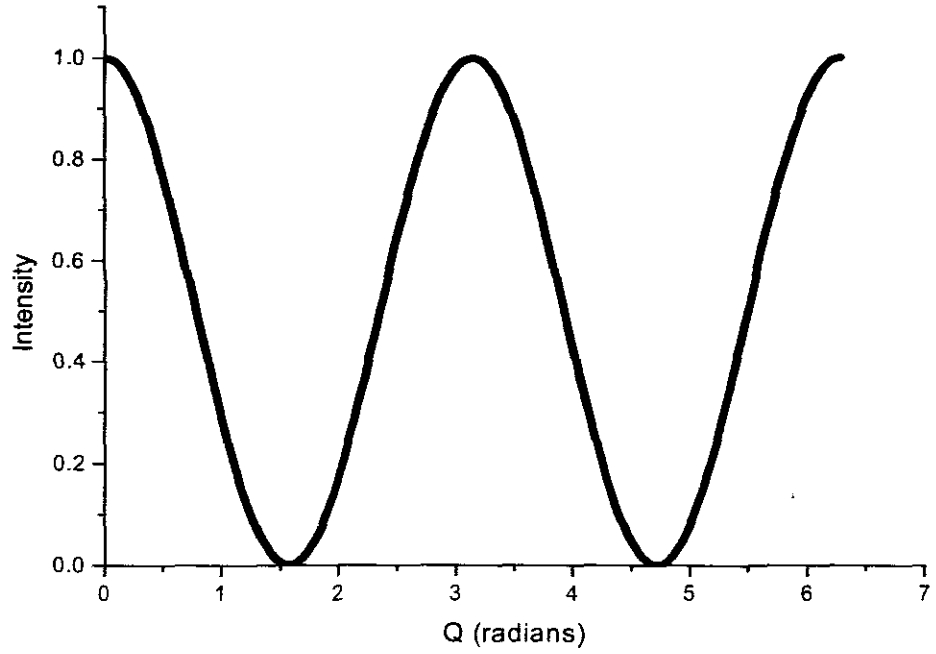

Figure 5.12: Optical intensity transmission of the perpendicular polarized light through the ZnSe windows (equation (5.26)).

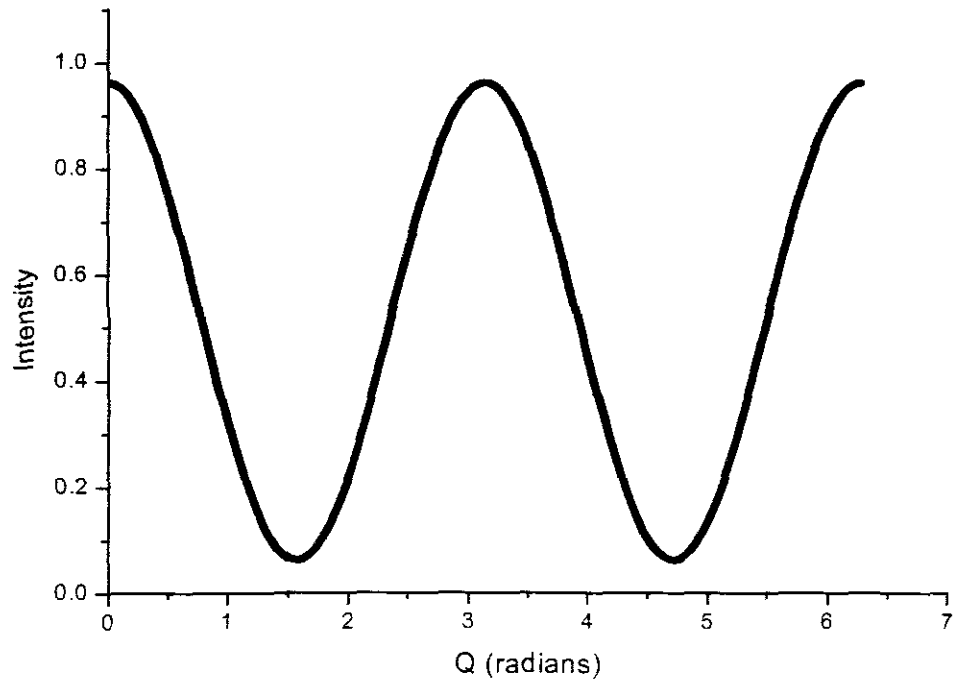

Figure 5.13: Total intensity transmission light through the ZnSe windows (equation (5.27)).

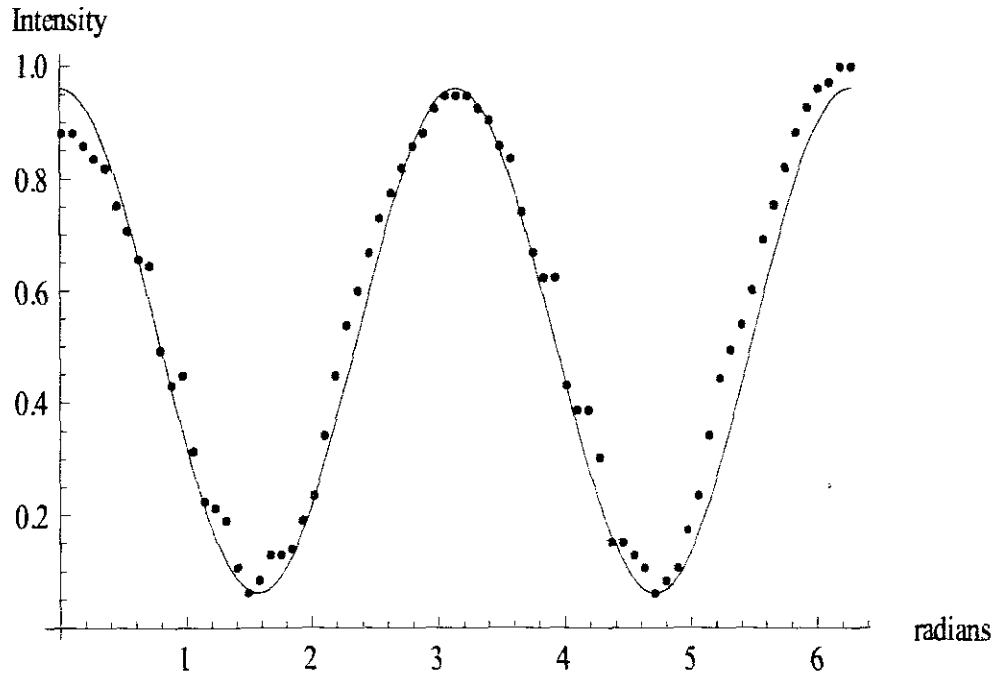

Figure 5.14: Total intensity transmission fitted to the experimental data. This graph shows a good agreement between the model (equation (5.27)) and experimental data.

5.5 Conclusions

The experiments characterising the CO_2 laser were successful. The necessary laser parameters were determined and were given as: Waist of the beam was 0.001207 m, waist position was 0.4436 m and beam quality is 1.68, indications a near-Gaussian intensity profile. The model of optical power/intensity transmission was successful derived and compared with the experimental data. There is good agreement between the theory and experiment. The polarization was determined.

Chapter 6

Laser heating

6.1 Introduction

The CO_2 laser is the heating source used to raise the temperature of the sample. The main purpose of this chapter is to present the laser heating method, temperature measurement method and metal-oxides compounds melting temperature. Laser heating set-up, temperature measurement results and metal-oxide compounds results are also presented in this chapter.

6.2 Laser heating set-up

The experimental system for the delivery of the laser beam for sample heating is shown in Figure 6.1. A continuous wave (cw) CO_2 laser was used in the experiment (Synrad Inc., maximum 30 W). A Helium Neon laser was aligned co-linear with the CO_2 beam for easier alignment through the optical system. A convex mirror was used to expand the beam to a diameter of approximately 1 cm at the optical plane of the ZnSe focusing lens (f = 55 mm), which then focused the beam to allow a variable spot size to be delivered to the sample. The thermal radiation spectrum from the sample was reflected off a ZnSe window onto the objective lens (focal length of 135 mm). A beam splitter then splits the thermal radiation into two, for simultaneous detection on a CCD camera and a spectrometer (Ocean Optics Inc., USB-2000 spectrometer). The CCD camera was used to view the hot-spot on the sample during the heating process. The spectrometer was used to capture the signal of the thermal radiation spectrum and from the spectrum the temperature can be determined.

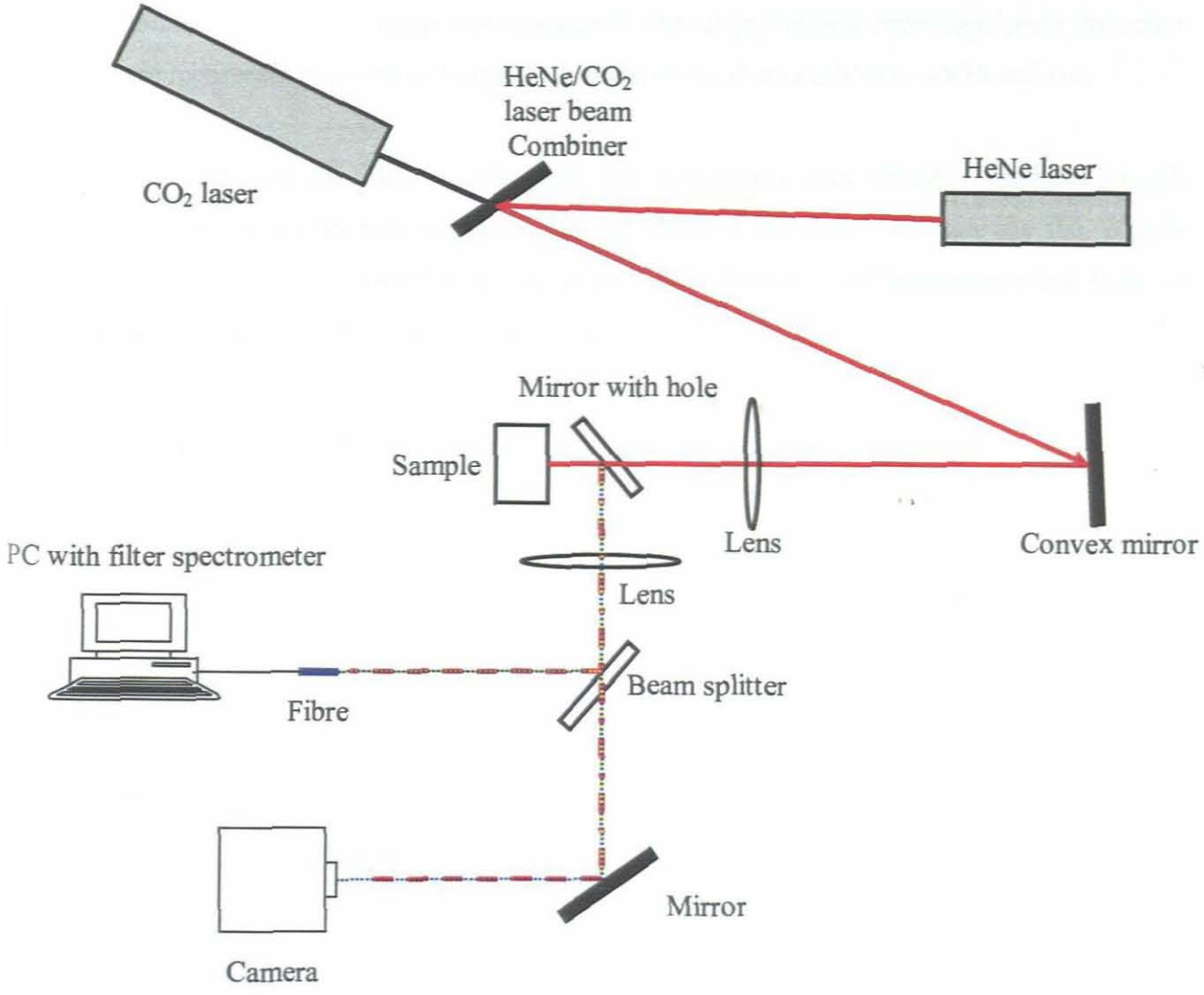

Figure 6.1: A schematic diagram of the laser beam delivery for heating of the sample.

6.3 Calibration of the spectrometer

The emission spectrum of a wideband grey body is often distorted due to the wavelength dependent efficiency of the detector and the deleterious effects of optical elements, e.g. chromatic aberration of lenses. By calibrating the spectrometer using a lamp (LS-1-CAL, Radiometrically Calibrated Miniature Tungsten Halogen Source, 3100 K), a corrected emission spectrum is then obtained.

The calibration of an ocean optics spectrometer for spectral irradiance response was accomplished by using a blackbody of known temperature. In this study, a fibre was placed in front of the lamp to collect the emission as shown in figure 6.2. 30 minutes elapsed after the lamp was switched on to allow it to stabilise. A reference spectrum, dark spectrum and

emission spectrum of the lamp were measured and all processing conditions were the same for three measurements such as integration times, scans average, boxcar width and etc.

Once the emission spectrum was obtained, the temperature was extracted from the Planck blackbody radiation formula (equation (2.25)) fitted to the data. One can use the Wien's approximation to the Planck formula to linearise the data and the temperature can then be easily extracted from the linear fit as follows:

$$\ell n(I\lambda^5) = \ell n(c_1 \varepsilon(\lambda)) - \frac{c_2}{\lambda} U^{-1} \tag{6.1}$$

where I is the spectral intensity, c_1 and c_2 are constants which are given by

$$c_1 = 2\pi hc^2 = 3.7418 \times 10^{-16} W.m^2, \tag{6.2}$$

$$c_2 = \frac{hc}{k_B} = 1.4388 \times 10^{-2} m.K. \tag{6.3}$$

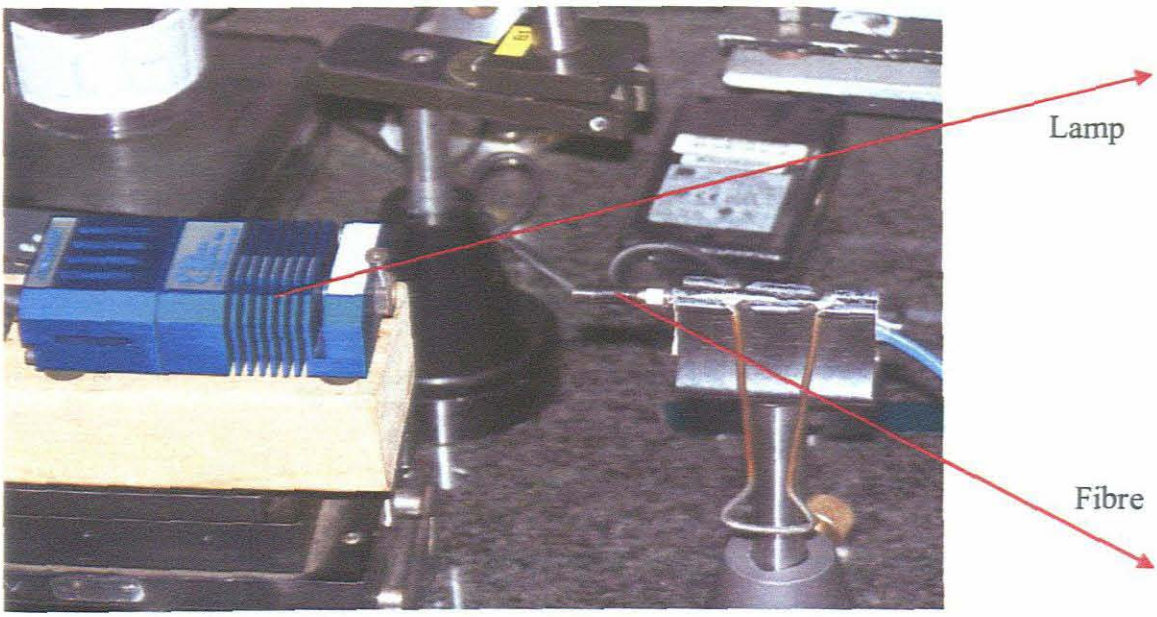

Figure 6.2: An experimental set-up for calibration of the spectrometer.

The spectra in figure 6.3 are the reference and the dark spectrum, respectively. Figure 6.3 (c) is an emission spectrum of the lamp acting as a blackbody of a known temperature (3 100 K).

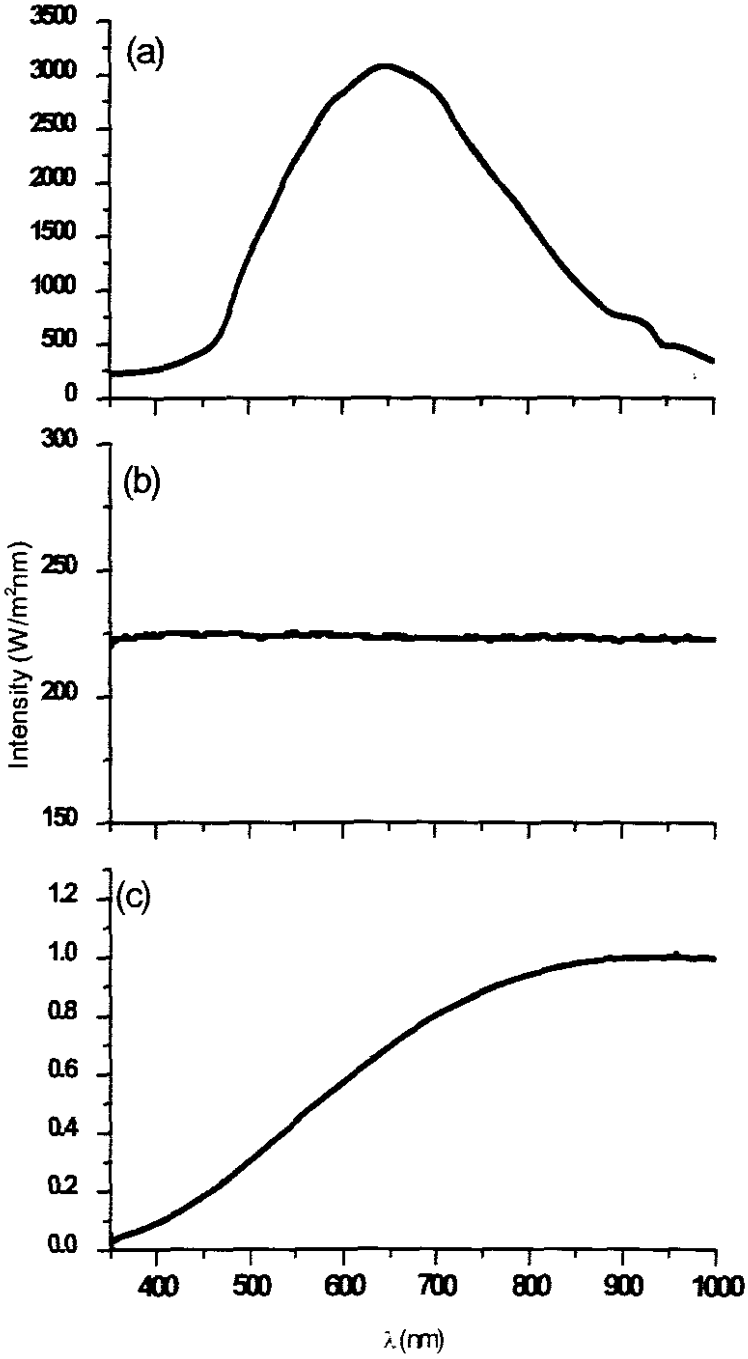

Figure 6.3: (a) Reference spectrum of the Light source with a blackbody of known temperature (3 100 K), (b) Dark spectrum of the Light source with a blackbody of known temperature (3 100 K), and (c) Emission spectrum of the lamp with a blackbody of known temperature (3 100 K).

The temperature can be determined by fitting the Wien approximation (to the Planck formula) in the measured data and can be solved as follows:

$$I = \frac{c_1}{\lambda^5}\left(\exp\frac{c_2\varepsilon(\lambda)}{\lambda U}\right)^{-1} \tag{6.4}$$

This can be expanded to a linear function:

$$\ell n(I\lambda^5) = \ell n(c_1\varepsilon(\lambda)) - \frac{c_2}{\lambda}U^{-1} \tag{6.5}$$

$$y = 39.20307 - 324563.20049x \tag{6.6}$$

The solution to equation (6.5) and (6.6) is:

$$\ell n(I\lambda^5) = y \tag{6.7}$$

$$\ell n(c_1\varepsilon(\lambda)) = 39.20307 \tag{6.8}$$

$$-\frac{c_2}{\lambda}U^{-1} = -324563.20049x \tag{6.9}$$

From the slope of the linear fit (as shown in figure 6.4) the temperature can be determined as follows:

$$-\frac{1}{U} = -324563.20049 \tag{6.10}$$

$$U = \frac{1}{324563.20049\times10^{-9}} = 3081\ \text{K} \tag{6.11}$$

The emission spectrum of the lamp was measured 16 times and the calibration graph was plotted as shown in figure 6.5. The spectrometer was successfully calibrated and the average temperature was found to be 3090 K ± 10 K as the result shown in figure 6.5.

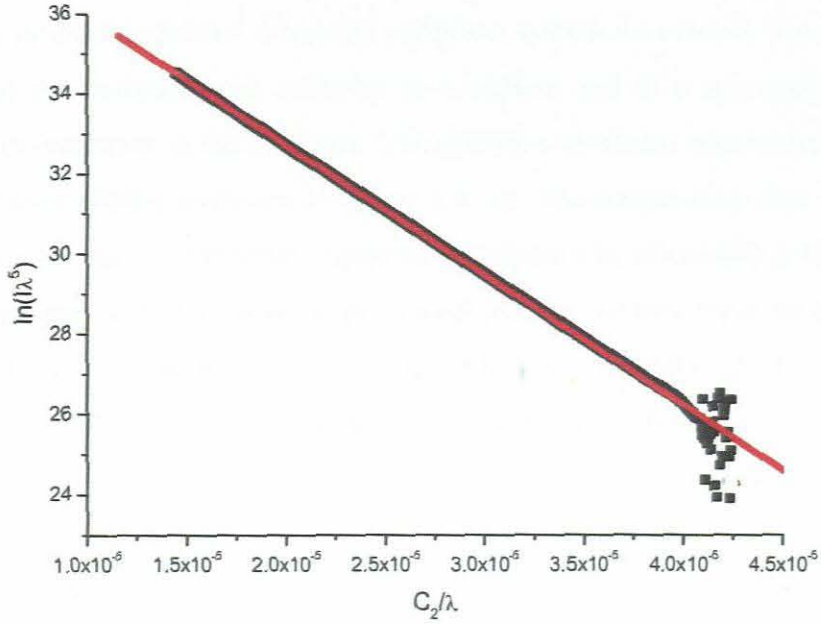

Figure 6.4: The linearised data with Wien approximation to Planck's blackbody formula: from the slope of the graph temperature can be determined. The linear fit equation is given as $y = 39.20307 - 324563.20049x$.

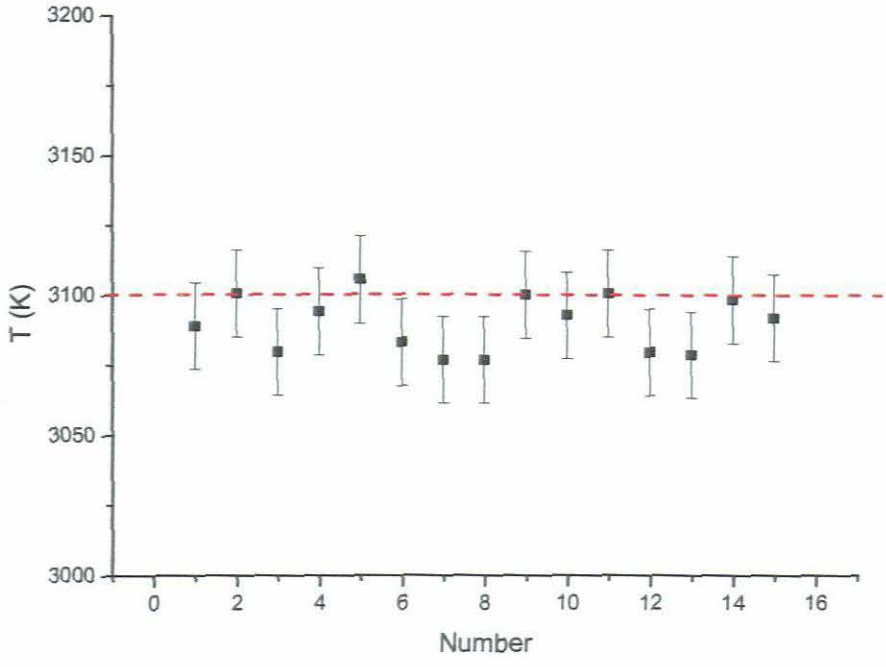

Figure 6.5: The repeatability graph (of the calibration of the spectrometer), the average temperature is 3090 ± 10 K and expected temperature is 3100 K. The measurements were taken over a day.

6.4 Optics

An unexpected problem occurred when the complete system was tested. An alumina sample was heated and the emission was reflected to a camera and to a spectrometer by using a HeNe/CO_2 beam combiner as the reflector. The emission spectrum was recorded but found to contain interference effects as shown in figure 6.6 (a). The temperature that was determined from this (figure 6.6 on (a) spectrum) emission spectrum was unreliable with large error. In this regard, a number of experiments were carried out for the investigation to determine the cause of this effect. These include collecting emission spectrum of all optics using the calibration lamp (LS-1-CAL, Radiometrically Calibrated Miniature Tungsten Halogen Source, 3 100 K).

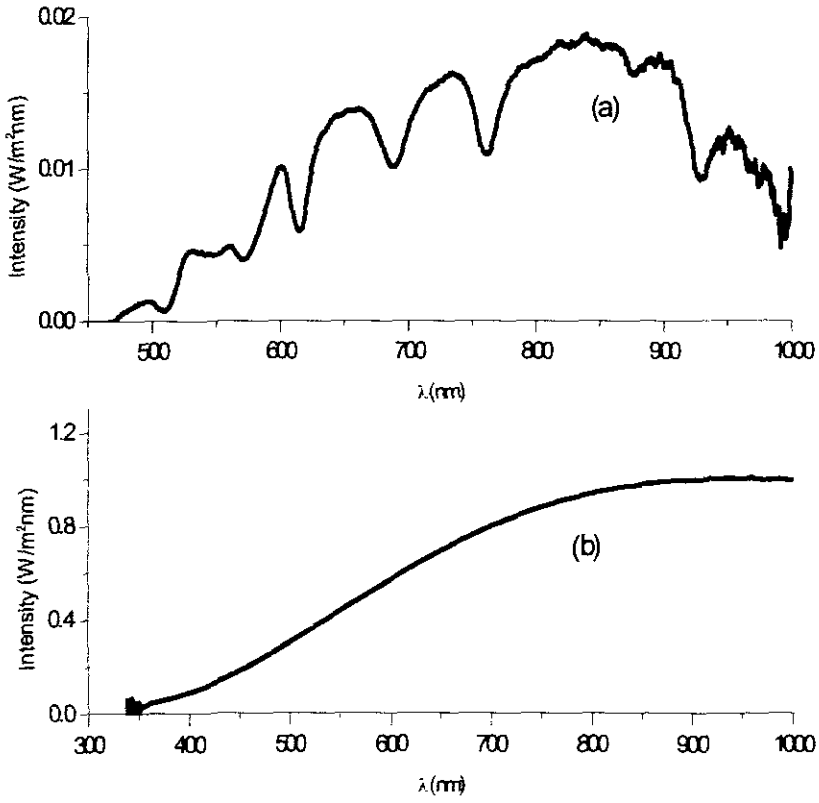

Figure 6.6: Emission spectra showing (a) some interference (unexpected spectrum) (b) no interference (expected spectrum).

The spectra were taken: before the HeNe/CO_2 beam combiner; after the HeNe/CO_2 beam combiner; HeNe/CO_2 beam combiner and projection lens; HeNe/CO_2 beam combiner, projection lens and flat mirror. All the spectra are show in figure 6.7.

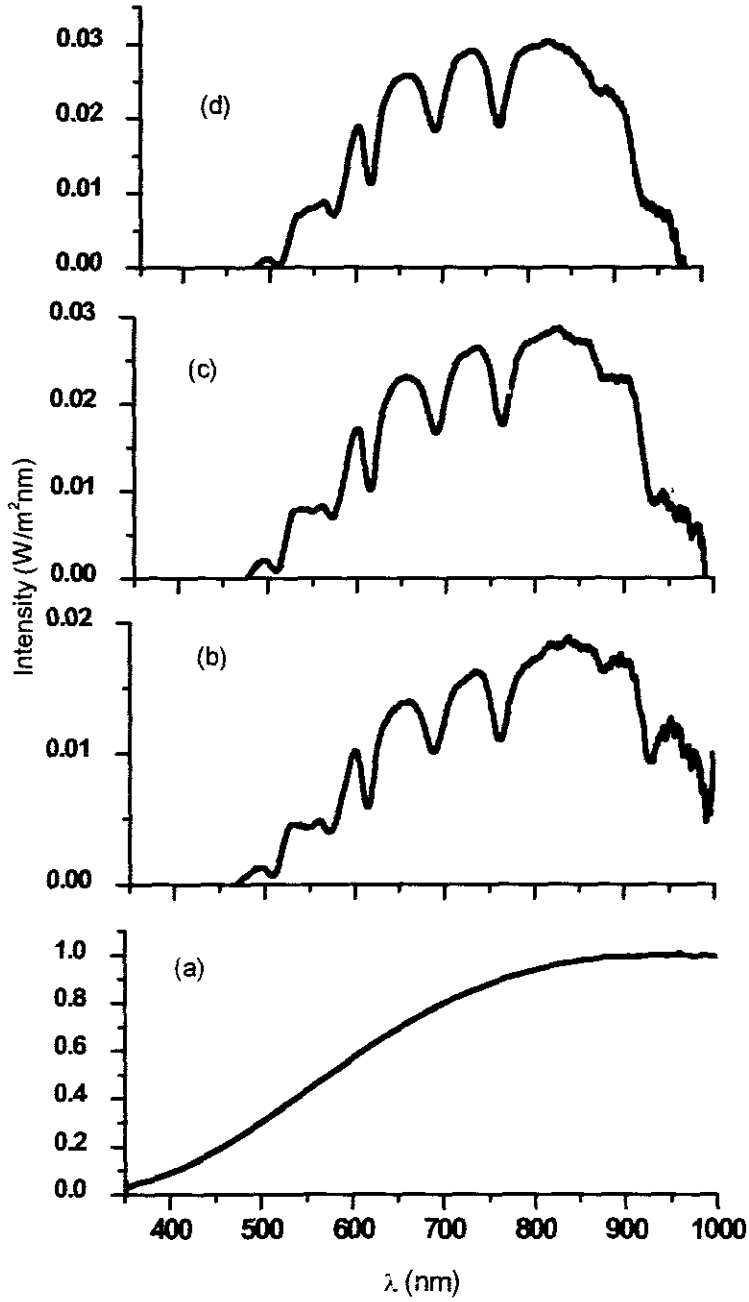

Figure 6.7: Emission spectra of all the optics: (a) Emission spectrum taken after the HeNe/CO_2 beam combiner, (b) Emission spectrum taken before the HeNe/CO_2 beam combiner, (c) Emission spectrum taken after the beam combiner and projection lens, (d) Emission spectrum taken after the beam combiner, projection lens and flat mirror. The interference (from figure 6.7 b) originates from the coating of the HeNe/CO_2 beam combiner.

Emission spectrum taken before the HeNe/CO_2 beam combiner (figure 6.7 (a)) shows no interference. The emission spectrum after the HeNe/CO_2 beam combiner (figure 6.7 (b))

shows interference. The emission spectra in figure 6.7 (c) and figure 6.7 (d) are taken after the HeNe/CO_2 beam combiner, projection lens, flat mirror and also show some interference.

To solve the problem, the data analyses of the emission spectra were carried out by assuming that the input emission spectrum to be S_{in}, optics effect to be X and output emission spectrum to be S_{out} as shown in figure 6.8. Then $S_{in}X = S_{out}$. By doing this one can get the effect of the optic.

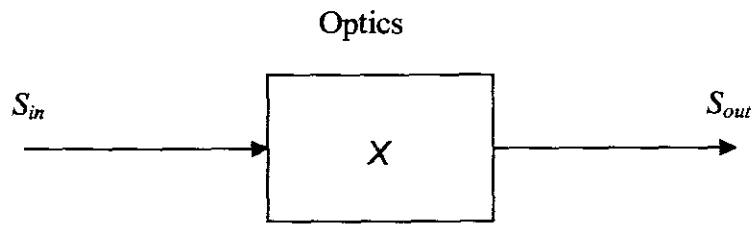

Figure 6.8: A schematic diagram illustrating the emission spectrum in S_{in}, optics effect X and emission spectrum out S_{out}.

The results of this data an analysis is shown in figures 6.9 and 6.10. Figure 6.9 shows the effect of the HeNe/CO_2 beam combiner and it was determined by dividing the data in figure 6.7 (b) with the data in figure 6.7 (a). The spectrum in figure 6.10 is effect of the projection lens that was determined by dividing the data in figure 6.9 (c) with the data in figure 6.9 (a). Then it was concluded that the HeNe/CO_2 beam combiner was producing the interference on the signal (emission spectrum). We summarised that the interference was due to the coating of the beam combiner, which was acting as an etalon.

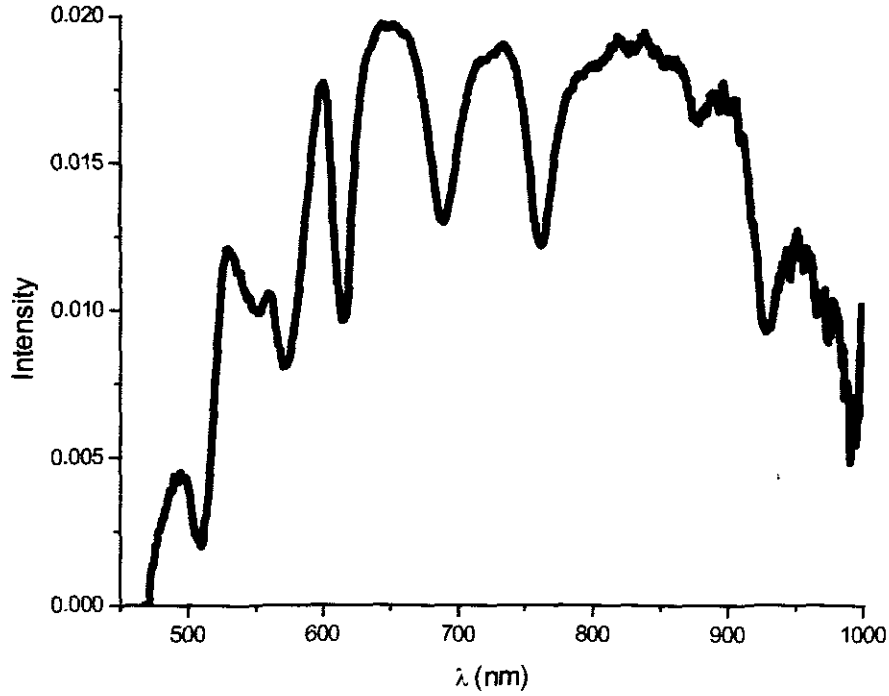

Figure 6.9: The spectrum shown is the effect of the HeNe/CO_2 beam combiner that was determined by dividing the data in figure 6.7 (b) with the data in figure 6.7(a).

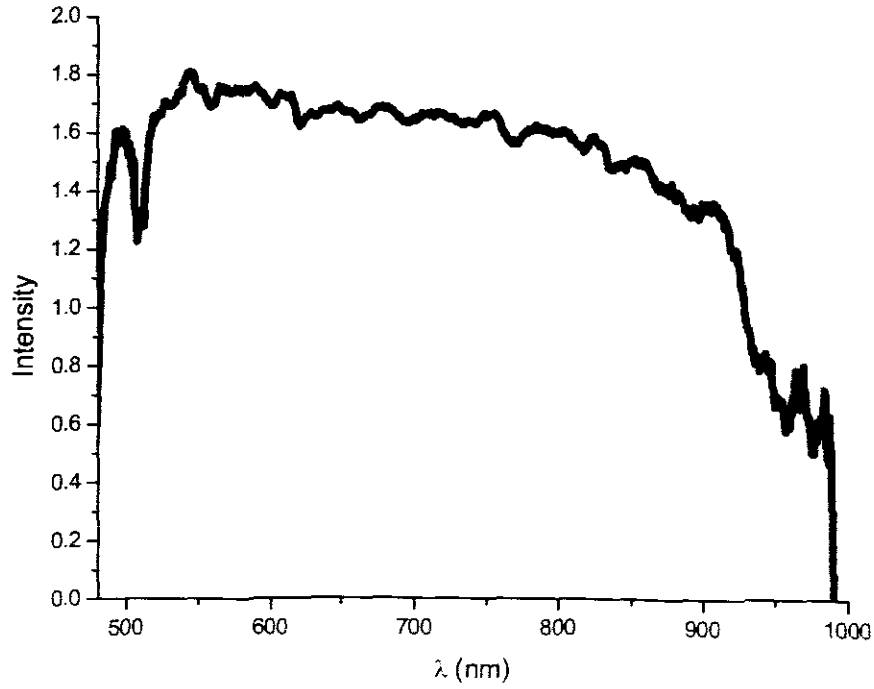

Figure 6.10: This spectrum is the effect of the projection lens that was determined by dividing the data in figure 6.7 (c) with the data in figure 6.7 (a).

The function of the HeNe/CO_2 beam combiner is to transmit the CO_2 laser and reflect the visible light (the emission of the sample), and any solution to the problem would also require these properties. We came up with two possible solutions: A broadband dichroic mirror which is transmitting the 10.6 μm wavelength and reflecting the visible light (emission of the lamp or sample) or by drilling a hole in the flat copper mirror (at an angle or in the centre of the mirror), in order for it to be able to transmit the laser beam and reflect the emission of the sample. Both of the possible solutions (reflectors) are perfect but it was impossible to find a dichroic mirror since most of the companies that make the dichroic mirror are not working in the 10.6 μm range. The second option was taken, that was to drill a hole in the mirror. The hole was made twice the beam size. The beam size was measured (±,3.5 mm) in order to determine the size of the hole as shown in figure 6.11. The diameter of the hole was ± 7 mm and the diameter of the mirror was ± 50 mm.

Collecting a reflected emission spectrum from the calibration lamp tested the flat copper mirror with a hole and the results are shown in Figure 6.12. The emission spectrum shows no interference. This means that our simple solution was working perfectly.

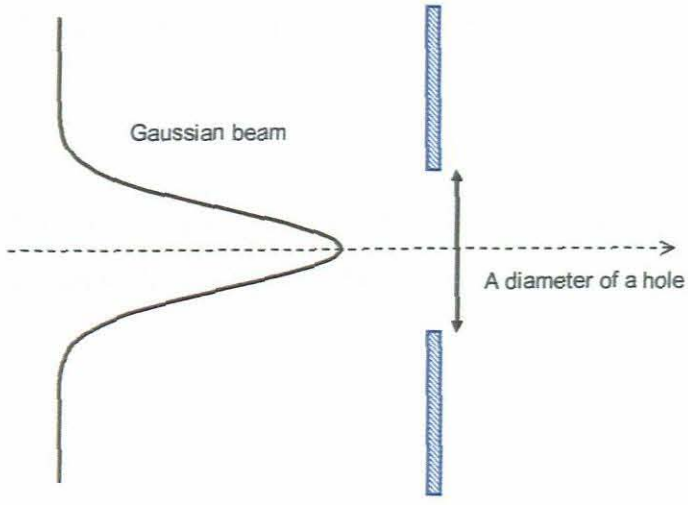

Figure 6.11: A schematic diagram showing a Gaussian beam passing through the hole.

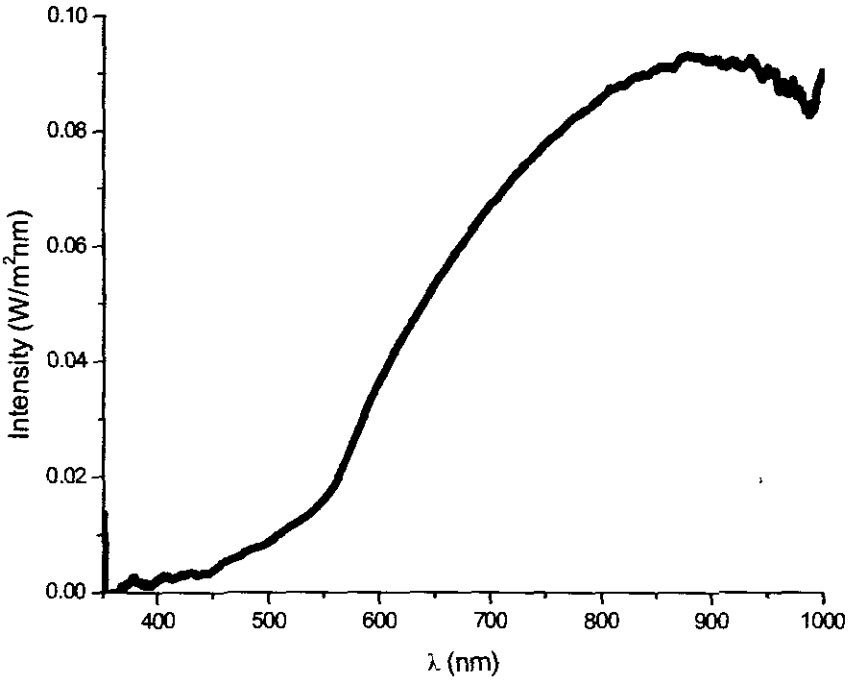

Figure 6.12: Emission spectrum after the mirror with the hole. This spectrum is interference free.

6.5 Testing of metal-oxides compounds

Using the CO_2 laser heated methodology temperature measurements of numerous metal-oxide compounds has been checked for their melting point. The metal-oxide compounds melting temperatures are given in the table 6.1 below. The purpose of this experiment was to determine the accuracy of the temperature measurement.

Table 6.1: Melting points for different metal-oxide compounds [47].

Oxides	Melting point (K)
Al_2O_3	2293
Y_2O_3	2683
SiO_2	1983
La_2O_3	2588
Nd_2O_3	2173
Nb_2O_5	1793
Ho_2O_3	2643
CeO_2	2668
CaO	2843

Table 6.2 shows in detail the results obtained from metal-oxide heating experiments, with the percentage difference between the experimental and expected data. There are five metal-oxides for which the percentage difference is 20% lower, and for the others the percentage difference is higher. A reason for this are still being investigated, but there are a few possibilities: (i) we have assumed that the samples under study behave as black bodies; if this were not true for these samples, then one would expect a discrepancy, (ii) if the samples started melting during the heating, then again the thermal model would break down and discrepancies would be expected. Unfortunately only visual inspection for the onset of melting could be achieved, and thus this cannot be ruled out unless a more sophisticated CCD detector monitoring system is implemented. This is an aspect for future study. There is however good agreement between the experimental and expected data in CeO_2, CaO, La_2O_3 and Y_2O_3. The emission spectra of all the metal-oxides are shown from figure 6.15 to figure 6.23.

Table 6.2: Percentage difference between experimental data and melting point of metal-oxides compounds.

Oxides	Experimental temperature (K)	Measured melting temperature (K)	Difference (%)
Al_2O_3	2695	2293	+18
Y_2O_3	2617	2683	-2
SiO_2	3704	1983	+87
La_2O_3	2424	2588	-6
Nd_2O_3	2705	2173	+24
Nb_2O_5	2413	1793	+35
Ho_2O_3	3421	2643	+29
CeO_2	2661	2668	-
CaO	2665	2843	+6

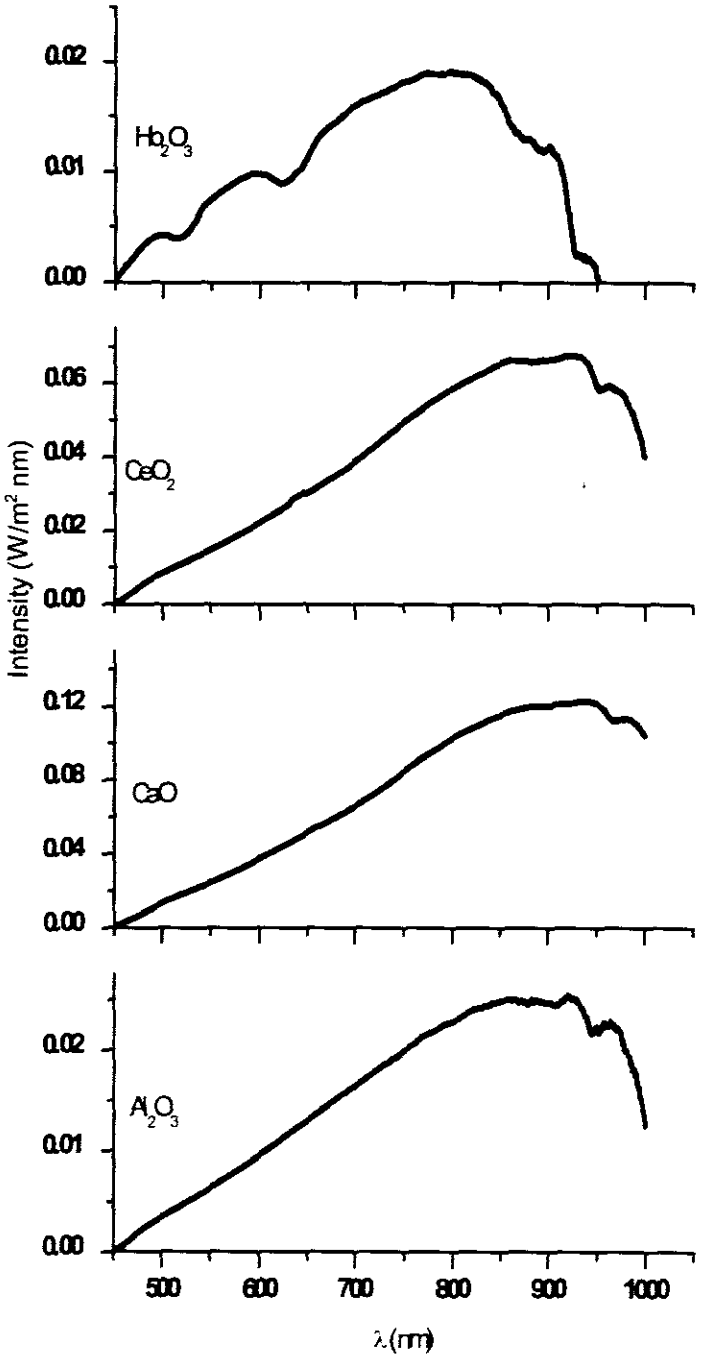

Figure 6.13: Emission spectra of metal-oxides compounds.

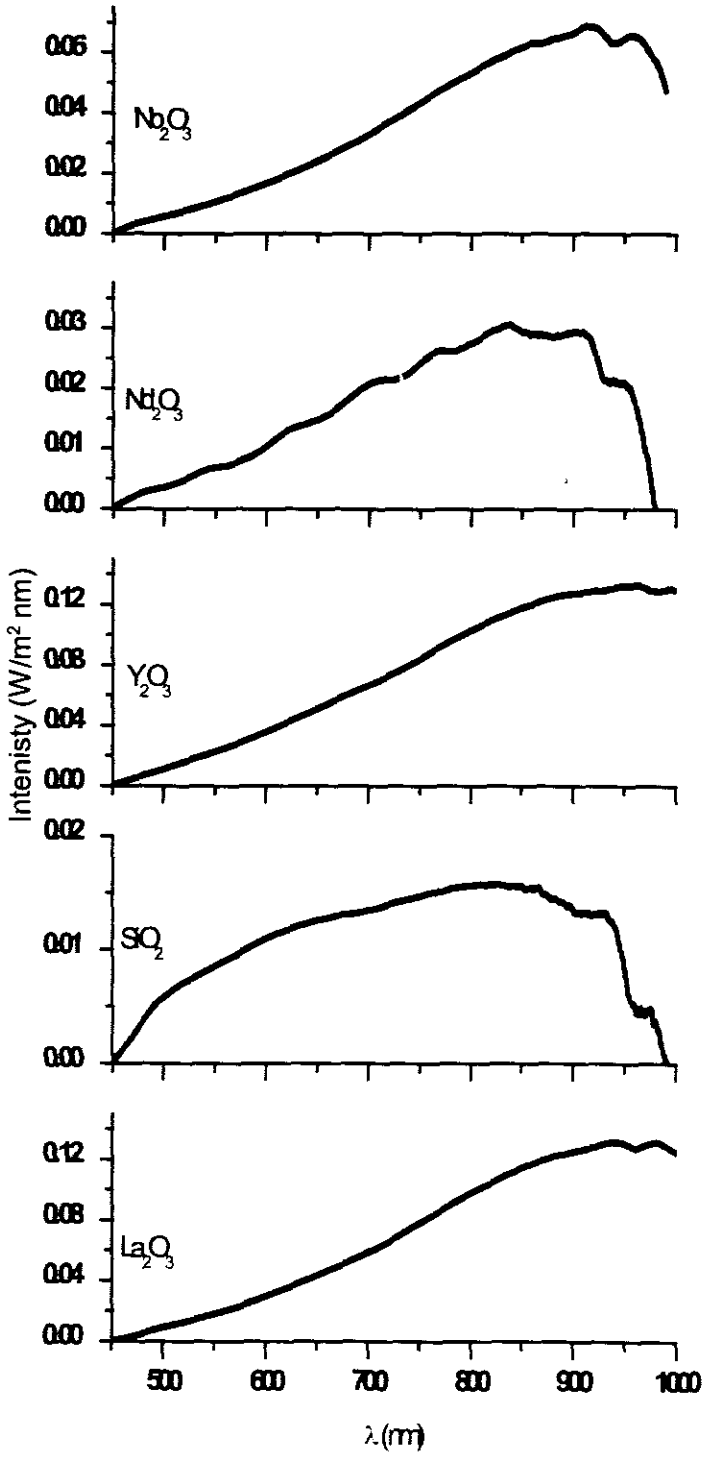

Figure 6.14: Emission spectra of metal-oxides compounds.

6.6 Temperature measurement of diamond

The stabilised temperature was measured at the various power configurations on the industrial diamond, from the minimum power to the maximum power of the laser beam. A polarisation-based attenuator was used to allow power variability by changing the angle of the attenuator. Emission spectra for the stabilised temperature are shown in figure 6.15. Then the graph of stabilised temperature versus power was plotted.

The graph in figure 6.16 shows the stabilised temperature versus power of the industrial diamond. The sample was heated in air. The model (as discussed in chapter 4) was fitted on the experimental data and there is good agreement between the experimental and theoretical results within the range of the spectrometer. There are no data points between 300 K and 1 400 K because of the limitations in the spectrometer range. The temperature range depends on the wavelength range of the spectrometer. The wavelength range of the spectrometer that was used in this study is in visible range (300 nm to 1000 nm). Therefore, at lower temperatures (such as 400 K) most of the emission is in the infrared. The accuracy of the temperature measurement is not known.

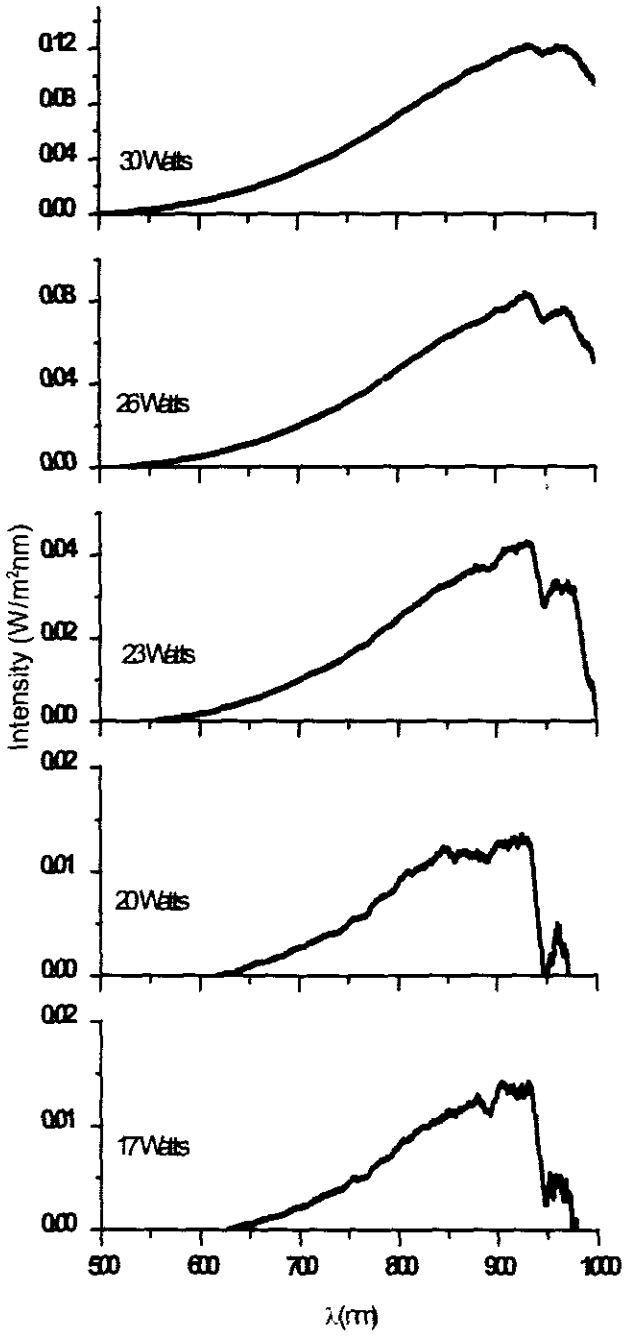

Figure 6.15: Emission spectra for the stabilised temperature (figure 6.16).

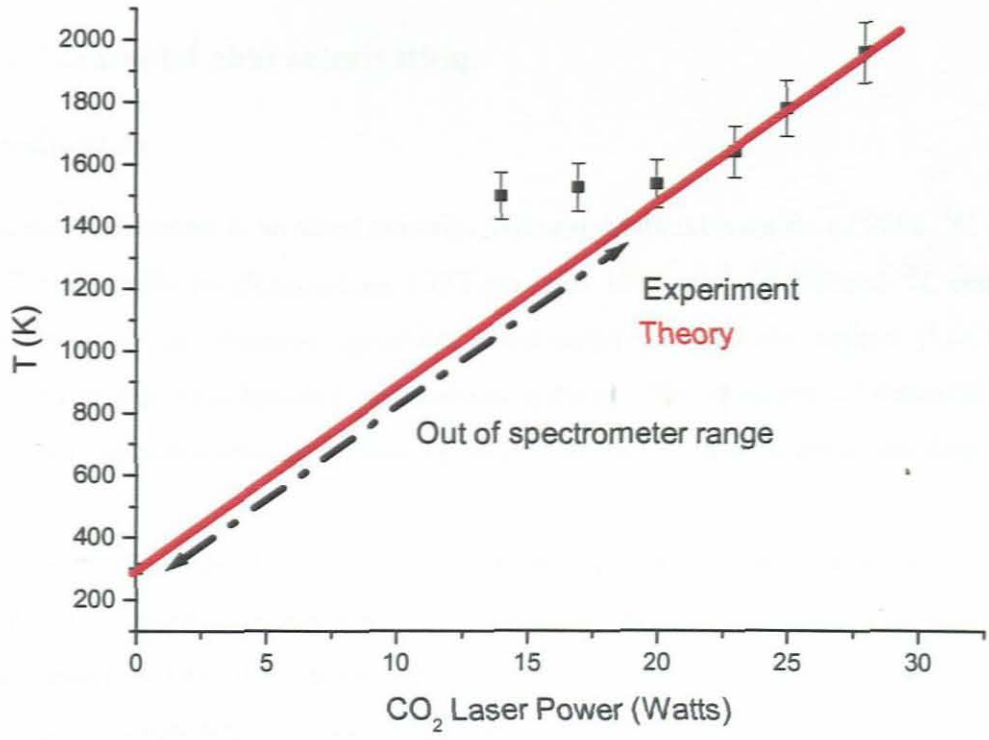

Figure 6.16: Stabilised temperature versus power on the industrial diamond, showing the experimental and theoretical data (equation 4.23 in chapter 4).

6.7 Conclusions

The set-up of the laser-based system for heating was achieved. The spectrometer was calibrated and used to capture the emission spectrum of various samples. Testing of metal-oxides showed good agreement between the experimental data and melting points in most of metal-oxides compounds such as CeO_2, CaO, lA_2O_3 and Y_2O_3. The temperature of the diamond was successfully measured and compared with models.

Chapter 7

Industrial diamond characterisation

7.1 Introduction

For applications diamond is an ideal material. Natural diamond consists of 98% ^{12}C and 1.1% ^{13}C. The Raman peaks for diamond are 1332 cm^{-1} and 1284 cm^{-1} for ^{12}C and ^{13}C respectively [48]. Carbon exists as diamond, graphite, tetrahedrally amorphous carbon (ta-C), carbon nanotubes, fullerenes (buckyballs) and carbon spheres. The structure of diamond leads to special mechanical and elastic properties by way of its very strong chemical bonding.

Diamond has the highest of all known natural materials in hardness, molar density, thermal conductivity and sound transmission. Because of its hardness diamond can be used as a cutting and grinding tool. Fine grain polycrystalline diamond films can be used as wire dies and water jet nozzles because polycrystalline artificial diamond nozzles are isotropic in hardness and lighter in weight, the latter of which is critical for most streamlined water cutting operations. Because of its high thermal conductivity diamond is presumed to be an ideal heat exchange material.

Diamond reacts with water and CO_2 at temperature above 870 K [48-49] and may also chemically react with metals to form carbides. In this chapter results of the analysis of the industrial diamond are presented. The techniques used for analysis are Raman spectroscopy, SEM, and XRD.

7.2 Experimental method

Two industrial diamonds synthesized by means of high pressure, high temperature (HPHT) methods have been employed in this study. The details of these two samples are discussed below. A CO_2 laser and a Nd:YAG laser operating at 10.6 μm and 1.064 μm respectively were used to heat the two industrial diamonds for 8 seconds. The details of these two lasers are summarised in Table 7.1.

Table 7.1: Details of laser parameters that were employed in this study.

Laser	Power (kW)	Diameter (μm)	Wavelength (μm)
CO_2	4	250	10.6
Nd:YAG	4	600	1.064

Initial sample

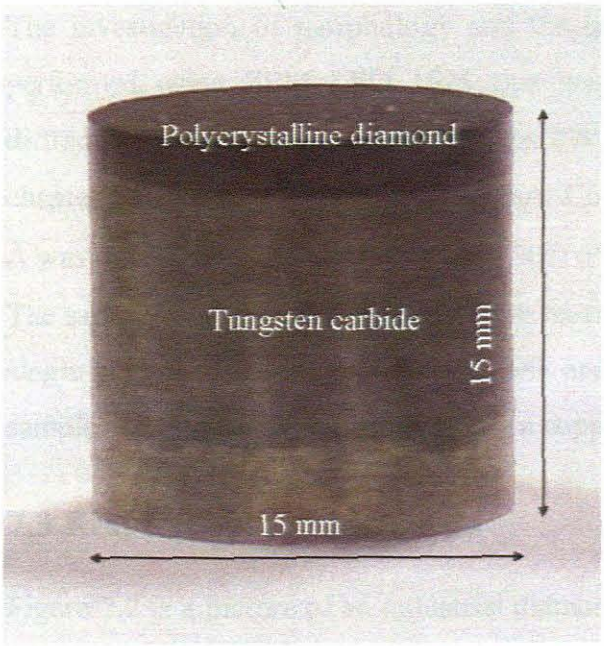

Figure 7.1: A photograph of industrial diamond that has been employed in this study.

Figure 7.1 is a picture of the initial sample of an industrial diamond that is made of a polycrystalline diamond (PCD) layer and a tungsten carbide substrate. The polycrystalline diamond layer possesses extremely high hardness and wear resistance, whereas the tungsten carbide substrate would greatly improve the toughness and weldability of the whole compact sample. PCD is used in geology for making drill bits, as well as in machine tooling. The diameter of the industrial diamond sample is 15 mm, its total height is 15 mm and the height of the PCD layer is 3 mm.

The analyses of the two samples were carried out using Raman spectroscopy, SEM and XRD. Raman scattering analyses were acquired with a Jobin-Yvon T64000 Raman spectrometer (the description of the Raman spectroscopy set-up is discussed in chapter 3) operated in single spectrograph mode. The 514.5 nm line of Coherent Innova 308 argon ion laser was used as

the source of light. The incident light was focused onto the sample via a Raman microscope attachment, using a 20x objective (~1.5 micron spot diameter). The power at the sample was <1.5 mW. Laser plasma lines were removed via a narrow bandpass filter, and the Rayleigh light was filtered via a holographic notch filter. The backscattered light was dispersed via a 1800 lines/mm grating onto a liquid nitrogen cooled CCD detector. Acquisition times were typically 2 minutes. Spectra were acquired and stored using Labspec 4.18 software.

The investigation of morphology and the qualitative analysis of industrial diamond were performed using SEM LEO 1525 that was discussed in chapter 3. The X-ray powder diffraction generator used was a Phillips PW 1830 generator (the description is discussed in chapter 3) operating at 45 kV and 40 mA. Copper $K_{\alpha 1}$ radiation with a wavelength of 1.5406 Å was used. The sample was run from $2\theta = 5°$ to 90°, step size 0.02° and step time 2 seconds. The sample was ground finer in an agate mortar and pestle prior to being sprinkle loaded on a single crystal of Si coated with Vaseline and analysed, e.g. C_ground (powder). The other samples were mounted on plasticene in a copper ring.

7.3 Results

Figure 7.2 is a picture of an industrial diamond after heating it with CO_2 laser for 8 seconds, and the initial sample for comparison. The physical changes for the sample heated with CO_2 laser compared with the initial sample are:

- There is a hole in the centre of the sample (labelled O).
- The sample is severed into two pieces with the crevice running along the centre of the hole (L_1, L_2).
- The substrate W+Co changed from black colour to dark/blue colour.
- There is yellowish-white powder denoted C at the interface between the polycrystalline diamond and substrate (only to the one piece B of the sample).
- There is a shining material and small crack on the surface of the sample (only to the one piece B of the sample).

Initial sample Sample heated with the CO_2 laser

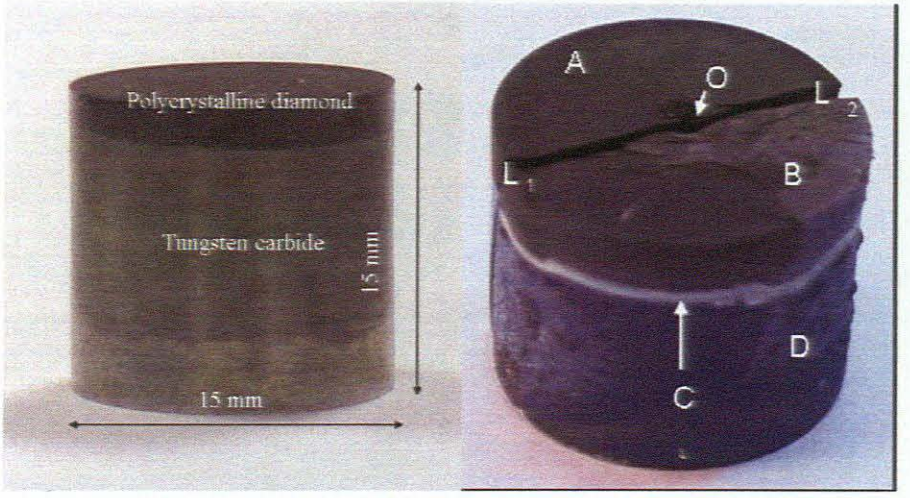

Figure 7.2: Comparisons of the initial sample and the sample heated with the CO_2 laser. Physical changes are pointed out in text.

Figure 7.3 is the comparisons of the two samples that are initial sample and the sample heated with the Nd:YAG laser. The physical changes are as follows:

- There are some small and big cracks on the surface of the sample.
- There are small and big spheres on the surface of the sample. The spheres are made of shining material.
- There is a hole at the centre of the sample.
- The sample is slightly larger than before; this could be due to the cracks

Initial sample

Sample heated with Nd:YAG laser

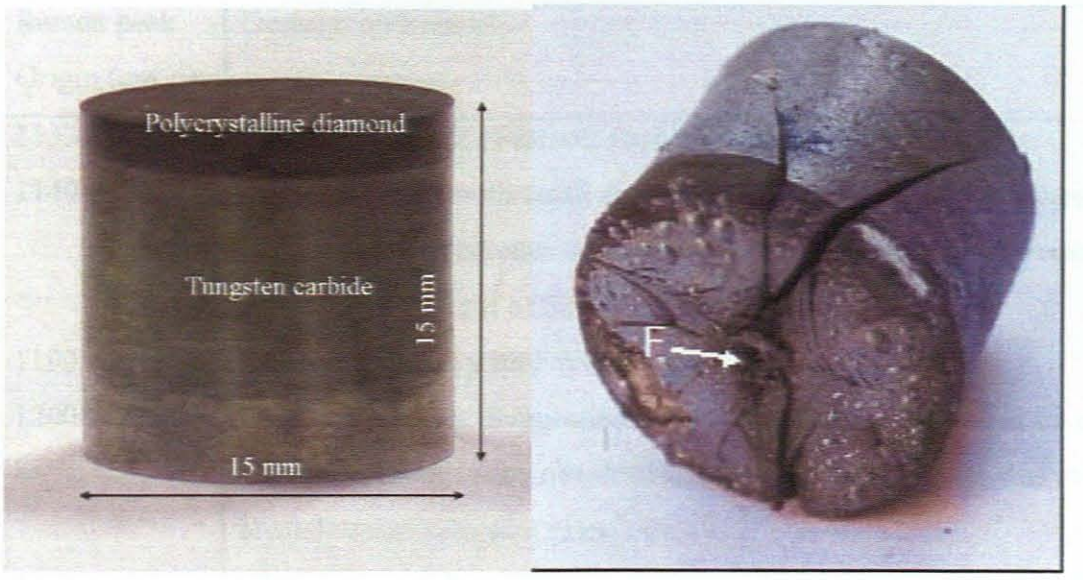

Figure 7.3: Comparisons of the two samples that are initial sample and heated with the Nd: YAG laser. Physical changes are pointed out in the text (above).

7.3.1 Raman spectroscopy

Raman scattering spectroscopy has been employed here to investigate the effects of laser irradiation on industrial diamond samples; literature reports of peaks within the Raman spectrum of diamond arising not only from the main diamond component but also from a number of carbon phases are summarized in table 6.2 [50].

Table 7.2: Summary of identified peaks in the Raman spectra of diamond and carbon films.

Raman peak Origin (cm^{-1})	Description/Remark
1133	Possible presence of carbon clusters containing double bonds
1140-1150	Present in films with small amounts of diamond crystalline domains suggesting the presence of nanocrystalline diamond or a precursor structure. A FWHM of 80 cm^{-1} has been quoted.
1190	Unassigned band with FWHM of 50 cm^{-1}.
1200-1230	Origins uncertain. Suggestions include amorphous diamond or may be boron related. Also observed in annealed carbon films due to the breakdown of selection rules.
1274	Observed in low pressure acetylene flame grown diamond with FWHM of 250 cm^{-1}.
1315-1320	Hexagonal diamond (Lonsdaleite).
1332	Diamond peak.
1340-1360	'D' peak associated with microcrystalline graphite (gain size <25 nm). Appears due to the breakdown of selection rules and broadens with disorder.
1271-1353	Observed in carbon films. Annealing was believed to increase the number or size of crystallites, in addition to reducing disorder, assigned to 'D' peak.
1357-1580	Diamond-like carbon material, Raman spectrum consists of several overlapping components within this band.
1580	'G' peak associated with single crystalline graphite that broadens with disorder within the graphite sheet.
1520-1600	Observed in carbon films. Annealing was believed to increase the number or size of crystallites, in addition to reducing disorder; assigned to 'G'.
1620	Disordered sp^2 carbon, present due to a breakdown of selection rules in fine crystalline material.

Figure 7.4 is a comparison of Raman spectra on the surface of the PCD before and after heating with a CO_2 laser. These spectra show two peaks: the first at 1120 cm^{-1} is an unknown peak and the second at 1332 cm^{-1} is the diamond peak. These spectra show that there was no chemical change on the surface of the PCD due to laser heating. The spectrum in figure 7.5 was taken on the white line along the circumference of the sample where the polycrystalline diamond and substrate are joined. From the spectrum we conclude that the white line along the circumference is tungsten trioxide (WO_3) (figure. 7.5).

Figure 7.6 is a comparison of Raman spectra on the surface of the PCD before and after heating with Nd:YAG laser. The increase of Raman peak has been observed after heating with Nd:YAG laser on the surface of the PCD. The spectrum (after heating) from the surface of the sample showed high intensity diamond peak at 1332 cm^{-1} and increased background, and no graphitic signature. Badzian *et al.* [51] also observed this Raman peak increase after they treated the polycrystalline diamond with laser and they alluded to the fact that this Raman peak indicated the increase of the parameter of atomic order (smaller atomic shifts from the perfect lattice nodes). Figure 7.7 is the comparison spectra of the two samples that were heated by Nd:YAG laser and CO_2 laser. The graphs show that both samples still have diamond present. However the sample heated with Nd:YAG laser, there is an increase in intensity.

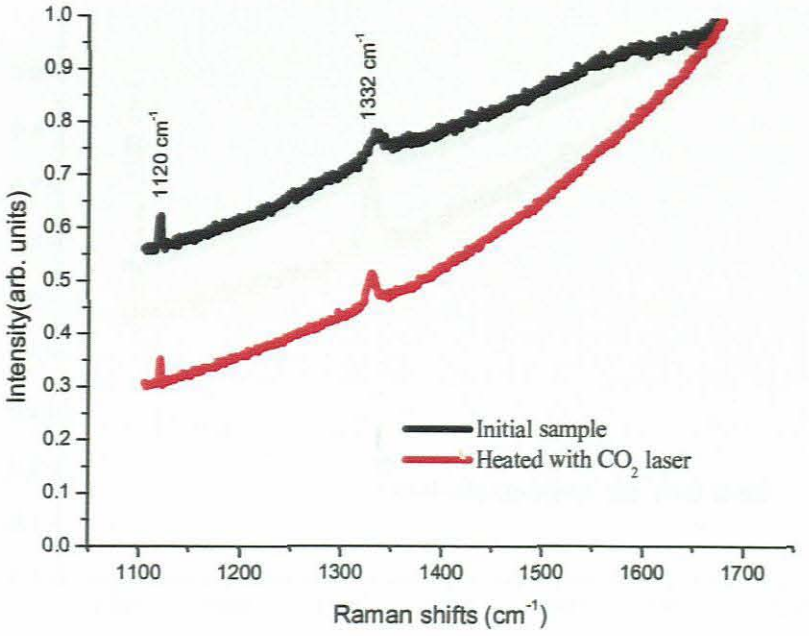

Figure 7.4: A comparison of Raman spectra taken on the surface of the polycrystalline diamond before and after heating with a CO_2 laser. These spectra show that the sample still has diamond present.

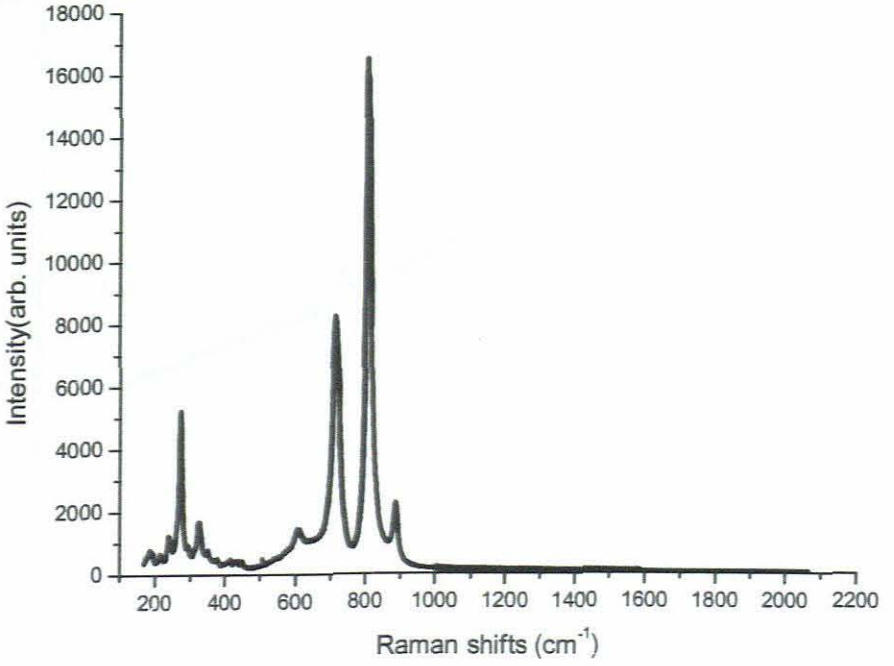

Figure 7.5: Raman spectrum on the yellowish-white powder at the interface between the polycrystalline diamond and substrate. This graph is showing that the substrate is changed to WO_3.

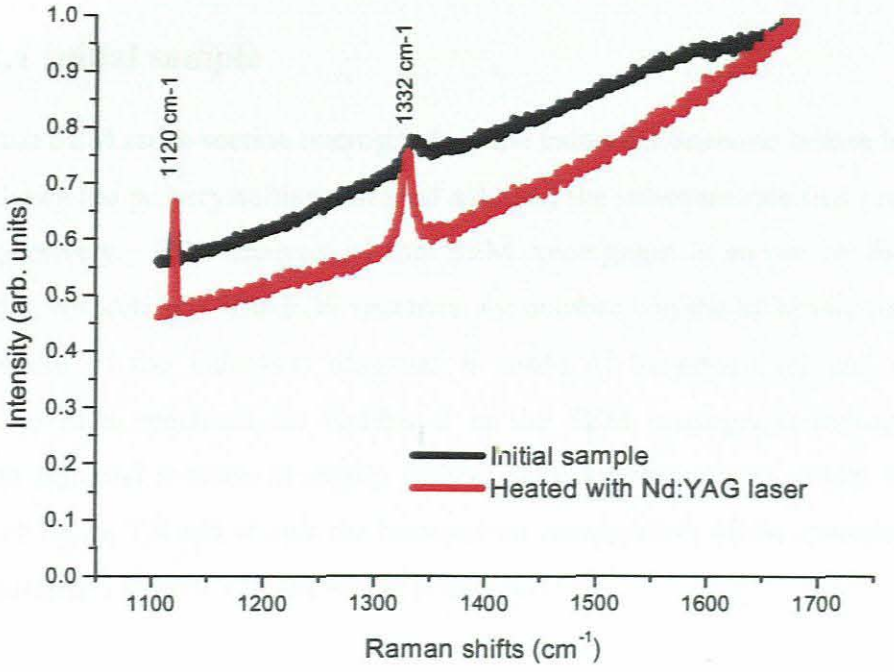

Figure 7.6: A comparison of Raman spectra taken on the surface of the polycrystalline diamond before and after heating with Nd:YAG laser.

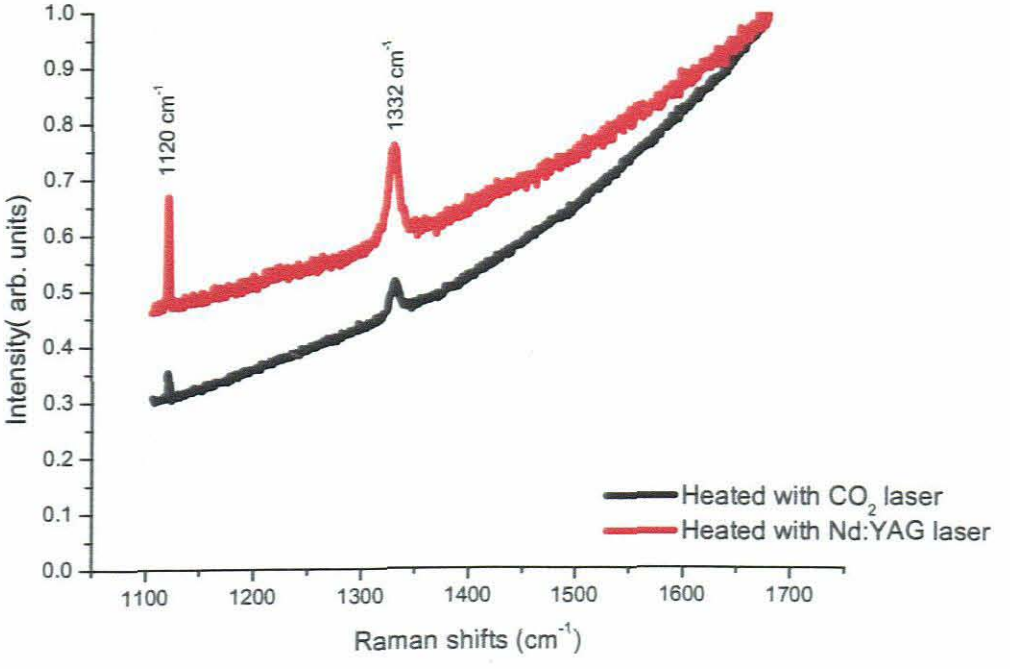

Figure 7.7: A comparison of Raman spectra taken on the surface of the polycrystalline diamond after heating with CO_2 and Nd:YAG laser.

6.3.2 SEM

6.3.2.1 Initial sample

Figure 7.8 is the SEM cross-section micrograph of the industrial diamond before heating. This micrograph shows the polycrystalline diamond side and the substrate side that are labelled as 1 and 2, respectively. EDS analysis of this SEM micrograph is shown in figure 7.8 for number 1 and 2, respectively. The EDS spectrum for number 1 in the SEM micrograph shows that the substrate of the industrial diamond is made of tungsten (W) and cobalt (Co) compound. The EDS spectrum for number 2 in the SEM micrograph indicates that the polycrystalline diamond is made of mostly carbon and trace amounts of cobalt. Figure 7.9 is the zoom-in of figure 7.8 and shows the honeycomb construction of the material. The EDS spectrum of number 3 (figure 7.9) shows the presence of Fe.

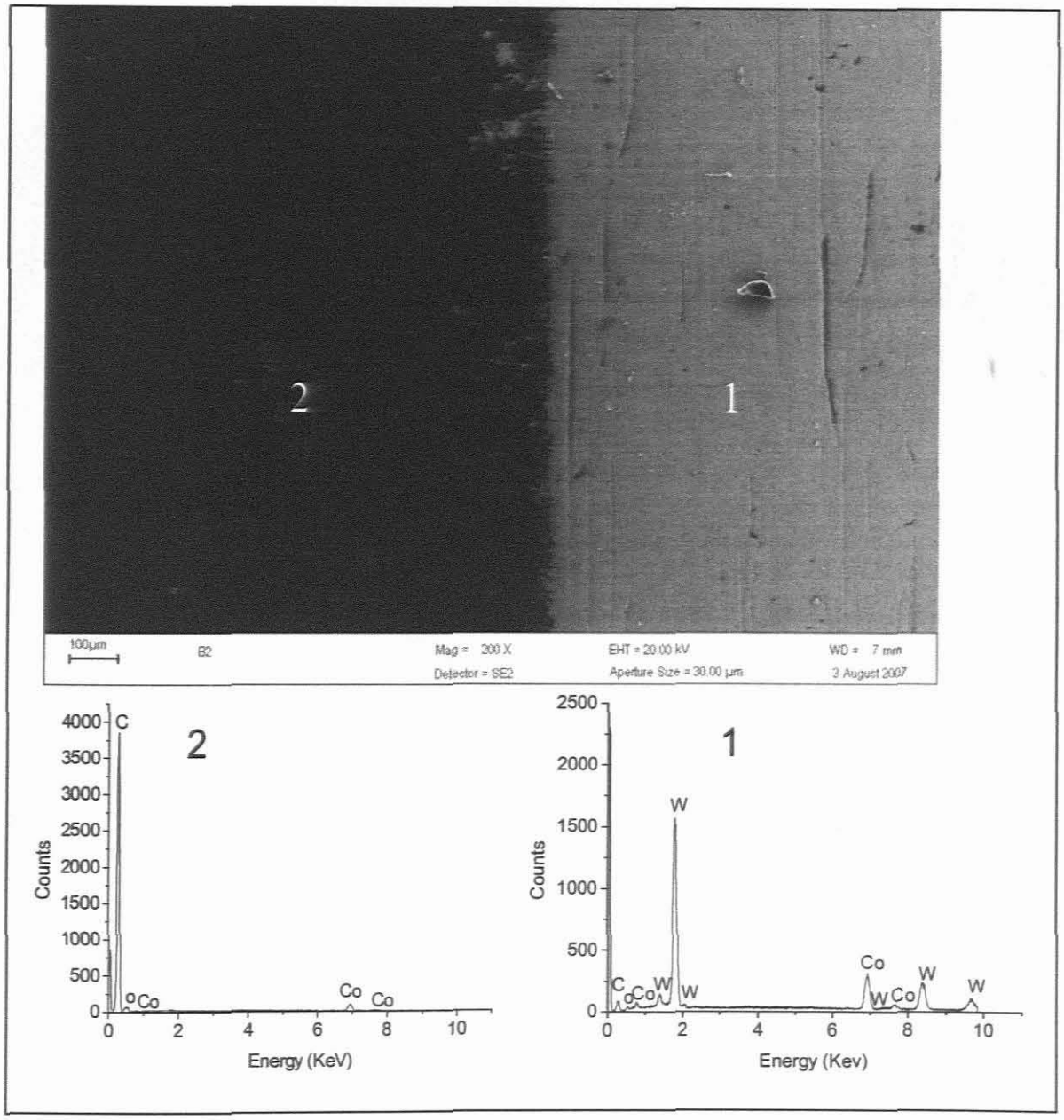

Figure 7.8: SEM cross-section micrograph of an industrial diamond before heating: 1 is the substrate side and 2 is the PCD side. The EDS spectrum for number 1 shows that the substrate is made of W and Co, initially. The EDS spectrum for number 2 shows that the PCD is mostly C.

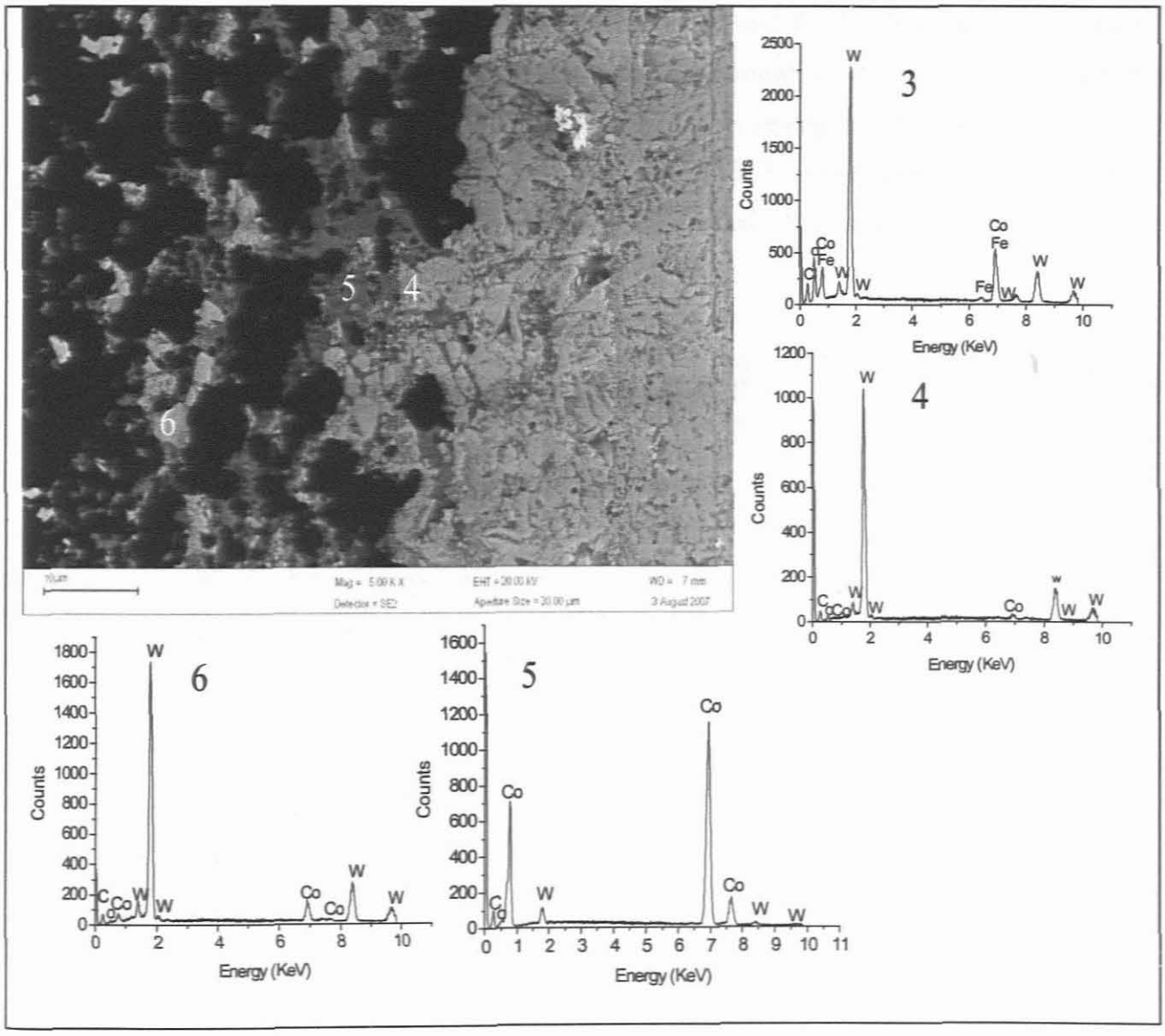

Figure 7.9: This is the zoom-in of figure 7.8 at the PCD/W+Co interface and shows the honeycomb construction of the materials before heating it. The EDS number 3 illustrates that the white material is the made of W, Fe, C and Co. EDS spectrum in number 4 is W, Co and C. Number 5 is along the interface between the PCD and substrate and shows that the most abundant element is Co.

7.3.2.2 Nd: YAG laser heated sample

Figure 7.10 is the SEM micrograph on the surface of an industrial diamond and the EDS spectra of industrial diamond on the surface of PCD after heating with Nd:YAG laser. This morphology is showing some spheres. The EDS spectrum illustrates that the sphere in number 7 is made of mostly C and trace amounts of Co and tungsten. The sphere label number 8 and 9

is made of Co and trace amounts of W and of course carbon as the EDS spectrum labelled 8 and 9. In summarise: the spheres are mostly made of Co and W. The EDS results illustrate that the tungsten carbide migrates from the substrate through to the diamond during the heating process. The laser beam of the Nd:YAG laser of wavelength 1.064 μm is transmitted through the diamond and heats up the W. Tungsten carbide phase separated into Co and W, and appeared on the surface. The morphology in labelled 10 is made of carbon, cobalt, tungsten and oxygen since the sample was heated in air.

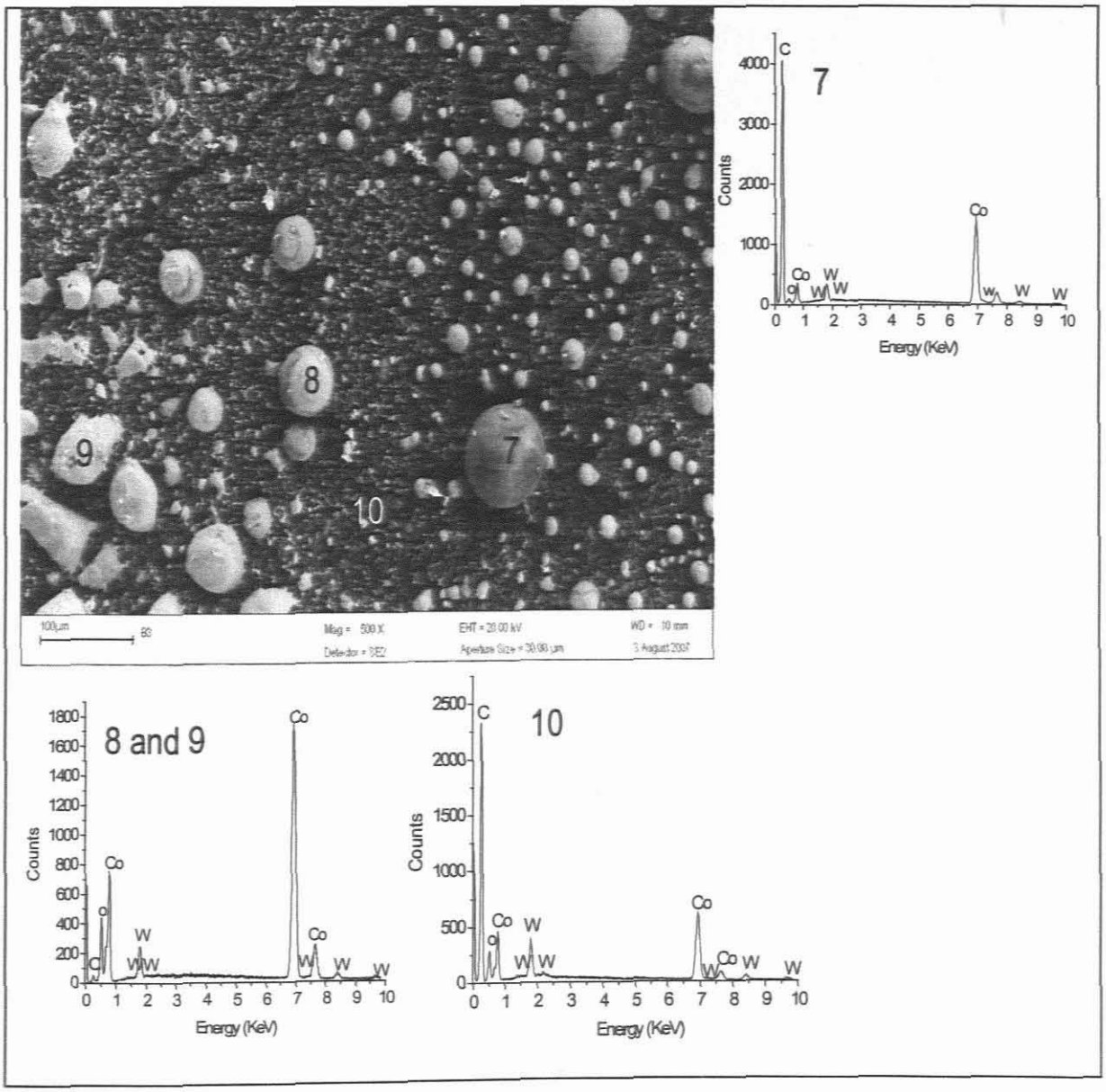

Figure 7.10: SEM micrograph and EDS spectra taken on the surface of the industrial diamond after heating by Nd:YAG laser for 8 seconds. The micrograph and EDS spectra show spheres that are made of Co and W.

7.3.2.3 CO_2 laser heated sample

Figure 7.11 is the SEM micrograph on the surface and the EDS spectrum on the surface of the sample which was heated with CO_2 laser for 8 seconds. The EDS spectrum is showing that the polycrystalline diamond layer is made of C, Fe and Co. The Co and W have migrated from the substrate through the polycrystalline diamond, while oxygen is present because the sample was heated in air. The SEM micrograph in figure 7.12 is the micrograph taken on the substrate and it shows that the bulk formation is tungsten.

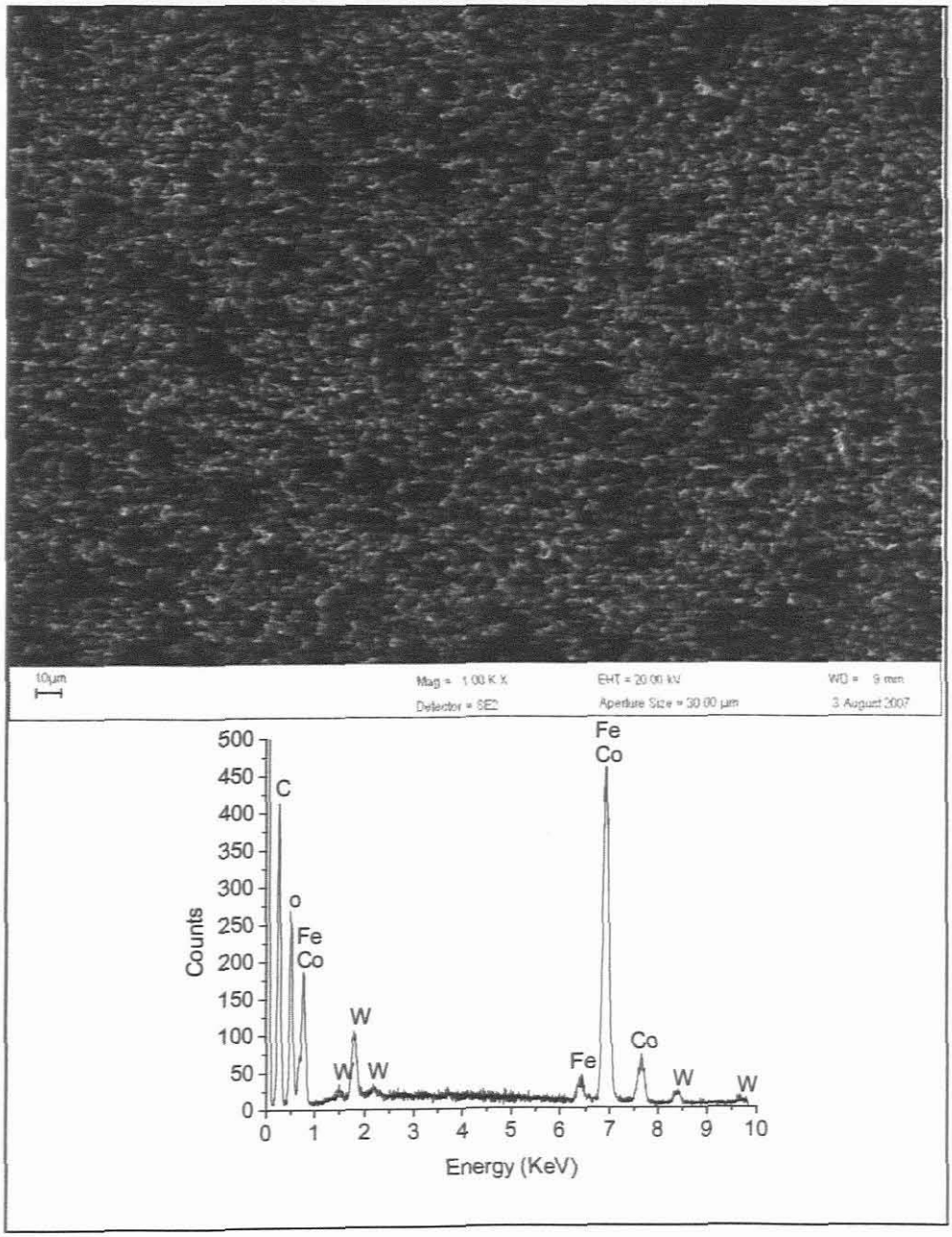

Figure 7.11: SEM micrograph on the surface of an industrial diamond and EDS spectrum of an industrial diamond after heating with CO_2 laser for 8 seconds on the PCD.

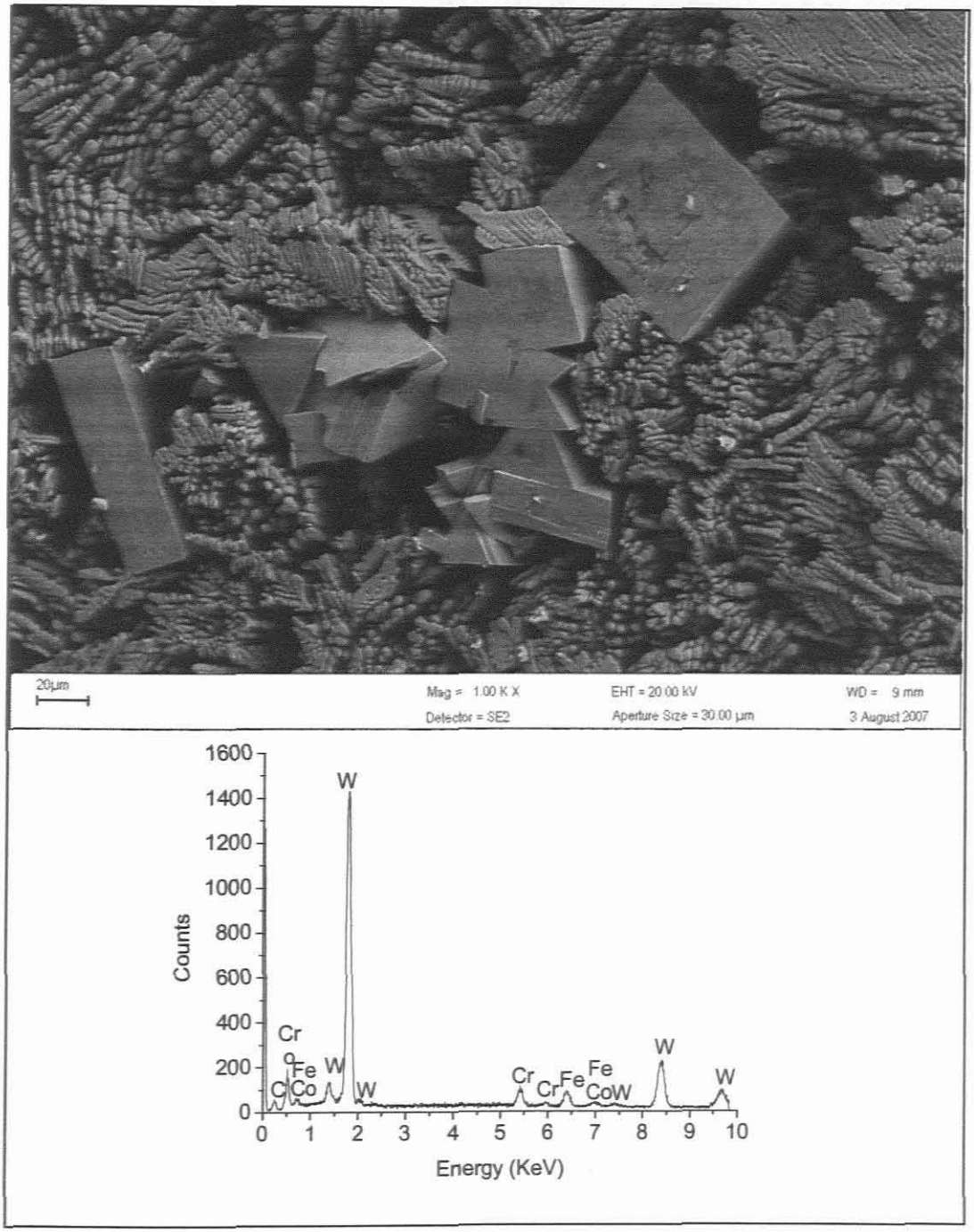

Figure 7.12: SEM cross-section micrograph and EDS spectrum of an industrial diamond after heating with CO_2 laser for 8 seconds. This micrograph was taken on the substrate.

7.3.3 X-ray diffraction

The samples were broken into four pieces and analysed by XRD as follows: C_OS was the outer surface of the polycrystalline diamond layer away from the W+Co, while C_IS was of the inner surface attached to the W+Co (refer to figure 7.13). Sample C_ground was the

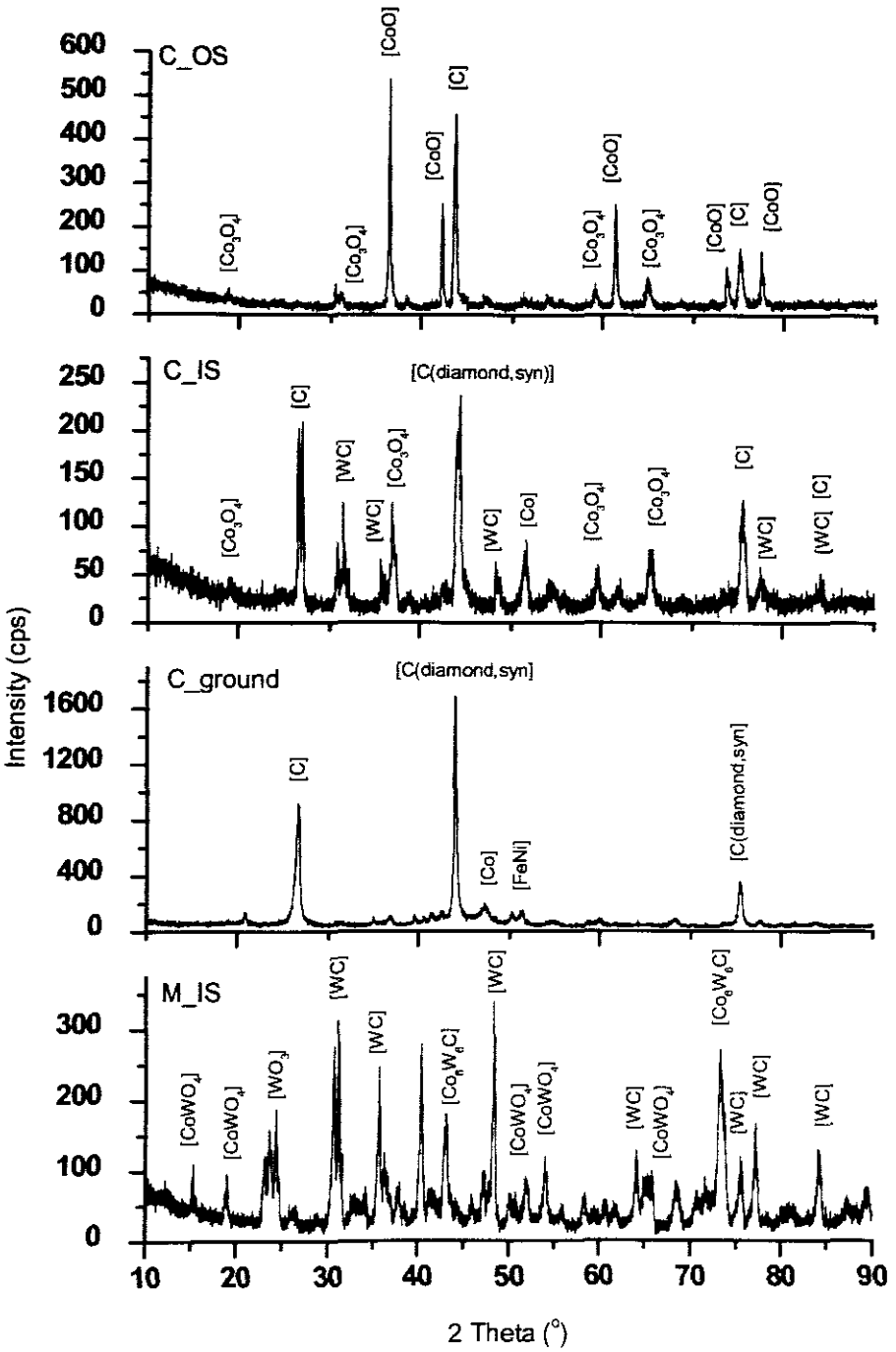

Figure 7.14: The XRD spectra of the industrial diamond after heating with Nd:YAG laser. The spectrum of M_IS shows that the substrate reacted and formed WC, WO_3 and $CoWO_4$.

7.3.3.2 CO_2 laser heated sample

The XRD spectra in figure 7.15 are spectra taken on the industrial diamond after heating with CO_2 laser. The spectrum on C_OS is showing the migration of Co to the diamond to form some oxides. The spectrum on C_IS indicates the migration of W+Co to the polycrystalline diamond surface. The spectrum on M_IS illustrates that the W reacted with C to form WC and Co migrated in the surface.

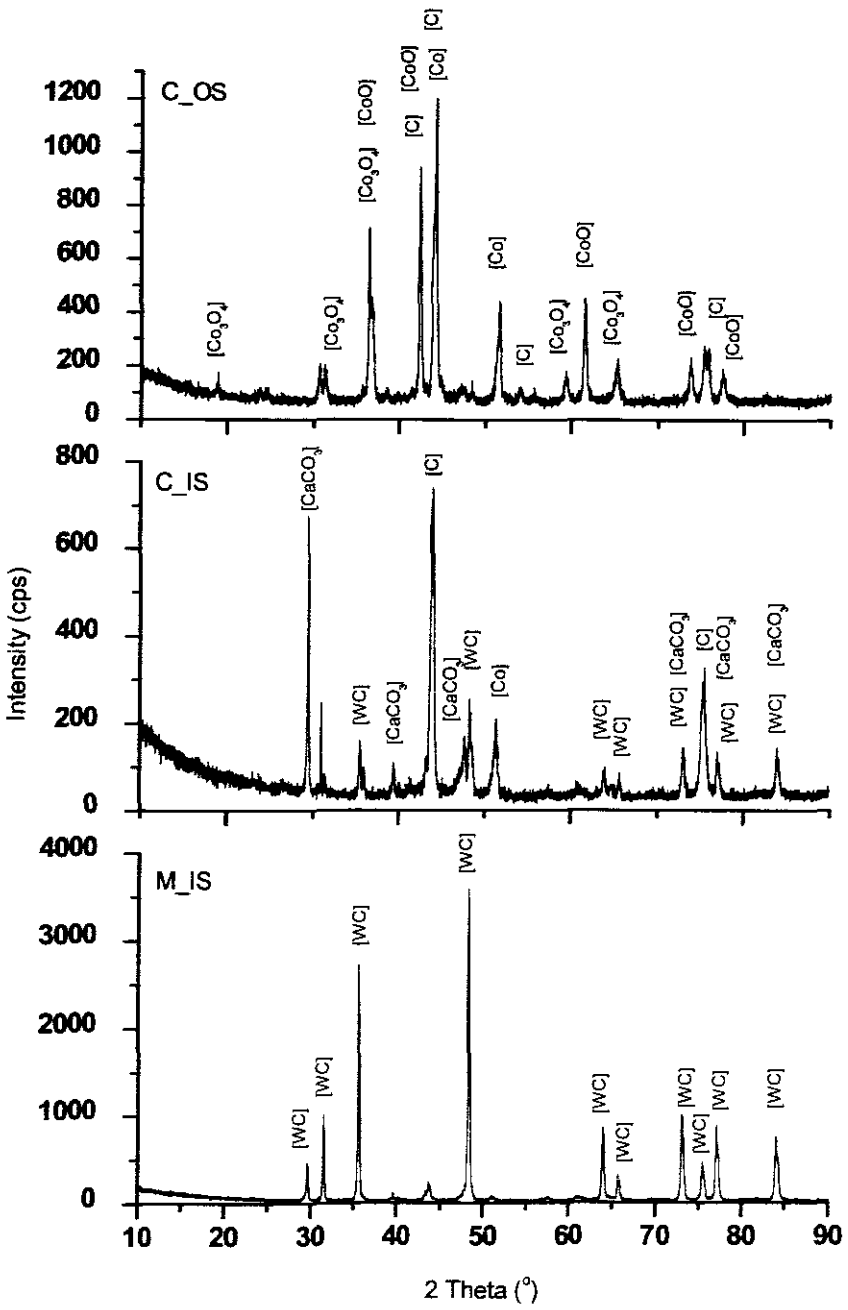

Figure 7.15: XRD spectra of the industrial diamond after heating with CO_2 laser. The spectrum of the C_OS shows the migration of Co into the C. The spectrum of the C_IS shows the W+Co. The $CaCO_3$ may originate from the calcite in the clay that was used to mount the sample. The spectrum of the M_IS shows that the substrate, W+Co changed from W+Co to WC.

7.4 Discussions

- Why do we see WO_x and CoO_x spheres in the Nd:YAG laser heated industrial diamond and not in the CO_2 laser heated industrial diamond one? We try to answer this question considering the following illustration.

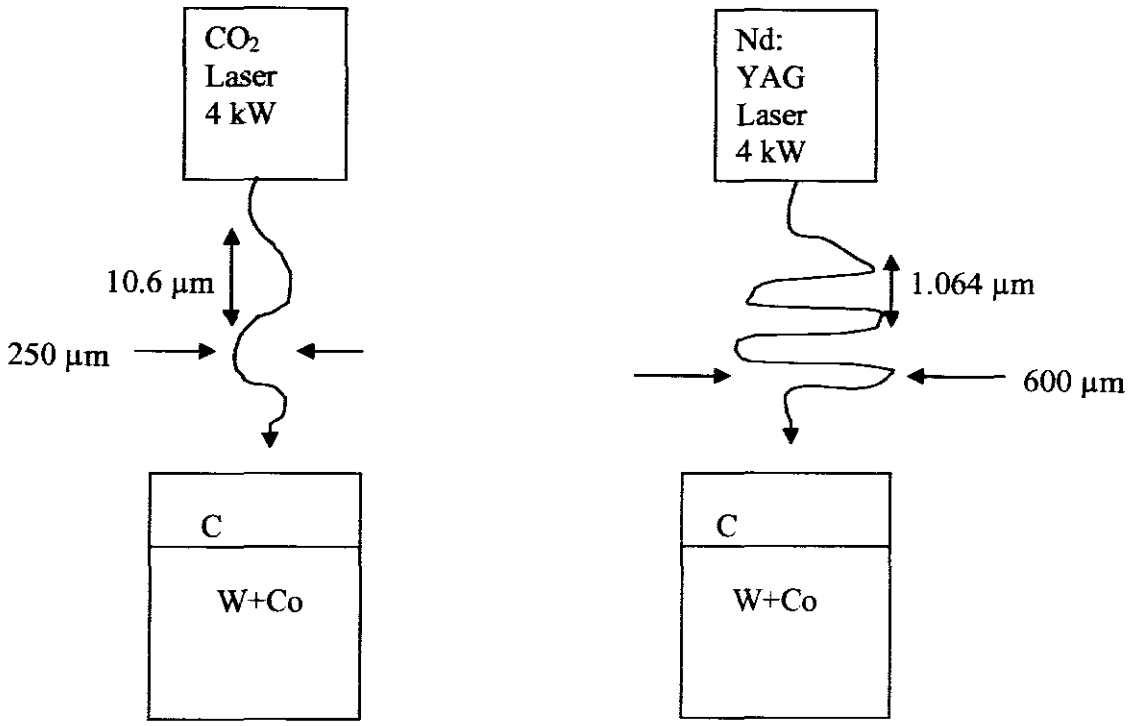

Figure 7.16: Schematic diagram of the two lasers in action.

The Nd: YAG laser has a shorter wavelength beam than the CO_2 laser and therefore is more penetrating. However the beam diameters of 250 μm and 600 μm respectively for the same power of 4 kW mean that the CO_2 laser has more intensity and hence the profound hole drilling capability than in the Nd:YAG laser. The fact that the diamond heated with Nd:YAG laser showed spherical particles of WO_x and CoO_x illustrates that the Co and W migrate from the substrate through the diamond and form oxides on the diamond surface, while at the same time C migrates at the diamond substrate and reacted with the W+Co matrix to form carbides of tungsten and cobalt as the EDS shows.

7.5 Conclusions

The industrial diamonds were successfully characterised using Raman spectroscopy, SEM and XRD.

7.5.1 Raman spectroscopy

The Raman spectra show that both the samples still have diamond. The increase of the Raman peak has been observed on the industrial diamond heated with Nd:YAG laser. The Tungsten trioxide formation has been observed as a yellowish-white powder at the interface between the polycrystalline diamond and substrate on the industrial diamond heated with CO_2 laser.

7.5.2 SEM

The SEM micrograph and EDX spectra which have been recorded here show that the PCD layer is made of mainly carbon, cobalt and iron. The substrate layer mainly is made of tungsten and cobalt. The structure of the sample resembles that of a honeycomb for both the PCD and the substrate layer.

The Nd:YAG laser heated sample: the SEM micrograph and the EDX spectra show that the tungsten and cobalt migrate from the substrate through to the surface of polycrystalline diamond layer to form oxides. The spheres on the surface of PCD were made of Co, W and trace amounts of C.

The CO_2 laser heated sample: the SEM micrograph and the EDX spectra shows some bulk formation on the substrate of the sample. This bulk formation is made of W and Co. There was nothing observed on the PCD surface except for the additional elements such as Fe.

7.5.3 XRD

The XRD spectra for both samples show that the substrate materials diffused in the surface of polycrystalline diamond. In conclusion the XRD spectra for the samples show some formation of oxides such as CoO_x.

Chapter 8

Concluding remarks and future work

8.1 Introduction

The main objective of this study was to heat an industrial diamond sample by means of optical absorption of a laser beam, and then measure the resulting temperature on the surface of the industrial diamond optically by means of emission spectrometer. The source of this study was a CO_2 laser and the characterisation of the CO_2 laser was done. The laser system was set-up and the temperature of the industrial diamond was raised and measured.

8.2 Concluding remarks

We have demonstrated an all optical system comprising of laser heating stage coupled to an optical spectrometer, for temperature measurements of various samples. In this study we have focussed on industrial diamond as the test sample. The CO_2 laser was successfully characterised and used as source of this study. In a test run of the non-contact temperature system of the industrial diamond was successfully obtained and compared with the mathematical model. There is qualitative agreement between the model prediction and experimental data. We have also shown numerical results on the predicted temperature profile on the surface of the sample, which has not yet been measured. We have also measured the melting temperature of the metal-oxide compounds as test for the system. There is good agreement between the experimental and expected data in these metal-oxide compounds CeO_2, CaO, La_2O_3 and Y_2O_3 while SiO_2, Nb_2O_5 and Ho_2O_3 do not show good agreement. Reasons for this are still being investigated and for now it is assumed that these metal-oxides are neither black nor grey bodies.

The surface of the industrial diamond was studied using SEM, XRD and Raman spectroscopy to quantify the damage after irradiation by higher power lasers. We characterised industrial diamonds that are: initial industrial diamond, heated industrial diamond with CO_2 laser and heated industrial diamond with Nd:YAG laser. The two heated samples were heated for 8 seconds with the same maximum power 4 kW for CO_2 laser and Nd:YAG laser. The temperatures were not measured.

The SEM analysis for both heated industrial diamonds (CO_2 laser and Nd:YAG laser heated respectively) show that cobalt and tungsten (in the substrate) diffused to the surface (polycrystalline diamond) and result in some interesting geometric structures, as shown in figure 7.12 (e.g., spheres and rhombics). Raman spectra show that both samples still contain diamond on the surface, with no graphite. This is understandable since the polycrystalline diamond is transparent to the laser radiation. The substrate heats up and parts of it become exposed. Most likely there is ablation at the polycrystalline diamond/tungsten carbide interface. The increase of the Raman peak at 1332 cm^{-1} has been observed after heating with a Nd:YAG laser. Badzian *et al.* [51] also observed an increase in this peak after they heated the polycrystalline diamond with a laser, and suggested that this indicates an increase in the parameter of atomic order.

The XRD spectra recorded on the inside and outside of the polycrystalline diamond confirm that indeed the tungsten cobalt diffused to the surface of to form some compounds such as CoO and Co_3O_4. These compounds have been observed on both samples.

8.3 Future work

Regardless of the technical excellence of the system, the temperature measure that it produces will only be as good as the calibration system. Future work is to calibrate the system because the accuracy of the temperature measurement is not known. There are two ways to perform the basic calibration for the temperature. One is to measure a source of well defined output and equate the signal from the emission spectrometer with the known output of the source at temperature to produce a series of calibration factors. The other method is to use a second well calibrated or standard instrument and compare the response of the two instruments to a single source. The source need not be well defined so long as both instruments measure it in exactly the same manner at the same time. A good calibration depends on more than just good lamp or source and instrument operation, attention must also be paid to the environment in which the calibration is performed.

Our test system is not able to measure low temperature because of the limitations in the spectrometer range. The temperature range that can be measured depends on the wavelength range of the spectrometer. The wavelength range of the spectrometer that was used in this study is in the visible range. Then for future work we wish to buy a spectrometer that is

working in the infrared range in order to measure low temperatures, because at lower temperatures most of the emission is in the infrared range.

In this study we have concentrated on the average temperature of the sample only. Then for future work we wish to measure the temperature profile across the sample experimentally, in order to compare it with numerical results on the predicted temperature profile on the surface of the sample. Lastly, we want to improve the model by including stress effect.

References

1. M. Fuchs, *Canopy thermal infrared observations,* Remote Sens. Rev., **5**, pp 323-333, 1990.
2. J. M. Baker , J. M. Noman, A. Kano, *A new approach to infrared thermometry,* Agricultural and forest meteorology, **108**, pp 281-292, 2001.
3. M. Jakob, *heat transfer*, Wiley, New York, **1**, 1949, pp 23.
4. R.P. Benedic, *Fundamentals of temperature, pressure, and flow measurements, 3rd edition*, pp 127.
5. T.J. Quinn, *Temperature monographs in physical measurements, series* editor: A.H. Cook, pp 284.
6. S. K. Thomas, *Blackbody theory and quantum discontinuity,* pp 1894-1912.
7. T.R. Harrison, *radiation pyrometry and its underlying principles of radiant heat transfer,* John Wiley an sons, Inc., publishers, pp 5.
8. J. Mehra, H. Rechneberg, T*he historical development of quantum theory*, **1** CHP 1, Springer, 1982.
9. R.C. Dougal, *The presentation of the Planck radiation formula, phys.* Educ., **11**, pp 438-443, 1976.
10. L.P. Daniel, *Multiwavelength pyrometry to correct for reflected radiation,* national aeronautics and space administration, 1990.
11. F.J. Blatt, *Modern physics,* New York: McGraw-Hill, 1992, 65
12. G.R. Fowles, *Introduction to modern optics,* Holt Rinehart and Winston, Inc., 1968,204.
13. Y. Tago, F. Akimoto, K. Kitagawa, N. Arai, *Measurements of surface temperature and emissivity by two dimensional four colour thermometry with narrow bandwidth,* energy, **30**, pp 485-495, 2005.
14. G. H. Wannier, *Statistical physics*, Dover, CHP 10-2, 1987.
15. R. Bowley, M. Sanchez, *Introductory statistical mechanics 2nd edition,* Oxford Clarendon Press.
16. H.J. kostkowski and R.D. Lee, *Theory and methods of optical pyrometry,* NBS Monograph **41**, 1962.
17. J.L. Gardner, T.P. Jones, and M.R. Davis, *Six wavelength radiation pyrometer,* High temperature-high pressure, **13**, pp 459-466,1981.
18. G.B. Hunter, C.D. Allemand, and T.W. Eagar, *Multiwavelength pyrometry: an improved method. Opt. Eng.*, **24**, 1985.

19. R. R. Corwin, A Rodenburgh II, *Temperature error in radiation thermometry caused by emissivity and reflectance measurement error,* applied optics, **33**, pp 1950-1957, 1994.
20. M. A. Khan, C. Allemand and T. W. Eagar, *Non-contact temperature measurement. II. Least squares based techniques,* Rev. Sci. Instrum., **62**, pp 403-409, 1991.
21. G. B. Hunter, C. D. Allemand, T. W. Eagar, *Prototype device for multi-wavelength pyrometry,* optical engineering, **25**, pp 1222-1231, 1986.
22. J. Ohno, *A method for temperature distribution measurement using multi-spectral radiance,* Pt.1 J. F. Schooley, ed., American institute of physics, **5**, pp 401-408, 1982.
23. B. Müller, U. Renz, *Time resolved temperature measurements in manufacturing,* measurement, **34**, pp 363-370, 2003.
24. S. Keyvan, R. Rossow, C. Romero, *Blackbody-based calibration for temperature calculations in the visible and near-IR spectral ranges using a spectrometer,* fuel, **85**, pp 796-802, 2006.
25. G. de Maupassant, *Film characterisation techniques, chapter 2,* the horla, 1887.
26. P.J. Goodhew, J. Humphreys, R. Beanland, *electron microscopy and analysis,* 3rd edition.
27. http://www.xraydiffrac.com/xraydiff.html.
28. pubs.usgs.gov/info/diffraction/html/index.html.
29. A. Sinha, A. B. Garg, V. Vijayakumar, B.K. Godwal, S.K. Sikka, *A CCD area detector for x-ray diffraction under high pressure for rotating anode source,* Bull. Mater. Sci., 23, 2000, 151.
30. B. Lengyel, Lasers, 2nd ed., 1971.
31. C. Patel, *High power carbon dioxide lasers,* Scientific American, 1968: An excellent introduction to the CO_2 laser.
32. C.K.N. Patel, *Continuous wave laser action on vibrational rotational transition of CO_2,* Physics Review, 1964, **136A**, 1187.
33. C.S. Willet, *Introduction to gas lasers population inversion mechanisms,* international series of monographs in natural philosophy, general editor: D. Ter Haar, vol. 67.
34. Weber, J. Marvin, *Handbook of laser science and technology,* Boca Raton: CRC Pres. Inc., 1982, vol 11- Gas laser.
35. W.E. Scheneider, R. Young, *A guide to photometry and visible Spectroradiometry,* optronic laboratories, inc., 1998.
36. J.H. Walker, R.D. Saunders, A.T. Hattenburg, *Spectral radiance calibrations,* NBS special publication, **250**, 1987.

37. *A guide to Spectroradiometry, instruments and applications for the ultraviolet,* Bentham instruments LTD, Issue 2, 1997.
38. http://teaching.shu.ac.uk/hwb/chemistry/tutorials/molspec/uvvisab3.htm.
39. G.B. Arfken, H.J. Weber, *Mathematical methods for physicist 4th edition,* p 385.
40. A.D. Polyanin, *Handbook of linear partial differential equations for engineers and scientists,* Chapman and hall/CRC.
41. H.D. Young, *University physics 8th edition,* Addison welsley 5290.
42. P. Majumdar, H. Xia, *A green's function model for the analysis of laser heating of materials*, applied mathematical modelling, **31**, 2007, 1186.
43. P.B. Chapple, *Beam waist and M_2 measurement using a finite slit,* optical engineering, **33**, 1994, 2461.
44. www.mellesgriot.com
45. http://en.wikipedia.org/wiki/Brewster's_angle
46. G.R. Fowles, *Introduction to modern optics,* Holt, Rinehart and Winston, INC., chapter 2.
47. http://www.processmaterials.com/oxides.html
48. S. Tong Lee, Z. Lin, X. Jiang, *CVD diamond films: nucleation and growth,* materials science and engineering, **25**, 1999, 123.
49. J.E. Field, *The properties of diamond,* academic press, oxford, 1979.
50. S.S.M. Chan, M. D. Whitfield, R.B. Jackman, G. Arthur, F. Goodall and R. A. Lawes, *The effect of excimer laser etching on thin film diamond*, Semicond. Sci. Technol. **18**, 2003, S46-S48.
51. A. Badzian, R. Roy, T. Badzian, W. Drawl, P. Mistry, M.C. Turchan, K. Cherian, *Decrystallization of diamond by Nd: YAG and excimer lasers and subsequent lattice relaxation,* diamond and related materials, **14**, 2005, 1562.